



**HAL**  
open science

# Study of an Optical Enhancement Cavity for Thomson Scattering Light Sources

Huan Wang

► **To cite this version:**

Huan Wang. Study of an Optical Enhancement Cavity for Thomson Scattering Light Sources. Optics [physics.optics]. Université Paris-Saclay; Qing hua da xue (Pékin), 2020. English. NNT : 2020UP-ASP092 . tel-03179872

**HAL Id: tel-03179872**

**<https://theses.hal.science/tel-03179872>**

Submitted on 24 Mar 2021

**HAL** is a multi-disciplinary open access archive for the deposit and dissemination of scientific research documents, whether they are published or not. The documents may come from teaching and research institutions in France or abroad, or from public or private research centers.

L'archive ouverte pluridisciplinaire **HAL**, est destinée au dépôt et à la diffusion de documents scientifiques de niveau recherche, publiés ou non, émanant des établissements d'enseignement et de recherche français ou étrangers, des laboratoires publics ou privés.



# Study of Optical Enhancement Cavity for Thomson Scattering Light Sources

**Thèse de doctorat de l'Université Paris-Saclay et  
de l'Université Tsinghua**

École doctorale n° 576 particules, hadrons, énergie, noyau,  
instrumentation, image, cosmos et simulation (PHENIICS)  
Spécialité de doctorat: Physique des accélérateurs  
Unité de recherche: Université Paris-Saclay, CNRS, IJCLab, 91405,  
Orsay, France  
Réfèrent: Faculté des sciences d'Orsay

**Thèse présentée et soutenue à Pékin, le 7 Décembre 2020, par**

**Huan WANG**

## Composition du jury:

<b>Kexin LIU</b> Professeur, Université de Pékin	Président & Rapporteur
<b>Chuanxiang TANG</b> Professeur, Université Tsinghua	Rapporteur & Examineur
<b>Huaibi CHEN</b> Professeur, Université Tsinghua	Examineur
<b>Renkai LI</b> Professeur, Université Tsinghua	Examineur
<b>Guoxi PEI</b> Professeur, Institut de Physique des Hautes Energies, Académie Chinoise des Sciences	Examineur
<b>David ROS</b> Professeur, Université Paris-Saclay	Examineur
<b>Fabian ZOMER</b> Professeur, Université Paris-Saclay	Directeur de thèse
<b>Wenhui HUANG</b> Professeur, Université Tsinghua	Codirecteur de thèse

# 用于汤姆逊散射的光学增益腔的研究

(申请清华大学和巴黎萨克雷大学  
工学博士学位论文)

培养单位： 工程物理系

学    科： 核科学与技术

研  究  生： 王    焕

指导教师： 黄  文  会    教  授

联合导师： **Fabian Zomer** 教  授

二〇二〇年十二月



# **Study of Optical Enhancement Cavity for Thomson Scattering Light Sources**

Dissertation Submitted to  
**Tsinghua University & Paris-Saclay University**

in partial fulfillment of the requirement

for the degree of

**Doctor of Philosophy**

in

**Nuclear Science and Technology**

by

**Huan Wang**

Dissertation Supervisor: Professor Wenhui Huang

Cooperate Supervisor: Professor Fabian Zomer

**December, 2020**



# 学位论文指导小组、公开评阅人和答辩委员会名单

## 指导小组名单

黄文会	教授	清华大学
Fabian Zomer	教授	巴黎萨克雷大学

## 公开评阅人名单

唐传祥	教授	清华大学
刘克新	教授	北京大学

## 答辩委员会名单

主席	刘克新	教授	北京大学
委员	唐传祥	教授	清华大学
	陈怀璧	教授	清华大学
	李任恺	教授	清华大学
	裴国玺	教授	中国科学院 高能物理研究所
秘书	黄文会	教授	清华大学
	潘志龙	助理研究员	清华大学



## 关于学位论文使用授权的说明

本人完全了解清华大学有关保留、使用学位论文的规定，即：  
清华大学拥有在著作权法规定范围内学位论文的使用权，其中包括：（1）已获学位的研究生必须按学校规定提交学位论文，学校可以采用影印、缩印或其他复制手段保存研究生上交的学位论文；（2）为教学和科研目的，学校可以将公开的学位论文作为资料在图书馆、资料室等场所供校内师生阅读，或在校园网上供校内师生浏览部分内容；（3）根据《中华人民共和国学位条例暂行实施办法》及上级教育主管部门具体要求，向国家图书馆报送相应的学位论文。

本人保证遵守上述规定。

（保密的论文在解密后遵守此规定）

作者签名： 王烁  
日 期： 2020年12月14日

导师签名： 黄文会  
日 期： 2020年12月14日



## 摘要

高平均功率光学增益腔在多个领域有着广泛的应用，包括用于汤姆逊散射产生高平均通量的 X 或伽马射线、光腔增强的高次谐波产生、引力波探测、稳态微聚束光源以及聚变能源实验等。

本论文的工作聚焦于以汤姆逊散射应用为背景的高平均功率光腔的理论与实验研究。以提高汤姆逊散射所产生光子的平均通量为目标，其要求光腔内激光场具有尺寸约为几十微米的束腰、脉冲长度为皮秒量级，并且具有稳定的几百千瓦的平均功率。

为了在汤姆逊散射模拟中更精确并且更高效的描述光腔内强聚焦的激光场，通过使用一种推广型的 Lax 级数展开的方法给出了强聚焦、线偏振激光场的一组非傍轴近似的表达式。

为了抑制在光腔内激光平均功率达到约 100 kW 时开始明显出现的影响光腔稳定性并且可能导致光腔失锁的模式不稳定性，使用将腔镜热弹性形变与腔内平均功率线性关联的 Winkler 模型较好的描述了引起光腔模式不稳定性的模式简并。我们提出并模拟证明了 D 型镜法可以成功抑制光腔内的模式不稳定性。在汤姆逊散射光源装置 ThomX 的原型光腔上安装 D 型镜并实现了小时时间尺度的 200 kW 稳定的平均储存功率。

针对影响光腔稳定性并阻碍腔内激光功率达到设计指标的光腔内功率快速下降现象进行了分析。这一现象表现为光腔内功率下降的幅度和时间尺度依赖于腔内的功率水平，进一步提升注入激光的功率最终导致光腔注入耦合镜表面的不可修复的损伤。通过对实验后已损伤的腔镜表面的成像和实验过程中采集的光腔的透射及反射数据的分析，发现主导这一现象的物理因素是腔镜表面的污染形成的热斑产生的表面形变所引起的散射损耗而导致的，并且通过模拟对这一现象进行了重现。这一分析可以帮助理解在多领域应用的高功率光腔上出现的此类功率快速下降现象背后的物理过程并起到损伤预警的作用。

给出了清华汤姆逊散射光源装置 TTX 的原型光腔的完整设计并进行了初步实验，实现了将连续型激光器与光腔锁定的实验目标。对中心波长为 1064 nm 的连续型注入激光实现了 133 倍的增益。并且给出了 TTX 原型光腔高功率实验的设计以及将与电子储存环结合的 TTX 光腔的设计。

**关键词：**光学增益腔；汤姆逊散射；高功率；热效应

## Abstract

High-average-power optical enhancement cavities (OEC), have a wide range of applications including Thomson scattering producing high average flux quasi-monochromatic X/ $\gamma$ -rays, cavity-enhanced high-order harmonic generation (HHG), gravitational wave interferometers, steady-state microbunching (SSMB) light sources and fusion energy experiments etc.

The works of this thesis focus on the theoretical and experimental studies of high-average-power OEC dedicated to Thomson scattering light sources. With the purpose of increasing the average flux of Thomson scattering generated photons, it is demanded for the laser beam inside OEC to have small waist with radius size of few tens of microns, pulse length at the order of picosecond and stable intra-cavity average power of few hundreds of kilowatts.

To precisely and effectively describe the highly focused laser field inside OEC to be used in simulations of Thomson scattering, a field expression of nonparaxial corrected highly focused linearly polarized laser field is derived with a generalized Lax series expansion method.

To suppress the modal instabilities start to appear apparently on OEC with an intra-cavity average power reaching  $\sim 100$  kW which affect cavity stability and could lead to lose of lock, the modal instabilities are well described with mode degeneracies induced by mirror surface thermoelastic deformation characterized by Winkler model. We brought up the D-shape mirror method for suppressing modal instabilities and proved its effectiveness with simulation. An hour-time-scale stable intra-cavity average power of 200 kW was realized on the prototype OEC of Thomson scattering light source ThomX with implementation of D-shape mirrors inside.

Analysis is carried out for understanding the fast power drop phenomenon appearing on OEC which affects the cavity stability and hinders the intra-cavity power reaching the designed goal. Intra-cavity power drops appeared with magnitude and time scale depending on the power level. Increasing further the incident power led to irreversible damage of the cavity coupling mirror surface. The origin of this phenomenon is investigated with *post mortem* mirror surface imaging and analysis of the signals transmitted and reflected by the OEC. Scattering loss induced by mirror surface deformation due to a hot-spot con-

taminant is found to be most likely the dominant physics behind this phenomenon and the cavity behavior could be well reproduced by simulation. This analysis could help to understand the physical process behind this kind of power drop phenomenon appearing on OEC being applied in wide range of applications and to prevent permanent mirror damage.

Full design of the prototype OEC of Tsinghua Thomson scattering X-ray light source (TTX) is presented and preliminary experiment is carried out on it, realizing the goal of locking a continuous wave injection laser with the cavity with the cavity gain measured to be 133. Design of the high power experimental setup for TTX prototype OEC and the design for TTX OEC to be coupled with the electron storage ring are provided.

**Keywords:** Optical enhancement cavity; Thomson scattering; high power; thermal effect

## Contents

摘 要.....	I
Abstract.....	II
Contents.....	IV
Chapter 1 Introduction .....	1
1.1 Background and Motivation .....	1
1.2 Thomson Scattering Light Source .....	1
1.2.1 Principles of Thomson Scattering.....	1
1.2.2 Thomson Scattering Light Sources Based on Optical Enhancement Cavity	5
1.2.3 ThomX .....	10
1.2.4 TTX.....	10
1.3 Development Status of Optical Enhancement Cavity .....	12
1.3.1 Development of Optical Enhancement Cavity in Different Fields .....	13
1.3.2 Development of Optical Enhancement Cavity with Specialized Features .	18
1.3.3 Development of Optical Enhancement Cavity in China .....	21
1.4 Focus of Dissertation .....	22
1.4.1 Main Work .....	22
1.4.2 Innovation Points .....	24
Chapter 2 Basic Principles of Optical Enhancement Cavity .....	25
2.1 Properties of Fabry-Perot Cavity.....	25
2.1.1 Stability Condition.....	25
2.1.2 Cavity Mode.....	26
2.1.3 Cavity Frequency Comb .....	27
2.2 Enhancement of Fabry-Perot Cavity.....	29
2.2.1 Cavity Enhancement with Continuous Wave Injection .....	29
2.2.2 Cavity Enhancement with Pulsed Wave Injection.....	31
2.3 Coupling of Injection Laser into Fabry-Perot Cavity.....	32
2.3.1 Transverse Mode Matching with Telescope .....	32
2.3.2 Longitudinal Phase Locking with PDH Technique.....	34

Chapter 3	Nonparaxial Expression of Highly Focused Laser Field .....	37
3.1	Series Expansion Formalism.....	38
3.2	Ignatovsky Formalism.....	41
3.3	Approximating the Ignatovsky Formulae with the Series Expansion .....	42
Chapter 4	Suppression of Modal Instabilities .....	50
4.1	Prototype Cavity SBOX of ThomX.....	50
4.2	Observation of Modal Instabilities.....	56
4.3	Modeling of Modal Instabilities.....	57
4.3.1	Mirror Thermoelastic Deformation Characterized by Winkler Model.....	57
4.3.2	Modal Instabilities Induced by Mode Degeneracy .....	60
4.4	Implementation of D-shape Mirrors for Suppressing Modal Instabilities .....	61
4.4.1	Simulation of Cavity Mode with Implementation of D-shape Mirrors .....	62
4.4.2	High Power Experiments with Suppression Modal Instabilities.....	65
Chapter 5	Study of Prior-damage Dynamics.....	69
5.1	Observation of Prior-damage Phenomenon.....	69
5.2	Modeling of Prior-damage Dynamics .....	73
5.2.1	Mirror Temperature Increase Characterized by Hello-Vinet Model.....	75
5.2.2	Prior-damage Dynamics Induced by Hot Spot.....	79
5.3	Simulation Results of Prior-damage Dynamics .....	82
Chapter 6	Study on Optical Enhancement Cavity of TTX .....	92
6.1	Preliminary Experiments on TBOX .....	93
6.1.1	Preliminary Experimental Setup of TBOX .....	93
6.1.2	Locking a Continuous Wave Injection Laser with TBOX.....	96
6.1.3	Key Parameters Measurement of TBOX .....	105
6.2	Design of High Power Experiments on TBOX.....	109
6.3	Design of Optical Enhancement Cavity for TTX.....	112
Chapter 7	Concluding Remarks.....	117
Bibliography	.....	119
Acknowledgements	.....	126
Statement	.....	127
Resume and Academic Achievements	.....	128

Contents

---

领导小组学术评语.....	129
答辩委员会决议书.....	130

## Chapter 1 Introduction

### 1.1 Background and Motivation

Since the first operation of laser demonstrated by Theodore Maiman in 1960<sup>[1]</sup>, human continues striving for increasing the power of laser which has been hindered by the damage threshold of the laser gain material. A revolutionary step of progress has been made with the invention of chirped pulse amplification (CPA) technique in 1985<sup>[2]</sup>. Further on, for applications demanding high average laser power and high repetition rate, optical enhancement cavity (OEC) based on reflective optical elements become one of the most promising solutions. OEC is resonant Fabry-Perot cavity without gain medium inside. So it does not suffer from the limit rooted in the damage threshold of the gain medium. Besides the feature of power enhancement, laser beam inside OEC can reach high repetition rate which is especially beneficial for enhancing the signals in physical process that has low generation efficiency in single pass. The works in this thesis focus on developing high-average-power OECs aiming for application in Thomson scattering light sources.

### 1.2 Thomson Scattering Light Source

#### 1.2.1 Principles of Thomson Scattering

Thomson scattering<sup>[3]</sup>, here in this thesis more specifically designates inverse Compton scattering (ICS) between photons and electrons after which photons gain energy.

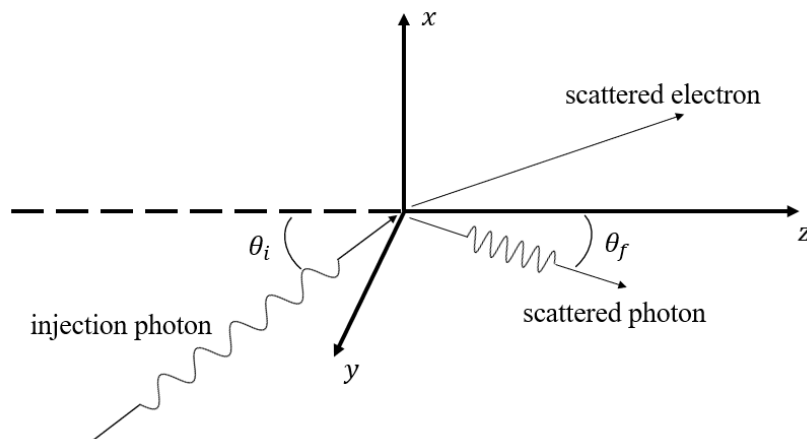


Figure 1.1 Schematic drawing of Thomson scattering in the initial-electron-at-rest frame.

In initial-electron-at-rest frame as shown in Fig. 1.1, the four momentum of the incident and scattered photon and electron are expressed as

$$\begin{aligned}
 \vec{P}_{\gamma i}^* &= (E_{\gamma i}^*, \vec{p}_{\gamma i}^*) = \frac{E_{\gamma i}^*}{c} (c, \sin \theta_i^*, 0, \cos \theta_i^*), \\
 \vec{P}_{ei}^* &= (E_{ei}^*, \vec{p}_{ei}^*) = \frac{m_0 c^2}{c} (c, 0, 0, 0), \\
 \vec{P}_{\gamma f}^* &= (E_{\gamma f}^*, \vec{p}_{\gamma f}^*) = \frac{E_{\gamma f}^*}{c} (c, \sin \theta_f^*, 0, \cos \theta_f^*), \\
 \vec{P}_{ef}^* &= (E_{ef}^*, \vec{p}_{ef}^*) = \frac{\gamma'^* m_0 c^2}{c} (c, \beta'^* \sin \phi^*, 0, \beta'^* \cos \phi^*).
 \end{aligned} \tag{1-1}$$

From energy conservation and momentum conservation, we have

$$\begin{aligned}
 E_{\gamma i}^* + E_{ei}^* &= E_{\gamma f}^* + E_{ef}^*, \\
 \vec{p}_{\gamma i}^* + \vec{p}_{ei}^* &= \vec{p}_{\gamma f}^* + \vec{p}_{ef}^*.
 \end{aligned} \tag{1-2}$$

Inserting Eq. 1-1 into Eq. 1-2, combining the energy-momentum relation of special relativity  $E^2 = (pc)^2 + (m_0 c^2)^2$ , the relation between energy of scattered photon with the energy of incident photon in initial-electron-at-rest frame can be derived as

$$E_{\gamma f}^* = \frac{m_0 c^2 E_{\gamma i}^*}{m_0 c^2 + E_{\gamma i}^* [1 - \cos(\theta_i^* - \theta_f^*)]}. \tag{1-3}$$

Applying the transformation of energy and angle between initial-electron-at-rest frame and laboratory frame as

$$\begin{aligned}
 E_{\gamma}^* &= \gamma E_{\gamma} (1 - \beta \cos \theta), \\
 \sin \theta^* &= \frac{\sin \theta}{\gamma (1 - \beta \cos \theta)}, \\
 \cos \theta^* &= \frac{\cos \theta - \beta}{1 - \beta \cos \theta},
 \end{aligned} \tag{1-4}$$

the relation between energy of scattered photon with the energy of incident photon in laboratory frame can be derived as

$$E_{\gamma f} = \frac{E_{\gamma i} (1 - \beta \cos \theta_i)}{(1 - \beta \cos \theta_f) + E_{\gamma i} [1 - \cos(\theta_i - \theta_f)] / E_{ei}}, \tag{1-5}$$

in which  $E_{ei} = \gamma m_0 c^2$  is the initial energy of electron in the laboratory frame. For head-on-collision backscattered photons,  $\theta_i = \pi$ ,  $\theta_f = 0$ , we have

$$E_{\gamma f} \simeq 4\gamma^2 E_{\gamma i}. \tag{1-6}$$

Benefited from this efficient mechanism of photon energy boost, it can be estimated that with incident laser wavelength of  $1 \mu\text{m}$ , X-ray photons with energy of  $\sim 100 \text{ keV}$  can

be generated through Thomson scattering by electron with energy of few tens of MeV. For generating X-ray photons, the needed energy of electron drops from the GeV scale of synchrotron light source<sup>[4-6]</sup> and free electron laser (FEL)<sup>[7-14]</sup> to few tens of MeV needed by Thomson scattering light sources. Proportionally the reduction of needed electron energy leads to reduction of cost and footprint. These make Thomson scattering light sources potentially capable of filling the gap in the current X-ray light sources between the low performance X-ray tubes and high performance synchrotron radiation light sources and FELs. Besides, this mechanism also enables Thomson scattering to generate photon with energy extending to gamma-ray range.

In addition to the advantage of compactness and effectiveness of Thomson scattering light sources, quasi-monochromatic X-rays can be obtained by using a diaphragm in the scattered photon beam path as the energy of scattered photon is correlated with scattering angle as exemplarily shown in Fig. 1.2.

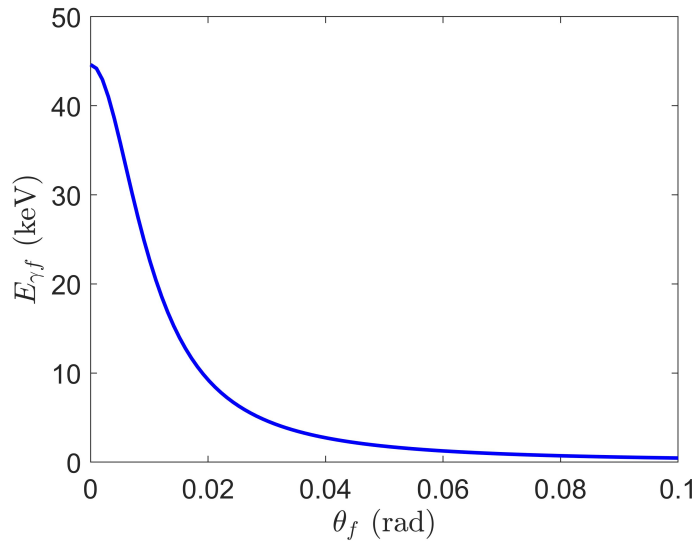


Figure 1.2 Relation between energy of Thomson scattered photon  $E_{\gamma_f}$  with scattered angle  $\theta_f$ , calculated with incident laser wavelength of  $1 \mu\text{m}$  head-on collision with electron beam of energy 50 MeV.

However, Thomson scattering light sources based on linac cannot satisfy the need of applications demanding high average flux. As the typical average flux of X-ray photons generated from linac based Thomson scattering light sources, with electron bunch charge of 1 nC, laser pulse energy 300 mJ, scattering repetition rate 10 Hz, round electron and laser beam with identical transverse Gaussian distribution and waist size of  $50 \mu\text{m}$ , can

be estimated to be

$$N_{\gamma f} = \frac{N_e N_L \sigma_T f_c}{4\pi \sigma_r^2} \simeq 1 \times 10^8 \text{ photons/s}, \quad (1-7)$$

in which cross section of Thomson scattering  $\sigma_T = \frac{8\pi}{3} r_e^2 \simeq 6.65 \times 10^{-29} \text{ m}^2$ , classical electron radius  $r_e = \left(\frac{e}{mc}\right)^2 = 2.82 \times 10^{-13} \text{ cm}$ <sup>[3]</sup>. To increase the average flux of Thomson scattering light source, a scheme combining optical enhancement cavity (OEC) and electron storage ring is proposed by Huang and Ruth in 1998<sup>[15]</sup> as the schematic drawing shown in Fig. 1.3. With this scheme, the average flux is increased in two folds: first the number of incident photon is increased through an optical enhancement cavity, second the repetition rate of Thomson scattering is increased from few Hz to few hundreds of MHz through the combination of optical enhancement cavity with electron storage ring.

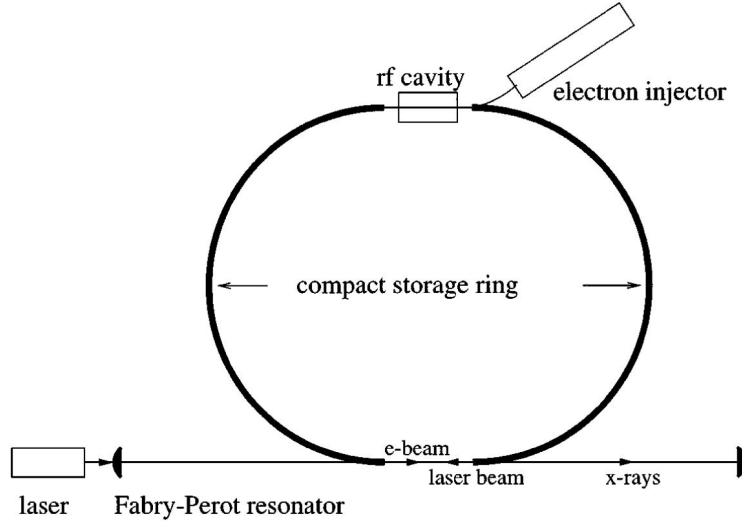


Figure 1.3 Schematic drawing of Thomson scattering light source combining optical enhancement cavity and electron storage ring<sup>[15]</sup>.

The works of this thesis are focusing on the theoretical and experimental studies of optical enhancement cavity for Thomson scattering light source. The demand of Thomson scattering for optical enhancement cavity can be inferred with the purpose of optimizing the average flux of scattered photon  $N_\gamma$  which has the following dependence<sup>[16][17]</sup>

$$N_{\gamma f} \propto \frac{N_e P_0 d}{A c E_{\gamma i}} \sigma_{\Delta E_{\gamma f}}, \quad (1-8)$$

in which  $N_e$  is the number of electrons,  $P_0$  is the laser pulse peak power,  $d$  is the interaction length,  $A$  is the transverse effective interaction area,  $c$  is speed of light, the cross section  $\sigma_{\Delta E}$  for an energy bandwidth  $\Delta E$  can be calculated from the integration  $\sigma_{\Delta E} = \int_{\Delta E} \frac{d\sigma}{dE_{\gamma f}} dE_{\gamma f}$  of which the energy dependent cross section derived by Klein and

Nishina<sup>[18]</sup> is expressed as

$$\frac{d\sigma}{dE_{\gamma f}} = \frac{\pi r_e^2}{2} \frac{1}{\gamma^2 E_{\gamma i}} \left[ \frac{E_{ei}^2}{4\gamma^2 E_{\gamma i}^2} \left( \frac{E_{\gamma f}}{E_{ei} - E_{\gamma f}} \right)^2 - \frac{E_{ei}}{\gamma^2 E_{\gamma i}} \frac{E_{\gamma f}}{E_{ei} E_{\gamma f}} + \frac{E_{ei} - E_{\gamma f}}{E_{ei}} + \frac{E_{ei}}{E_{ei} - E_{\gamma f}} \right]. \quad (1-9)$$

As it can be inferred from Eq. 1-8 that to increase the average flux of scattered photon it demands for optical enhancement cavity that:

1. the transverse size and longitudinal length of intra-cavity laser beam matching with that of the electron beam, which usually demands the intra-cavity laser beam has a waist with radius size around few tens of microns and pulse length at the order of picosecond;
2. to increase the laser pulse energy, which usually demands the OEC to have an hour-time-scale stable intra-cavity average power at the level of few hundreds of kilowatts.

All studies in the following part of this thesis are based on the purpose of realizing these two goals on OEC which is targeted for application in Thomson scattering.

## 1.2.2 Thomson Scattering Light Sources Based on Optical Enhancement Cavity

Currently, there are tens of Thomson scattering light sources which are based on traditional accelerators that are in operation, being under commissioning, or have been designed over the world, in which the key parameters of the ones based on OEC are summarized in Table 1.1. The two Thomson scattering light sources, ThomX and TTX, on which the works of this thesis are based on will be more detailedly introduced in Section.1.2.3 and Section 1.2.4.

Compact Light Source (CLS)<sup>[19-20]</sup> is the commercial product of Thomson scattering X-ray light source manufactured by Lyncean Technologies Inc., USA. The photo and layout of CLS are shown in Fig. 1.4 and Fig. 1.5 respectively. CLS is featured as combining OEC with electron storage ring. The OEC of CLS is in a four-mirror planar bow-tie structure with a round trip length of 4.6 m. It is working at an intra-cavity average power of 300 kW, corresponding to a cavity gain of  $\sim 10000$  for an injection laser average power of 30 W. Flux of X-ray is  $\sim 3 \times 10^{10}$  photons/s with full bandwidth.

New Electron STORage Ring (NESTOR)<sup>[23]</sup> is a Thomson scattering light source now under commissioning, located in Ukraine. NESTOR is based on OEC and electron storage ring. The layouts of NESTOR and the OEC are shown in Fig. 1.6 and Fig. 1.7

Table 1.1 Summary of key parameters of Thomson scattering light sources which are based on OEC, in which  $E_{ei}$  is the energy of incident electron,  $\lambda$  is the wavelength of the incident laser,  $P_c$  is the average laser power inside OEC,  $\tau_L$  is the pulse length of laser inside OEC,  $f_c$  is the scattering repetition rate,  $E_{\gamma f}$  is the cut-off energy of scattered X-ray photons.

Name	Accelerator Type	$E_{ei}$ (MeV)	$\lambda$ (nm)	$P_c$ (kW)	$\tau_L$ (ps)	$f_c$ (MHz)	$E_{\gamma f}$ (keV)	Flux (ph/s)
CLS <sup>[19-20]</sup>	Ring	25-50	1064	300	25	65	8-42	$10^{10}$
ThomX <sup>[21]</sup>	Ring	50-70	1030	700	5	17.84	46-90	$10^{13}$
TTX <sup>[22]</sup>	Ring	50	1064	300	20	52.93	45	$10^{10}$
NESTOR <sup>[23]</sup>	Ring	40-225	1064	/	/	19.46	30-900	$10^{13}$
MightyLaser <sup>[24-25]</sup>	Ring	1280	1030	30	11.4	1.08	24000	$10^8$
LUCX <sup>[26-27]</sup>	Linac	18-24	1064	2.45	7	0.0125	6-10	$10^6$
cERL <sup>[28]</sup>	ERL	20	1064	10	10	162.5	6.95	$10^7$
BriXS <sup>[29-30]</sup>	ERL	100	1030	500	2	100	20-180	$10^{13}$

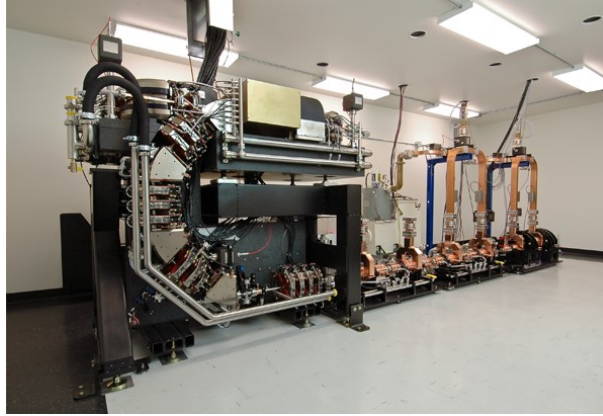


Figure 1.4 Photo of Lyncean CLS<sup>[19]</sup>.

respectively. The OEC of NESTOR is designed to be with two-mirror structure with a round trip length of 0.812 m. Each cavity mirror is with reflectivity of 99.9 %. Injection laser average power is 10 W. The average flux of the scattering generated X-ray is expected to be  $10^{13}$  photons/s with full bandwidth.

MightyLaser<sup>[24-25]</sup> is a Thomson scattering gamma-ray source demonstrated at KEK, Japan but has been dismantled in 2014<sup>[31]</sup>. The layouts of MightyLaser and the OEC are shown in Fig. 1.8 and Fig. 1.9 respectively. The OEC of MightyLaser is in a four-mirror nonplanar tetrahedron structure with a round trip length of 1.68 m. The nonplanar tetrahedron structure of OEC is chosen for maintaining a circularly polarized laser beam inside thus to generate circularly polarized gamma-ray beam. The OEC is working at

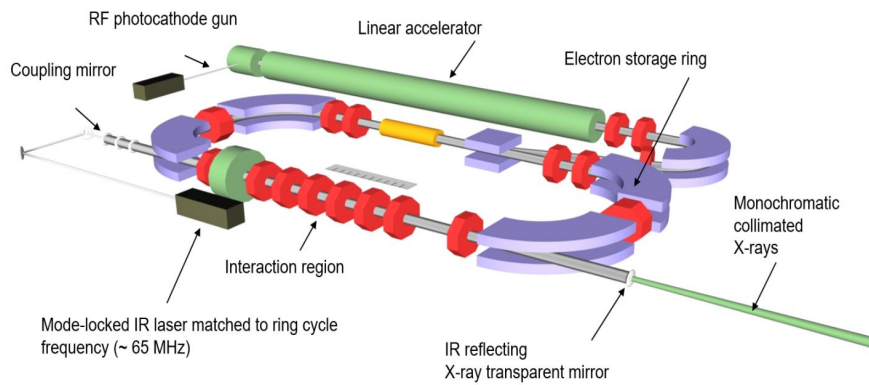


Figure 1.5 Layout of Lyncean CLS<sup>[19]</sup>.

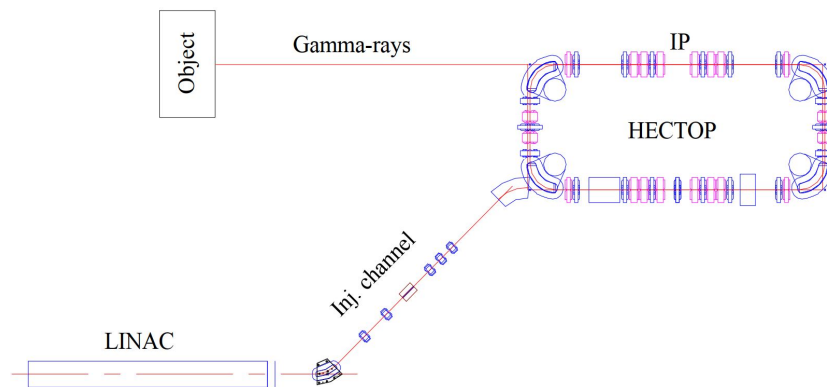


Figure 1.6 Layout of NESTOR<sup>[23]</sup>.

an intra-cavity average power of 30 kW, corresponding to a cavity gain of  $\sim 550$  for an injection laser average power of 54 W. The laser pulse inside OEC is interacting with electron beam with energy of 1.28 GeV from damping ring of Accelerator Test Facility (ATF) with a collision rate of 1.08 MHz. Flux of gamma-ray is up to  $(3.5 \pm 0.3) \times 10^8$  photons/s with full bandwidth.

Laser Undulator Compact X-ray source (LUCX)<sup>[26-27]</sup> is a Thomson scattering X-ray light source now in operation at KEK, Japan. The layouts of LUCX facility and the OEC are show in Fig. 1.10 and Fig. 1.11 respectively. The OEC of LUCX is in a four-mirror

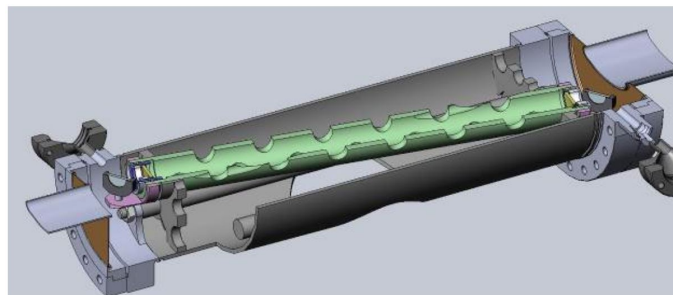


Figure 1.7 Layout of NESTOR OEC<sup>[23]</sup>.

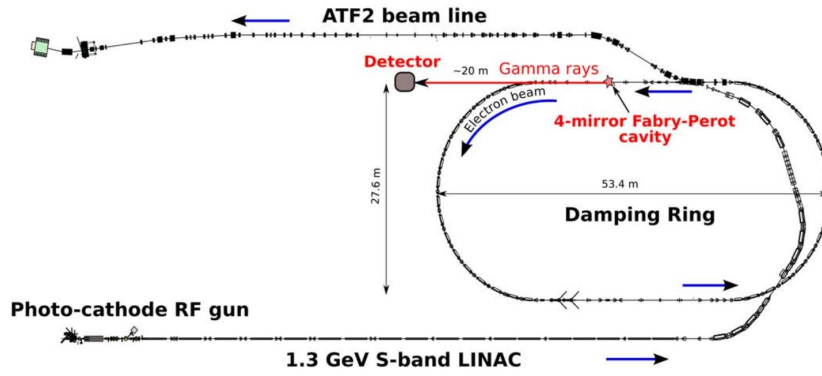


Figure 1.8 Layout of MightyLaser<sup>[25]</sup>.

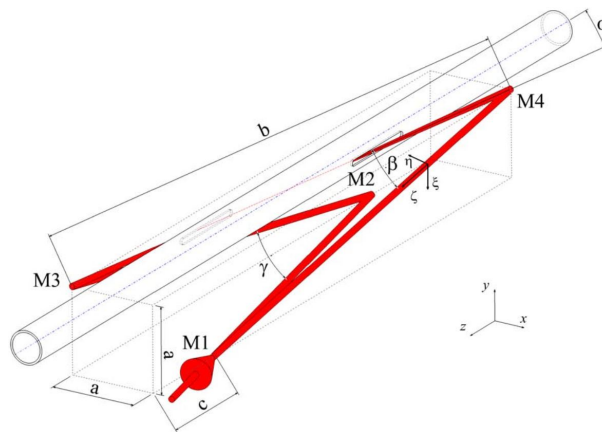


Figure 1.9 Layout of MightyLaser OEC<sup>[25]</sup>.

planar bow-tie structure. It is working at a burst mode<sup>[32]</sup> with a peak intra-cavity power of 250 kW with 357 MHz repetition rate, interacting with electron beam at repetition rate of 12.5 Hz with 1000 bunch spacing with 2.8 ns. Flux of X-ray is  $3 \times 10^6$  photons/s with full bandwidth.

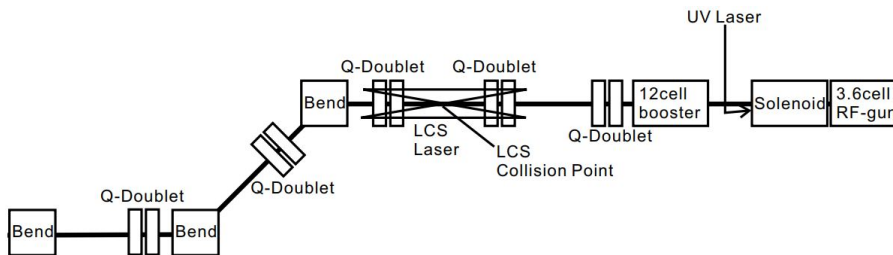


Figure 1.10 Layout of LUCX<sup>[26]</sup>.

cERL<sup>[28]</sup> is a Thomson scattering light source based on interaction between laser beam in OEC and electron beam from energy recovery linac (ERL) at KEK, Japan. The layout of cERL and structure of OEC are shown in Fig. 1.12 and Fig. 1.13 respectively. The OEC of cERL is in a four-mirror planar bow-tie structure with a round trip length of 1.845 m. It is working at an intra-cavity average power of 10.4 kW, corresponding

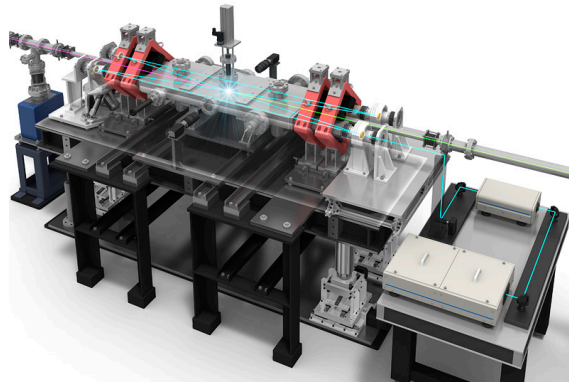


Figure 1.11 Layout of LUCX OEC<sup>[27]</sup>.

to a cavity gain of 430 for an injection laser average power of 24 W. Flux of X-ray is  $(2.6 \pm 0.1) \times 10^7$  photons/s with full bandwidth.

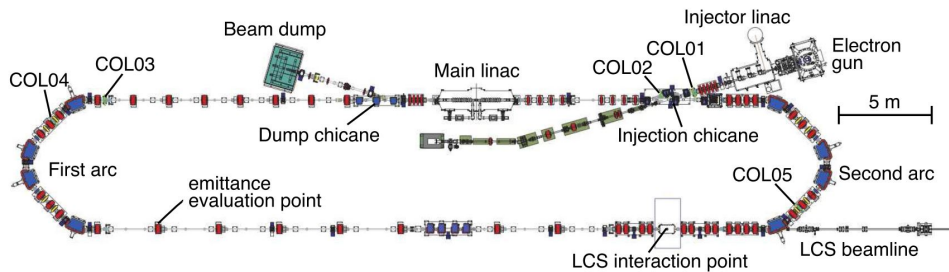


Figure 1.12 Layout of cERL<sup>[28]</sup>.

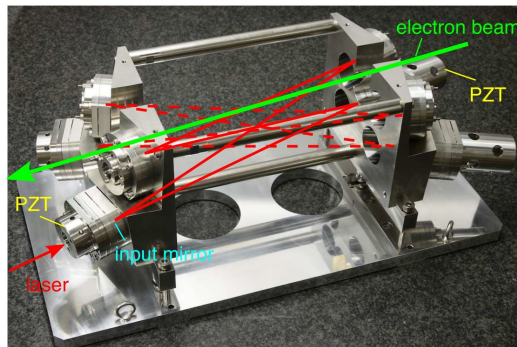


Figure 1.13 Layout of cERL OEC<sup>[28]</sup>.

Bright compact X-ray source (BriXS)<sup>[29-30]</sup> is a Thomson scattering light source that has been designed to be built in Italy. The layout of BriXS and scheme of optical enhancement cavity are shown in Fig. 1.14. BriXS consists of two symmetric beam lines. Each line generates X-rays through Thomson scattering between laser beam inside OEC and electron beam from ERL. The OEC of BriXS is designed to be with four-mirror planar bow-tie structure with a round trip length of 3 m. It is designed to be working at an average

power of 500 kW, corresponding to a cavity gain of 7700 for an injection laser average power of 65 W. The flux of X-ray is designed to be  $4.7 \times 10^{12}$  photons/s for 5% bandwidth and  $1 \times 10^{13}$  for 10% bandwidth.

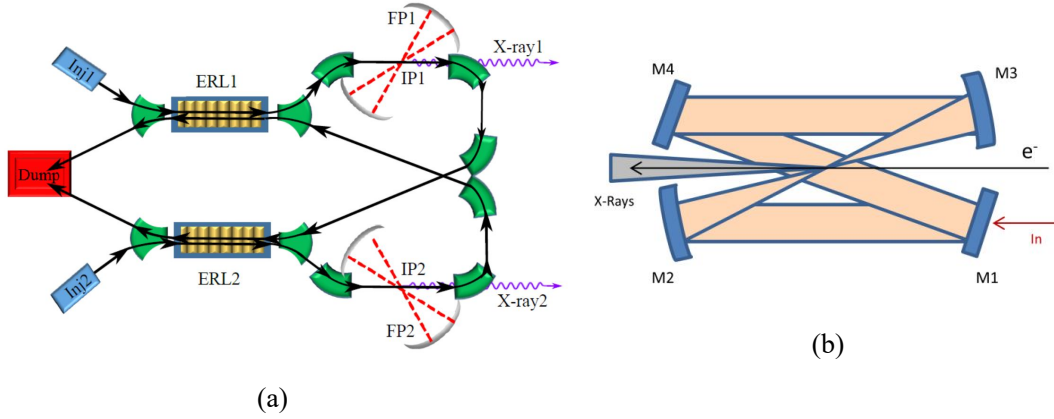


Figure 1.14 (a) Layout of BriXS, (b) scheme of BriXS OEC<sup>[30]</sup>.

### 1.2.3 ThomX

ThomX<sup>[21]</sup> is a Thomson scattering light source which is now under commissioning, located inside campus of Paris-Saclay University at Orsay, France. The layouts of ThomX and the OEC are shown in Fig. 1.15 and Fig. 1.16 respectively. Key parameters of ThomX are summarized in Table 1.2. The OEC of ThomX is in a four-mirror planar bow-tie structure with a round trip length of 8.4 m. It will be working at an intra-cavity average power up to 700 kW, corresponding to a cavity gain of 10000 for an injection laser average power of 100 W. Flux of X-ray is expected to be  $3 \times 10^{13}$  photons/s with full bandwidth.

On the optical enhancement cavity side, before the commissioning of the OEC of ThomX, extensive R&D works have been done on a prototype OEC called SBOX. Studies based on the experimental setup of SBOX will be introduced in Chapter 4 and Chapter 5.

### 1.2.4 TTX

Tsinghua Thomson scattering X-ray source (TTX)<sup>[22]</sup> is a Thomson scattering light source which is currently based on a 45 MeV linac and terawatt laser system and being planned for upgrade to a configuration combining OEC and electron storage ring, located inside campus of Tsinghua University at Beijing, China. The photo and layout of TTX are shown in Fig.1.17,1.18 respectively and key parameters are summarized in Table 1.3. Currently, R&D works have been progressed independently on the sides of optical en-

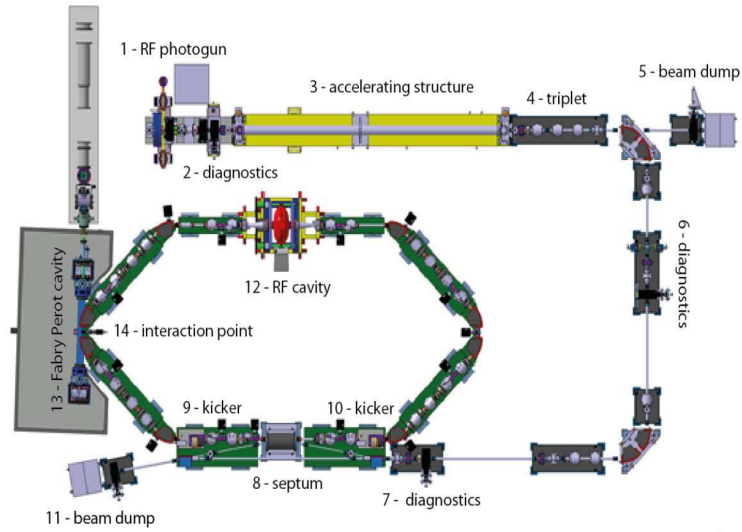


Figure 1.15 Layout of ThomX<sup>[21]</sup>.

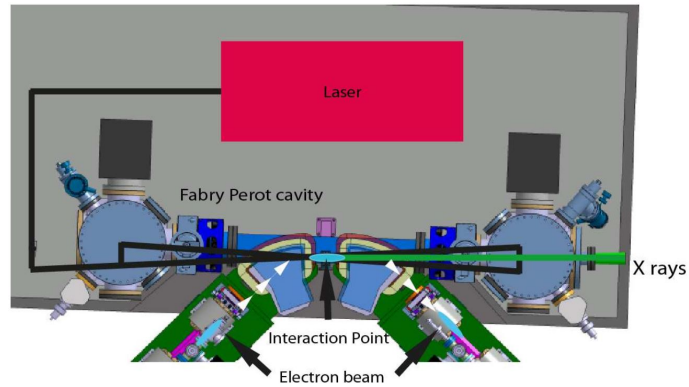


Figure 1.16 Layout of ThomX OEC<sup>[21]</sup>.

hancement cavity<sup>[33][34]</sup> and electron storage ring<sup>[35][36]</sup>.

Studies on the optical enhancement cavity of TTX will be presented in Chapter 6, including the full design of the experimental setup of the prototype OEC called TBOX and the preliminary experiment carried out on it, design for high power experimental setup of TBOX and the design of OEC which will be combined with TTX electron storage ring.

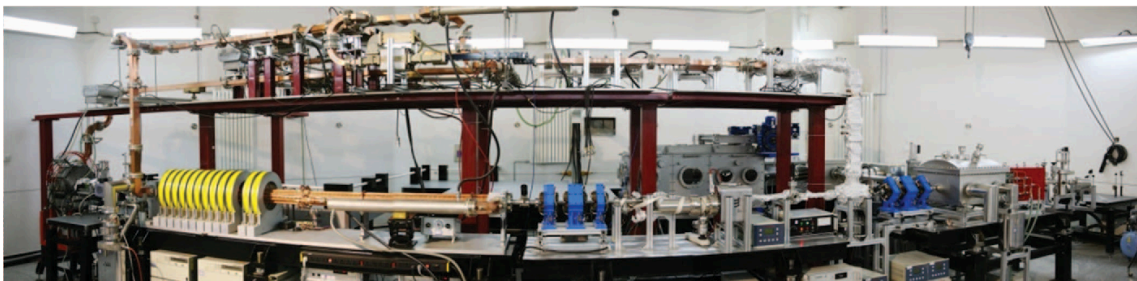
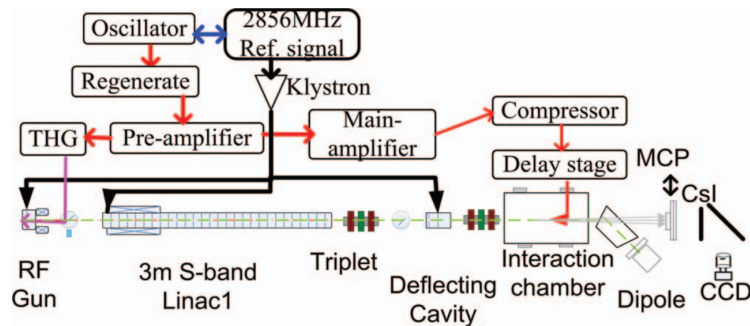


Figure 1.17 Photo of TTX<sup>[22]</sup>.

Table 1.2 Key parameters of ThomX<sup>[21]</sup>.

Parameter	Value
Electron energy	50 MeV
Circumference of electron storage ring	16.8 m
Electron beam current	17.84 mA
Laser wavelength	1030 nm
Laser and OEC repetition rate	35.68 MHz
Injection laser power	50-100 W
Injection laser pulse energy	1.4-2.8 $\mu$ J
Laser pulse energy inside OEC	28 mJ
Laser pulse length inside OEC	5 ps (rms)
OEC finesse/ Gain	3000-30000/ 1000-10000
Laser waist diameter inside OEC	70 $\mu$ m
Laser power inside OEC	70-700 kW
Energy of X-ray photons	46-90 keV
Total flux of X-ray photons	$10^{11} - 10^{13}$ photons/s

Figure 1.18 Layout of TTX<sup>[22]</sup>.

### 1.3 Development Status of Optical Enhancement Cavity

The development of OECs can be classified in terms of several dimensions. In terms of geometrical structure, the OECs can be in planar structure to maintain linearly polarized laser beam inside, or nonplanar tetrahedron structure to maintain circularly polarized laser beam inside. In terms of number of cavity mirrors, the OECs can be with two mirrors, three mirrors, four mirrors, six mirrors and more. In terms of laser beam temporal structure inside OECs, it can be in continuous wave, pulsed wave and burst mode. In terms of laser wavelength, most commonly OECs are injected with 1  $\mu$ m-wavelength lasers amplified by Yb: fiber amplifiers possessing the features both of high average power and high repetition

Table 1.3 Key parameters of TTX<sup>[22]</sup>.

Parameter	Value
Electron energy	46.7 MeV
Electron bunch charge	1 nC
Electron bunch length	2.7 ps (rms)
Laser wavelength	800 nm
Laser pulse energy	300 mJ
Laser pulse length	356 fs (FWHM)
Laser spot size	100 $\mu\text{m}$ (rms)
Energy of X-ray photons	30-50 keV
Yield of X-ray photons	$10^7$ per pulse

rate, also OECs exist being injected with laser of central wavelength of 355nm, 532 nm, 800 nm and 10  $\mu\text{m}$ .

In this section, to provide a comprehensive view of the current development status of OEC, representative works of OECs are introduced including the OECs with a application background different from Thomson scattering light sources, OECs with no targeted application but with specialized features and the representative experimental OEC works that have been done in China.

### 1.3.1 Development of Optical Enhancement Cavity in Different Fields

Besides Thomson scattering light source, optical enhancement cavity can be applied in wide range of applications in the frontier of scientific research. In this section, developments status will be introduced for optical enhancement cavity applied in different fields including pulsed wave OEC for high-order harmonic generation (HHG), continuous wave OEC for gravitational wave detection, steady-state microbunching (SSMB) light source, fusion energy experiment and Compton polarimeter.

High-order harmonic generation (HHG) can be realized by interaction between laser and noble gas, which demands for a laser power density  $> 10^{14}$  W/cm<sup>2</sup><sup>[37]</sup>. To realize this power density, the laser beam inside OEC is typically with a pulse length of  $\sim 100$  fs, waist size of few tens microns and an intra-cavity average power of few kilowatts, as the key parameters of representative cavity-enhanced HHG experiments summarized in Table 1.4. An OEC with bow-tie structure is commonly adopted by experimental setup for HHG to have a small laser beam waist inside OEC. The single pass efficiency of HHG

is limited to  $\sim 10^{-6}$ <sup>[38]</sup>. With cavity-enhance, HHG can be produced with repetition rate  $>10$  MHz to greatly increase the average flux of the HHG photons. Currently, most commonly used OECs for HHG are with laser wavelength of  $1 \mu\text{m}$ , which is resulted from the available laser possessing properties of both high-average-power and high-repetition-rate now limited to Yb: fiber laser. So the cavity-enhanced HHG photon is now limited to energy up to extreme ultraviolet (EUV), since the higher energy of HHG photon favors longer wavelength of incident laser. The obtained HHG radiation can be used for photoelectron spectroscopy (PES)<sup>[39]</sup> to be able to detect electron dynamic in attosecond time scale. Typical OEC for HHG experiment with few kilowatts intra-cavity average power is maintained for few minute time scale<sup>[39]</sup>.

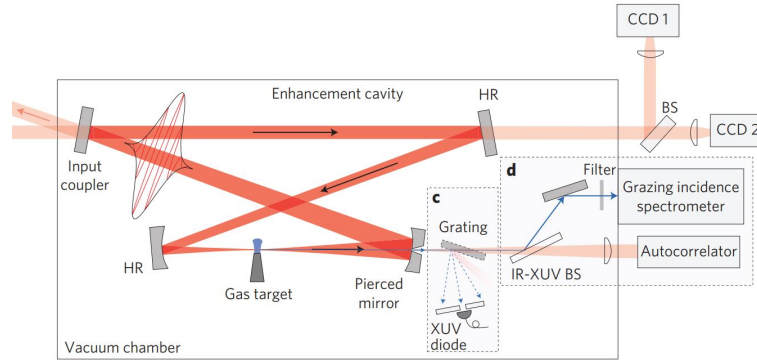


Figure 1.19 Typical layout of OEC for HHG experiment<sup>[40]</sup>.

Table 1.4 Summary of key parameters of representative cavity-enhanced high-order harmonic generation experiments, in which  $\lambda$  is the wavelength of the incident laser into the noble gas,  $P_c$  is the average intra-cavity laser power of OEC used for HHG,  $\tau_L$  is the intra-cavity pulse length,  $f_h$  is the repetition rate of the HHG,  $E_{\gamma h}$  is the energy of the HHG photon.

Experiments at	$\lambda$ (nm)	$P_c$ (kW)	$\tau_L$ (fs)	$f_h$ (MHz)	$E_{\gamma h}$ (eV)	Flux (photons/s)
MPQ <sup>[39]</sup>	1030	2.8	40	18.4	60	$10^{13}$
JILA <sup>[41]</sup>	1070	8	120	154	30	$10^{11}$
Stony Brook Univ. <sup>[42]</sup>	1035	11	155	88	37	$10^{11}$
Univ. British Columbia <sup>[43]</sup>	1045	10	120	60	40	$10^{11}$
Univ. Tokyo <sup>[44]</sup>	1040	1	200	10	41	$10^{13}$

Gravitational wave (GW) can be detected through measurement of phase difference of continuous wave laser in the two arms of Michelson interferometer, the signal of which is further enhanced through using long-distance OECs as interferometer arms<sup>[45]</sup>. Typical



Table 1.5 Summary of key parameters of currently running gravitational wave detection observatories, in which  $\lambda$ ,  $l_c$ , Finesse and  $P_c$  respectively represent the laser wavelength, arm cavity length, cavity Finesse and intra-cavity average power of the arm OEC of the interferometer;  $f_{GW}$  is the gravitational wave detection range,  $h$  is the strain sensitivity, BNS range is the detectable distance of gravitational wave signal emitted by a binary neutron star (BNS) coalescence.

Observatory	Advanced LIGO <sup>[48]</sup>	Advanced VIRGO <sup>[49]</sup>
$\lambda$ (nm)	1064	1064
$l_c$ (km)	4	3
Finesse	450	443
$P_c$ (kW)	750	700
$f_{GW}$	10 Hz - 7 kHz	10 Hz - 10 kHz
$\tilde{h}$ ( $\text{Hz}^{-1/2}$ )	$10^{-23}$ @100 Hz	$10^{-23}$ @100 Hz
BNS range (Mpc)	210	140

crowave in the conventional accelerator with optical wave, the spacing of electron bunch stabilized around the zero-crossing point of the electromagnetic field and the bunched beam length decrease typically five to six orders of magnitude. The high brightness results from the coherent radiation from the short bunch. The high repetition rate results from the combination with electron storage ring. Radiation can be generated by SSMB with a wavelength range from IR to EUV, in which a key application is EUV generation for lithography. There are mainly two schemes being under studied for now: longitudinal strong focusing<sup>[51]</sup> and reversible<sup>[52]</sup>. In longitudinal strong focusing scheme, a quasi-isochronous lattice with low alpha is designed for realizing and maintaining the microbunch state inside the electron storage ring. Whereas in reversible scheme, low-alpha lattice is not needed, the electron beam is demicrobunched after radiator to be sent back to the ring. In both schemes, OEC serves for providing modulating electric field in the modulator, which demands for an continuous wave intra-cavity average power of  $\sim 1$  MW and a phase stability characterized by linewidth  $< 10$  kHz.

Neutral beam system will provide heating and current drive for the future DEMOstration fusion reactor (DEMO)<sup>[54]</sup>. To increase the efficiency of the fusion reactor, it is a major requirement to increase the efficiency of the neutral beam system to be with a wall-plug-efficiency higher than 60%. A scheme of neutral beam system based on photoneutralization that utilizes high power continuous wave laser beam to neutralize  $D^{-1}$  beam is proposed<sup>[54]</sup>. The implementation of a photoneutralizer in a fusion reactor building is

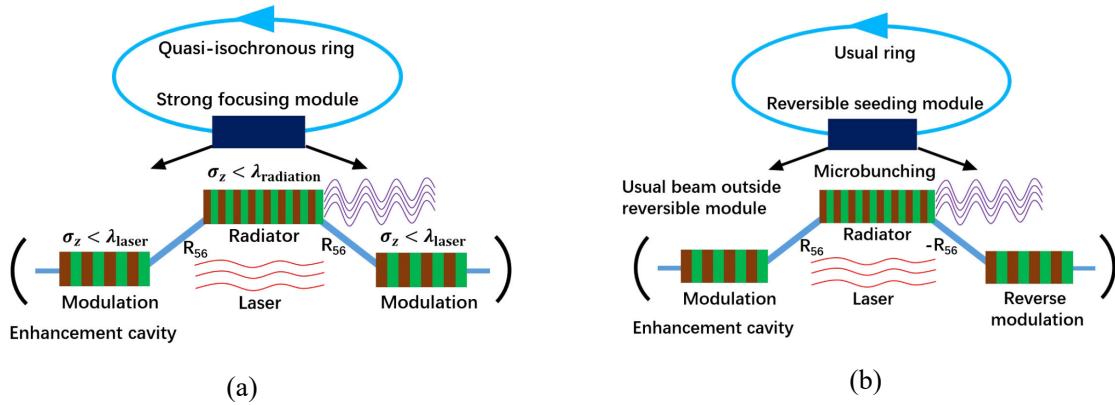


Figure 1.21 Schematic layouts of SSMB of (a) longitudinal strong focusing scheme and (b) reversible scheme<sup>[53]</sup>.

shown in Fig. 1.22. The layout of a OEC in the photoneutralizer is shown in Fig. 1.23. The OEC of DEMO is in a four-mirror planar bow-tie structure with a round trip length of 100 m minimum. The laser beam size is nearly constant in the interaction region with diameter of 1 cm as with a Rayleigh length of  $\sim 15$  m. An intra-cavity average power of 3 MW is corresponding to realization of 50% of neutralization rate for a  $1\text{MeV } D^{-1}$  beam sheet of 1 cm. Duplication with a second and third OEC will lead to a 75% and 87.5% neutralization rate respectively. The OEC is envisaged to be working with a 1 kW continuous wave injection laser and a cavity finesse of 10000.

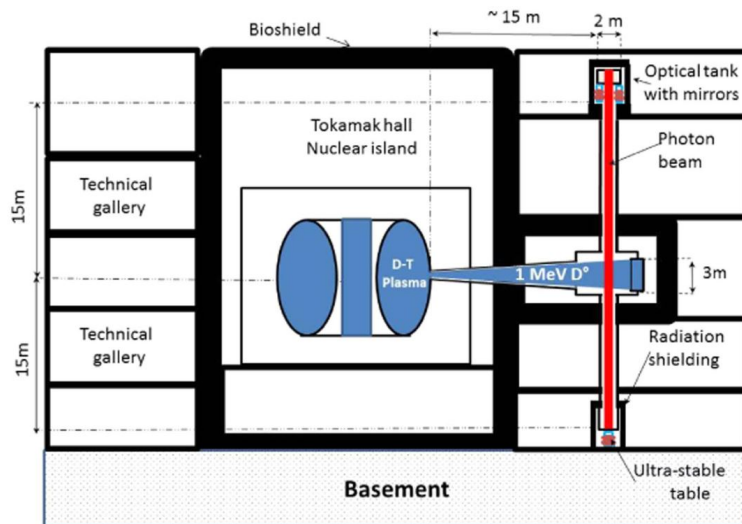


Figure 1.22 Implementation of a photoneutralizer in a fusion reactor building<sup>[54]</sup>.

Optical enhancement cavity can be used for Compton polarimeter to detect polarization of electron beam<sup>[55-56]</sup>. Layout of a Compton polarimeter at Jefferson Lab is shown in Fig. 1.24<sup>[57]</sup>. The OEC is in a two-mirror symmetry structure with a round trip length

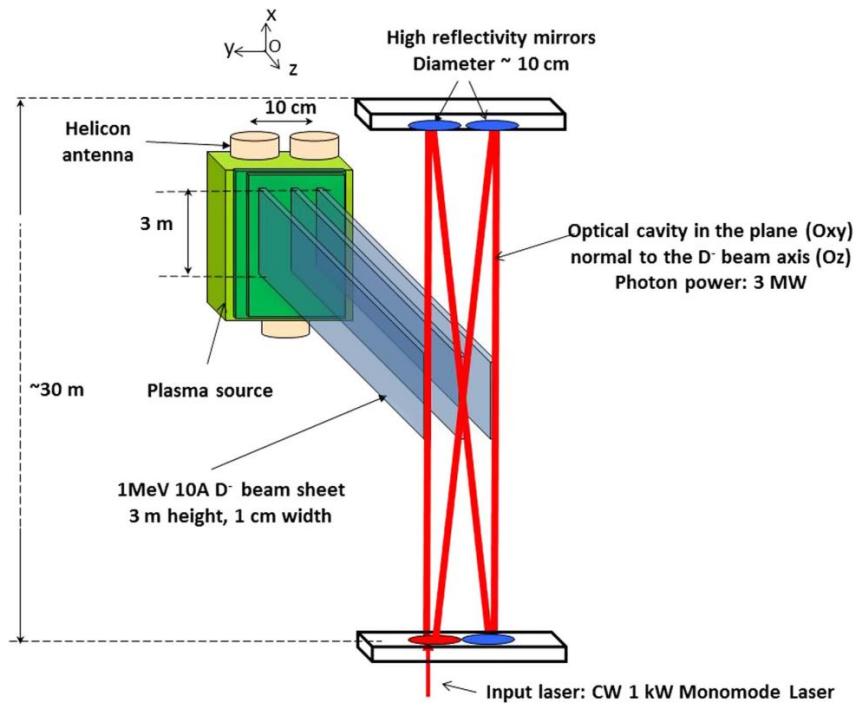


Figure 1.23 Layout of a OEC in the photoneutralizer<sup>[54]</sup>.

of 1.7 m. It is injected with continuous wave laser with central frequency of 532 nm and average power of 1.74 W. The intra-cavity average power is enhanced to 3.7 kW with a cavity gain of 3800. A precision of 1.0 % can be achieved for polarization measurement for electron beam with energy of 1.06 GeV and current of 50  $\mu$ A.

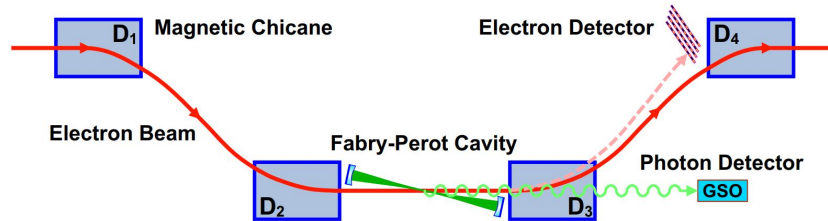


Figure 1.24 Layout of Compton polarimeter at Jefferson Lab<sup>[57]</sup>.

### 1.3.2 Development of Optical Enhancement Cavity with Specialized Features

Besides the OECs with a targeted application, experiments have been done on OECs to explore the specialized features of OEC itself. Representative works are introduced in this Section including realizing high intra-cavity average power to megawatt scale, locking with incident laser wavelength other than the commonly used 1  $\mu$ m but of 355 nm, 800 nm and 10  $\mu$ m, and with simultaneous locking to two different wavelength incident

lasers.

Megawatt-scale intra-cavity average power was realized at Max-Planck-Institute for Quantum Optics (MPQ) on experimental setup as schematically shown in Fig. 1.25<sup>[58]</sup>. The OEC is in a four-mirror planar bow-tie structure. Injection laser is with central wavelength of 1040 nm and average power up to 420 W. An intra-cavity average power of 400 kW was realized with 250 fs pulses at an input power of 315 W, corresponding to a cavity gain of 1270. And average power of 670 kW was realized with 10 ps pulses. At high power state, the cavity fundamental mode is distorted with resonant coupling to high order modes. Further increase of the intra-cavity average power was prevented by damage threshold of the input coupling mirror.

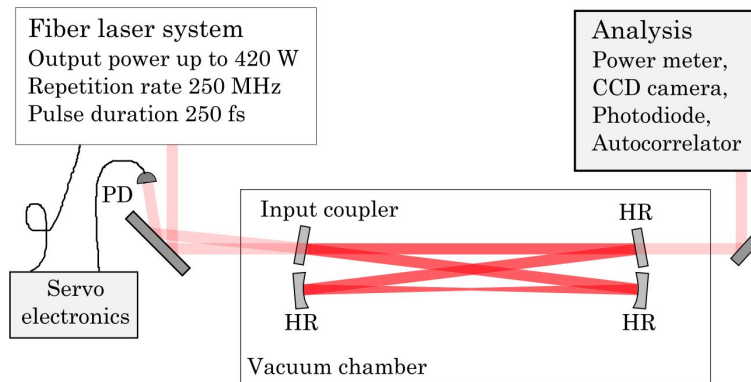


Figure 1.25 Schematic drawing of experimental setup of the OEC realizing megawatt-scale intra-cavity average power at MPQ<sup>[58]</sup>.

Experiment of OEC to enhance laser with central wavelength of 800 nm is done at JILA on experimental setup schematically shown in Fig. 1.26<sup>[59]</sup>. The OEC is in a six-mirror planar bow-tie structure with a round trip length of 3.95 m. An intra-cavity average power of 50 W is realized, corresponding to a cavity gain of 100 with an incident laser average power of 500 mW. Intra-cavity laser pulse length is measured to be 3.4 ps with FWHM of Gaussian fit.

Experiment of OEC to enhance laser wavelength of 10  $\mu\text{m}$  was done at Waseda University, Japan<sup>[60]</sup>. A structure of OEC with three-mirror as shown in Fig. 1.27 is selected. GaAs mirror is used as input coupling mirror which realizes small loss and large transmission. Cavity is diagnosed with the transmission of ZnSe mirror. As the reflection of Si substrate mirror varies with laser incident angle, it is optimized with slightly changing the incident angle. An intra-cavity average power of 2.3 kW is realized, corresponding to a cavity gain of 200 with an incident laser average power of 11 W.

Experiment of OEC to simultaneously enhance two laser beams with different wave-

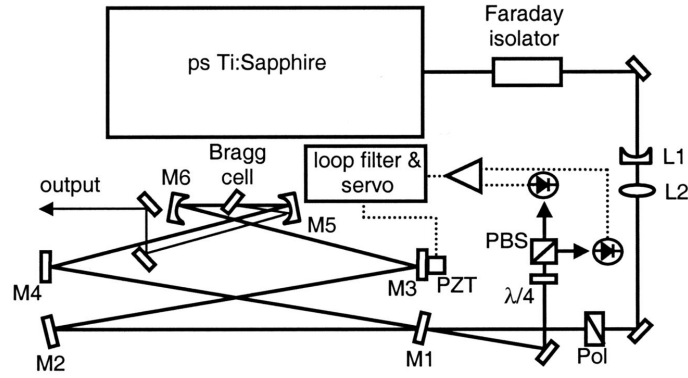


Figure 1.26 Schematic drawing of experimental setup of the OEC to enhance laser with central wavelength of 800 nm at JILA<sup>[59]</sup>.

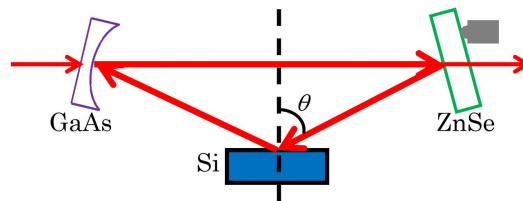


Figure 1.27 Schematic drawing of OEC for enhancing laser with central wavelength of 10  $\mu\text{m}$ <sup>[60]</sup>.

lengths is done at Oak Ridge National Laboratory, USA<sup>[61]</sup>. The OEC is in two-mirror structure with a round trip length of 0.75 m. The demonstrated experiment is done with cavity mirrors coated with dual-wavelength HR coating at 1064 nm and 355 nm. Error signal for the PDH feedback<sup>[62-63]</sup> is generated from the cavity reflection signal of IR beam. And the frequency of the IR beam is tuned through an acousto-optic frequency shifter to realize the lock. Enhancement factor of 110 is realized for 533 nm laser. The demonstrated technique can be applied to multiple incident laser beams with different wavelengths and different temporal structures.

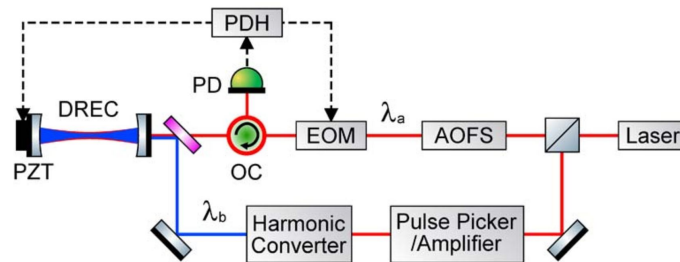


Figure 1.28 Experimental setup of the OEC to simultaneously enhance two laser beams with different wavelengths<sup>[61]</sup>.

### 1.3.3 Development of Optical Enhancement Cavity in China

Developments of OECs have been carried out in several institutions in China. Two representative experimental works are presented in this section.

Experimental work of OEC has been done in Institute of Physics, Chinese Academy of Science (CAS) in 2015<sup>[64]</sup>. The experimental setup of this OEC is shown in Fig. 1.29. It is in a four-mirror planar bow-tie structure with a round trip length of 1.76 m. Cavity mirrors  $M_1$  and  $M_4$  are planar,  $M_2$  and  $M_3$  are concave with radius of curvature (ROC) of 100 mm. The cavity is injected with pulsed wave Ti:Sapphire laser with wavelength centered at 826 nm, repetition rate of 170 MHz and pulse length of 80 fs. A cavity gain of 24 is realized with intra-cavity power of 24 W. BBO crystal is placed at the waist position between  $M_2$  and  $M_3$ , and doubled-frequency laser is obtained for an average power of 392 mW.

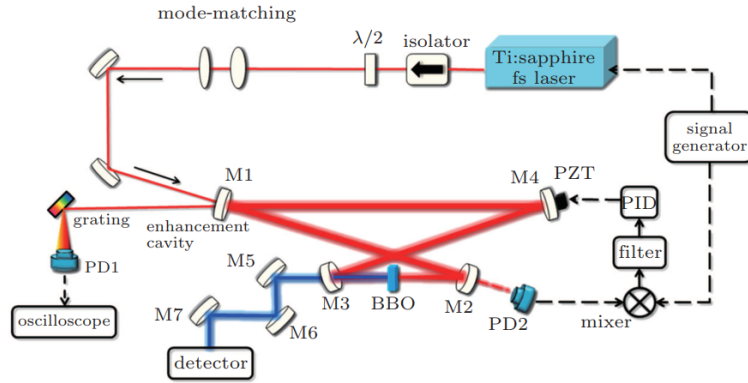


Figure 1.29 Experimental setup of the OEC built in Institute of Physics, CAS in 2015<sup>[64]</sup>.

Experimental work of OEC has also been done in Wuhan Institute of Physics and Mathematics, CAS in 2019<sup>[65]</sup>. The experimental setup of this OEC is shown in Fig. 1.30. It is in a six-mirror planar bow-tie structure with a round trip length of 3 m. Cavity mirrors MC, MD, ME and MF are planar, MA and MB are concave with ROC of 10 cm and 15 cm respectively. The cavity is injected with pulsed wave Yb: fiber laser with wavelength centered at 1038 nm, repetition rate of 100 MHz and pulse length of 100 fs. A cavity gain of 225 is realized with intra-cavity average power of 6.08 kW. Noble gas of Xe is introduced in the focus region, and HHG signal is observed.

As we can see from the above introduced works on optical enhancement cavity, it is still challenging to realize an intra-cavity average power of few hundreds of kilowatts stably stored inside OEC for hour time scale. Realizing this goal and solving the related issues of thermal instabilities will be the focus of the works in this thesis.

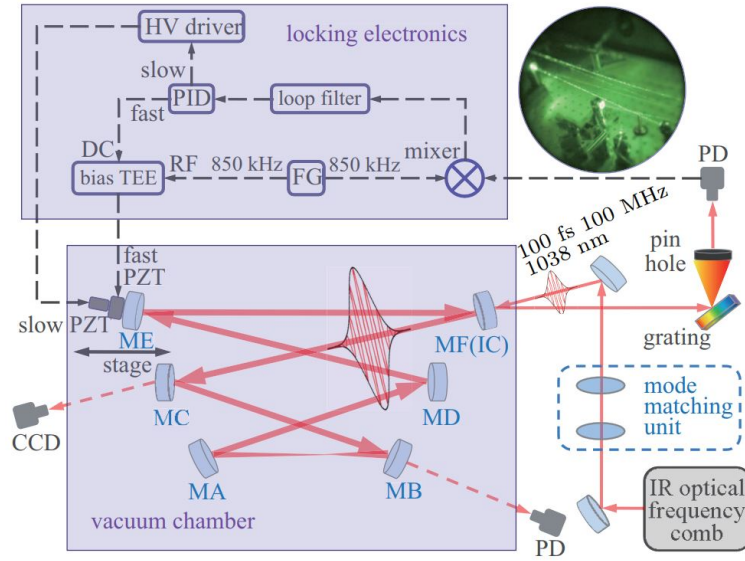


Figure 1.30 Experimental setup of the OEC built in Wuhan Institute of Physics and Mathematics, CAS in 2019<sup>[65]</sup>.

## 1.4 Focus of Dissertation

### 1.4.1 Main Work

This thesis focuses on theoretical and experimental works of developing a high-average-power optical enhancement cavity aiming for application in Thomson scattering light sources.

In Chapter 2, the fundamental principles and properties of optical enhancement cavity are introduced to establish a theoretical framework of this thesis. First, the properties of cavity itself are introduced including stability condition, cavity mode and cavity frequency comb. Then cavity enhancements with continuous wave (CW) injection and pulsed wave (PW) injection are analyzed separately. Coupling of injection laser beam into the cavity is analyzed from transverse mode matching with telescope and longitudinal phase locking with PDH technique respectively.

In Chapter 3, for a small laser beam waist with radius size of few micrometers inside optical enhancement cavity that is needed by Thomson scattering, an expression of highly focused linearly polarized laser field with nonparaxial correction derived through a generalized Lax series expansion method is presented which could be used for simulation of Thomson scattering to improve simulation precision and speed.

In Chapter 4, the experimental setup of prototype cavity of ThomX, called SBOX, is presented. During experiment, the injection laser power is gradually increased to increase the intra-cavity laser power. Modal instabilities began to show when intra-cavity average

power reaches around 100 kW. The experimentally observed modal instabilities can be well described with mode degeneracy induced by mirror surface thermoelastic deformation. Method of D-shape mirror is brought up to be implemented close to the optical path between cavity mirrors to break the boundary conditions of high order modes which are degenerated with the ideal cavity working mode  $TEM_{00}$ . Through simulation of cavity mode done with ANSYS and OSCAR code, the capability of D-shape mirror for modal instabilities suppression is well proved and the experimental data of intra-cavity power change versus D-shape mirror position is well recovered. High power experiment was launched with implementation of D-shape mirrors inside SBOX cavity, an hour-time-scale stable intra-cavity average power of 200 kW was realized.

In Chapter 5, after achieving the 200 kW intra-cavity average power in 2018, with the purpose of investigating the reason of cavity gain decrease, extensive R&D works were done on the SBOX experimental setup with implementation of the pair of D-shape mirrors. A prior-damage phenomenon is observed in 2019. The phenomenon behaves with fast intra-cavity average power drop with magnitude and time scale depending on the power level. Increasing further the incident laser power led to irreversible damage of the cavity coupling mirror surface. The origin of this phenomenon is investigated with *post mortem* mirror surface imaging and analysis of the signals reflected and transmitted by the optical enhancement cavity. Scattering losses induced by surface deformation due to a hot-spot surface contaminant is found to be most-likely the dominant physics process behind this phenomenon. A good consistency is achieved between the simulation results using the hot-spot model with the experimental data.

In Chapter 6, the full design of the experimental setup of TBOX and the preliminary experiment carried out on it are presented. The goal of the preliminary experiment is realized that is to lock a continuous wave injection laser with the 3.78 m round-trip-length Fabry-Perot cavity using PDH method. Finesse and gain of the preliminary TBOX are measured to be  $\sim 1610$  and 133 respectively. The pathroute for future development of the OEC until final realization of combining OEC with electron storage ring to produce high average flux X-rays is planned. The design of the high power TBOX experimental setup to realize hundreds of kilowatts average power inside and the design of the final OEC which will be combined with electron storage ring of TTX are presented.

### 1.4.2 Innovation Points

1. Provided precise and efficient description of highly focused laser field inside optical enhancement cavity for Thomson scattering simulation with an expression of nonparaxial corrected highly focused linearly polarized laser field derived through a generalized Lax series expansion method.
2. Successfully modeling the modal instabilities appeared on high power optical enhancement cavity and proved the capability of D-shape mirrors for suppressing modal instabilities through simulation. Experimentally realized hour-time-scale stable intra-cavity average power of 200 kW on prototype optical enhancement cavity of ThomX with the implementation of D-shape mirrors.
3. Successfully explaining the fast intra-cavity power drop phenomenon appeared on high-finesse optical enhancement cavity which affects the cavity stability and hinders the intra-cavity power reaching the designed goal. Based on the model attributing this phenomenon to the scattering loss induced by mirror surface thermoelastic deformation due to hot-spot contaminant, experimentally observed power drop behavior could be well reproduced with simulation.

## Chapter 2 Basic Principles of Optical Enhancement Cavity

Optical enhancement cavity (OEC) is Fabry-Perot cavity (FPC) working at the condition that the injection optical wave coherently stacks with the intra-cavity optical wave to realize optical field enhance inside cavity and the steady state is reached when the intra-cavity wave round trip loss of power balance with the injection wave power. In this chapter, the fundamental principles and properties of FPC are introduced to establish a theoretical framework of this thesis. First, the properties of cavity itself are introduced in Section. 2.1, including stability condition, cavity mode and cavity frequency comb. Then cavity enhancements with continuous wave (CW) injection and pulsed wave (PW) injection are analyzed separately in Section. 2.2. Coupling of injection laser beam into the cavity is analyzed from transverse mode matching with telescope and longitudinal phase locking with PDH technique respectively in Section. 2.3.

### 2.1 Properties of Fabry-Perot Cavity

#### 2.1.1 Stability Condition

Modes are electromagnetic fields with certain spatiotemporal distributions which can stably exist inside FPC. The field distributions depend on the properties of FPC and injection optical wave<sup>[66-67]</sup>.

First we represent the geometrical properties of FPC to have mode inside. Generally, FPC consists of  $N$  mirrors with round trip length  $L$ . From a view of geometrical optic and analyzing with ABCD matrix, optical beam can be denoted by two variables:  $r$  the off-axis distance and  $\theta$  the angle between beam and the axis. The process of the beam going through one round trip inside the cavity can be denoted by a transfer matrix  $T$ <sup>[66-67]</sup>. For example for a FPC consists of two reflective mirrors with radius of curvature  $R_1$  and  $R_2$  spaced at a distance of  $L/2$  as shown in Fig. 2.1, the relation of beam  $\begin{bmatrix} r' \\ \theta' \end{bmatrix}$  that has been through one round trip inside cavity with respect to the injection beam of  $\begin{bmatrix} r \\ \theta \end{bmatrix}$  can be written as:

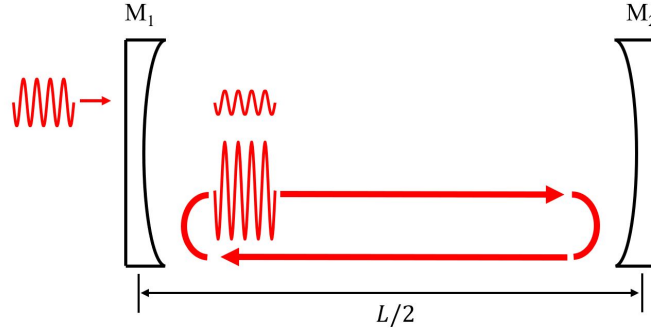


Figure 2.1 Schematic drawing of Fabry-Perot cavity made up of two mirrors.

$$\begin{bmatrix} r' \\ \theta' \end{bmatrix} = T \begin{bmatrix} r \\ \theta \end{bmatrix} = \begin{bmatrix} A & B \\ C & D \end{bmatrix} \begin{bmatrix} r \\ \theta \end{bmatrix} = \begin{bmatrix} 1 & 0 \\ -\frac{2}{R_1} & 1 \end{bmatrix} \begin{bmatrix} 1 & \frac{L}{2} \\ 0 & 1 \end{bmatrix} \begin{bmatrix} 1 & 0 \\ -\frac{2}{R_2} & 1 \end{bmatrix} \begin{bmatrix} 1 & \frac{L}{2} \\ 0 & 1 \end{bmatrix} \begin{bmatrix} r \\ \theta \end{bmatrix}, \quad (2-1)$$

in which

$$\begin{aligned} A &= 1 - \frac{L}{R_2}, \\ B &= L \left(1 - \frac{L}{2R_2}\right), \\ C &= - \left[ \frac{2}{R_1} + \frac{2}{R_2} \left(1 - \frac{L}{R_1}\right) \right], \\ D &= - \left[ \frac{L}{R_1} - \left(1 - \frac{L}{R_1}\right) \left(1 - \frac{L}{R_2}\right) \right]. \end{aligned} \quad (2-2)$$

The transferring matrix is calculated with left-side multiplying, that is the matrix multiplication in Eq. 2-1 is calculated from right to left side. Suppose there could be stable modes exist in this cavity and the eigenvalue  $\beta$  makes the equation  $\begin{bmatrix} A & B \\ C & D \end{bmatrix} \begin{bmatrix} r \\ \theta \end{bmatrix} = \beta \begin{bmatrix} r \\ \theta \end{bmatrix}$  stand, then it demands for  $\det \begin{bmatrix} A - \beta & B \\ C & D - \beta \end{bmatrix} = 0$ , combining the unitarity of the transferring matrix that is  $AD - BC = 1$ , it arrives at the stability condition of the cavity<sup>[67]</sup>:

$$\left[ \frac{1}{2}(A + D) \right]^2 < 1. \quad (2-3)$$

### 2.1.2 Cavity Mode

For the property of the mode, from a view of wave optic, to have stable mode inside FPC, longitudinally the phase delay after one cavity round trip needs to be integer of  $2\pi$ ,

besides the transverse distribution of cavity mode needs to satisfy the integral equation<sup>[66]</sup>:

$$\begin{aligned}\gamma^{(2)} E^{(2)}(s_2) &= \int_{s_1} K^{(1)}(s_2, s_1) E^{(1)}(s_1) ds_1, \\ \gamma^{(1)} E^{(1)}(s_1) &= \int_{s_2} K^{(2)}(s_2, s_1) E^{(2)}(s_2) ds_2, \\ E^{(1)}(s_1) &= E^{(1)}(s_1),\end{aligned}\tag{2-4}$$

in which  $s_1, s_2$  correspondingly represents the transverse coordinates of the surfaces of the two mirrors  $M_1, M_2$ , the integrals are taken over the mirror surfaces,  $\gamma$  describes the field attenuation and phase shift during the passage from one mirror to another,  $K$  the integral kernel depends on the distance from a point on one mirror to a point on another mirror.

Analyzing in Cartesian coordinate and using paraxial-approximation, cavity mode can be expressed by Hermite-Gaussian mode<sup>[66-67]</sup>:

$$\begin{aligned}E_{mn}(x, y, z) &= E_0 H_m \left[ \frac{\sqrt{2}x}{w(z)} \right] H_n \left[ \frac{\sqrt{2}y}{w(z)} \right] \frac{w_0}{w(z)} \exp \left[ -\frac{r^2}{w^2(z)} \right] \\ &\cdot \exp \left[ -ikz - ik \frac{r^2}{2R(z)} + i(1+m+n)\zeta(z) \right],\end{aligned}\tag{2-5}$$

in which  $H_m, H_n$  are the  $m$ -th and  $n$ -th Hermite polynomial, spot size  $w(z) = w_0 \sqrt{1 + (z/z_R)^2}$ , Rayleigh length  $z_R = \pi w_0^2 / \lambda$ , radius of curvature of wavefront  $R(z) = z \left[ 1 + (z_R/z)^2 \right]$ , Gouy phase  $\zeta(z) = \arctan \left( \frac{z}{z_R} \right)$ . Parameter  $q$  is defined as

$$\frac{1}{q(z)} = \frac{1}{R(z)} - i \frac{\lambda}{\pi w^2(z)},\tag{2-6}$$

and follows the transformation rule of

$$q' = \frac{Aq + B}{Cq + D}.\tag{2-7}$$

Especially, the commonly used fundamental mode  $TEM_{00}$  is expressed as

$$E_{00}(x, y, z) = E_0 \frac{w_0}{w(z)} \exp \left[ -\frac{r^2}{w^2(z)} \right] \exp \left[ -ikz - ik \frac{r^2}{2R(z)} + i\zeta(z) \right].\tag{2-8}$$

In the following content, FPC is defaultly considered to be ideally work at  $TEM_{00}$  mode.

### 2.1.3 Cavity Frequency Comb

Define cavity round trip time  $T_c = L/c$ , free spectral range  $FSR = 1/T_c$ , set the  $i$ -th mirror's field reflection and transmission coefficient as  $r_i, t_i$ , whose square modulus

are intensity reflection and transmission coefficient  $T_i$ ,  $R_i$ , and assume for now there's no other loss, that is  $T_i + R_i = 1$ . Define  $\rho = r_1 \cdot r_2 \cdot \dots \cdot r_m$ .

For a monochromatic injection laser wave  $E_L(x, y, z, t) = E_0(x, y, z)e^{i(\omega t - kz)}$  which could be perfectly coupled inside cavity, observing right after injection coupling mirror, the stacked laser field after  $N$  round trip time  $T_c$  can be written as<sup>[68]</sup>:

$$\begin{aligned} E_c^N(x, y, z, t) &= it_1 \left( 1 + \rho e^{-i\omega T_c} + \rho^2 e^{-i2\omega T_c} + \dots + \rho^{N-1} e^{-i(N-1)\omega T_c} \right) E_L(x, y, z, t) \\ &= it_1 \sum_{n=0}^{N-1} (\rho e^{-i\omega T_c})^n E_L(x, y, z, t) \\ &= it_1 \frac{1 - (\rho e^{-i\omega T_c})^N}{1 - \rho e^{-i\omega T_c}} E_L(x, y, z, t). \end{aligned} \quad (2-9)$$

For  $N \rightarrow \infty$ , the steady-state cavity gain with perfectly coupled injection can be written as

$$G_c = \frac{I_c^\infty}{I_{in}} = \frac{|E_c^\infty|^2}{|E_L|^2} = \frac{T_1}{|1 - \rho e^{-i\omega T_c}|^2} = \frac{T_1}{(1 - \rho)^2} \frac{1}{1 + \left( \frac{2\sqrt{\rho}}{1-\rho} \right)^2 \sin^2(\omega T_c/2)}. \quad (2-10)$$

Later on for convenience, the analysis are done with frequency  $\nu$  rather than angular frequency  $\omega$  and they are related as  $\omega = 2\pi\nu$ . The maximums of Eq. 2-10 show at positions  $\sin(\omega T_c/2) = 0$ , where we define  $\nu_c = p/T_c = p\text{FSR}$ , in which  $p$  is positive integer. Besides, linewidth of cavity resonance peak  $\Delta\nu_c$  defined as the full width at half maximum (FWHM) of each resonance peak, and the cavity finesse  $\mathcal{F}$  are as following:

$$\begin{aligned} \Delta\nu_c &= \frac{1}{\pi T_c} \frac{1 - \rho}{\sqrt{\rho}}, \\ \mathcal{F} &= \frac{\text{FSR}}{\Delta\nu_c} = \frac{\pi\sqrt{\rho}}{1 - \rho}. \end{aligned} \quad (2-11)$$

Then Eq. 2-10 can be rewritten in a form of Lorentzian function,

$$G_c(\nu) = \frac{T_1}{(1 - \rho)^2} \frac{(\frac{1}{2}\Delta\nu_c)^2}{(\nu - \nu_c)^2 + (\frac{1}{2}\Delta\nu_c)^2}, \quad (2-12)$$

which we call the cavity resonance frequency comb, as illustratively shown in Fig. 2.2. It is made up of infinite number of resonance peaks each centered at  $\nu = \nu_c$  with FWHM peak width  $\Delta\nu_c$ , spacing at distance of FSR.

Taking an example cavity SBOX with parameters of  $T_1 = 180$  ppm,  $T_2 = T_3 = T_4 = 3$  ppm, FSR= 133.33 MHz, injected with laser of central wavelength  $\lambda = 1 \mu\text{m}$ , then it can be calculated that cavity resonance linewidth  $\Delta\nu_c = 4$  kHz,  $\mathcal{F} = 3.3 \times 10^4$ . It

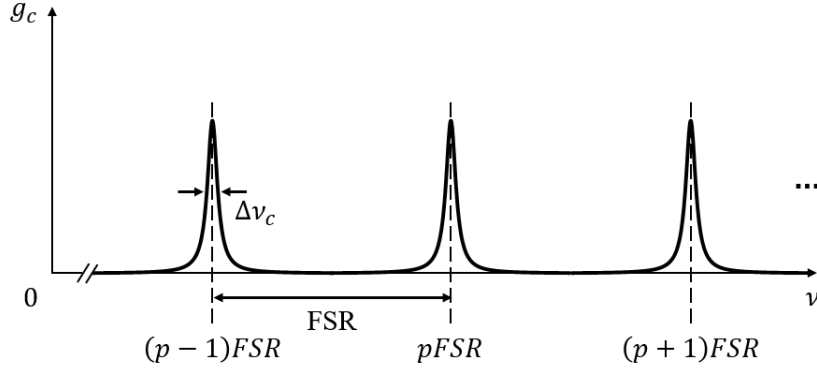


Figure 2.2 Illustrative plot of Fabry-Perot cavity resonance frequency comb.

means that if we control the laser frequency to be resonate with cavity, it demands laser frequency stability to be  $\Delta\nu_c/\nu_L = \Delta\nu_c \cdot \lambda/c < 1.34 \times 10^{-11}$ . From another side, if we control the cavity length thus the injection laser to be resonate with cavity, it demands for the cavity length control precision to be  $\Delta L = L \cdot \Delta\nu_c/\nu_L < 30$  pm. From these characteristic values we can tell the demands of FPC for high precision control system and highly stable environment including low temperature fluctuation and vibration etc.

## 2.2 Enhancement of Fabry-Perot Cavity

For Thomson Scattering experiment, the intra-cavity laser beam will scatter with electron beam to generate X/ $\gamma$ -ray beam. So it's important to know the properties of the intra-cavity laser field, which depend on both the properties of Fabry-Perot cavity and injection laser. In this section, the cavity enhancements of continuous wave (CW) and pulsed wave (PW) injection are analyzed separately.

### 2.2.1 Cavity Enhancement with Continuous Wave Injection

For CW injection, first we analyze in time domain, for a monochromatic CW injection laser  $E_L(x, y, z, t) = E_0(x, y, z)e^{i(2\pi\nu_L t - kz)}$ , following the similar calculation as Eq. 2-9 we can get that at steady state the intra-cavity laser beam intensity can be written as:

$$I_c(t) = |E_c(t)|^2 = \frac{T_1}{(1-\rho)^2} \frac{I_0}{1 + \left(\frac{2\sqrt{\rho}}{1-\rho}\right)^2 \sin^2(\pi\nu_L T_c)}, \quad (2-13)$$

in which  $I_0(x, y, z) = |E_0(x, y, z)|^2$ .

Then we analyze in frequency domain, for general case of injection laser wave with

a frequency comb  $\hat{I}_L(\nu)$ , which is technically the spectrum of the injection laser, that is

$$\hat{I}_L(\nu) = \left| \int_{-\infty}^{+\infty} E_L(x, y, z, t) e^{-i2\pi\nu t} dt \right|^2, \quad (2-14)$$

Intra-cavity field intensity can be expressed in frequency domain as

$$\hat{I}_c(\nu) = G_c(\nu) \cdot \hat{I}_L(\nu). \quad (2-15)$$

For monochromatic CW injection  $\hat{I}_L(\nu) = I_0\delta(\nu - \nu_L)$ , then the intra-cavity field intensity in frequency domain is

$$\hat{I}_c(\nu) = I_0 G_c(\nu) \delta(\nu - \nu_L), \quad (2-16)$$

which is consistent with time domain analysis since  $\hat{I}(\nu)_c = FT\{I_c(t)\}$ , in which  $FT$  stands for Fourier transform.

More generally for CW laser injection,  $\hat{I}_L(\nu)$  is a single peak centered at the laser central frequency  $\nu_L$  with a FWHM peak width  $\Delta\nu_L$ , commonly called linewidth of laser. For example for a non-monochromatic injection CW laser with a Lorentzian shaped spectrum expressed as  $\hat{I}_L(\nu) = \frac{I_0}{\pi} \frac{\frac{1}{2}\Delta\nu_L}{(\nu - \nu_L)^2 + (\frac{1}{2}\Delta\nu_L)^2}$ , with central wavelength  $\lambda = 1030$  nm, linewidth  $\Delta\nu_L = 3$  kHz, being injected to the example cavity SBOX, graphically the intra-cavity field spectrum, as shown in Fig. 2.3, is the product of cavity frequency comb with laser frequency comb.

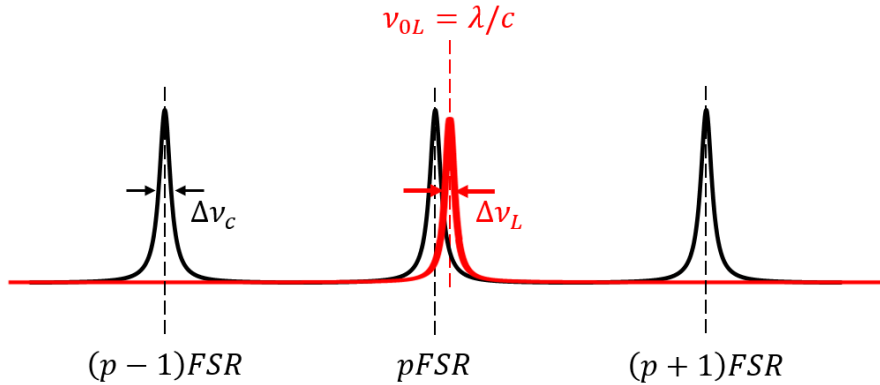


Figure 2.3 Illustrative plot of cavity frequency comb (black) with continuous wave laser frequency comb (red), the intra-cavity field spectrum is mathematically the product of the two.

### 2.2.2 Cavity Enhancement with Pulsed Wave Injection

For pulsed wave, a monochromatic pulsed wave is impossible to exist as a result of the finite pulse length complying with uncertainty principle, but a time domain analysis of cavity gain with injection of pulsed wave taking a single frequency part will lead to useful result for understanding the dynamic process of cavity filling. So, in time domain, taking a single frequency part of the pulsed wave laser field written as  $E_L(x, y, z, t) = E_0(x, y, z) \sum_{m=-\infty}^{m=+\infty} e(t - mT_L) e^{i[(2\pi\nu_L t - mT_L) + m\Delta\Phi_{ce} + kz]}$ , in which  $e(t)$  is the pulse envelope,  $\Phi_{ce}$  is the carrier-envelope phase, each pulse is in the form of  $E_m(x, y, z, t) = E_0(x, y, z) e(t - mT_L) e^{i[(2\pi\nu_L t - mT_L) + m\Delta\Phi_{ce} + kz]}$ . Observe at the cavity inner side of injection coupling mirror, the stacked laser field after  $N$  round trip time  $T_c$  can be written as<sup>[31,34]</sup>

$$E_c^N(x, y, z, t) = it_1 \sum_{n=0}^{N-1} r^{n-1} E_{N-n-1}(t - nT_c), \quad (2-17)$$

here it is implicitly assumed that the laser pulse period  $T_L$  ideally to be matched with single cavity round trip time  $T_c$ , the difference between those two is  $\Delta T = T_c - T_L$ , and define  $\Phi_D = \omega_0 \Delta T + \Delta\Phi_{CE}$ . The cavity gain of intensity with pulsed wave injection can be written as<sup>[31,34]</sup>

$$I_c^N = \frac{T_1}{1 - r^2} \left[ (1 - r^{2N}) A(0) + 2 \sum_{n=1}^{N-1} (r^n - r^{2N-n}) \cos(n\Phi_D) A(n\Delta T) \right], \quad (2-18)$$

in which  $A(t) = \int_{-\infty}^{+\infty} |\hat{e}(\nu)|^2 e^{i2\pi\nu t} d\nu$ ,  $\hat{e}(\nu) = \int_{-\infty}^{+\infty} e(t) e^{i2\pi\nu t} dt$ . For the case of  $\Delta T = 0$ ,  $\Delta\Phi_{ce} = 0$ ,

$$I_c^N = I_0 T_1 \left( \frac{1 - \rho^N}{1 - \rho} \right)^2. \quad (2-19)$$

Taking example cavity SBOX, the curve of normalized intra-cavity field intensity  $I_c^N / I_c^\infty$  versus time is shown in Fig. 2.4, of which it takes  $\sim 500 \mu s$  to reach steady state.

From a view of frequency domain, the frequency comb of the single frequency part of PW laser is  $\hat{I}_L(\nu) = I_0 |\hat{e}(\nu - \nu_L)|^2 \sum_{m=-\infty}^{m=+\infty} \delta\left(\frac{\Delta\Phi_{ce}}{2\pi} - \nu_L T_L - m\right)$ , which is multiple peaks each centered at position of  $\nu_L = (\Delta\Phi_{ce} - m) f_L$  with infinite narrow width and amplitude modulated by envelope  $|\hat{e}(\nu - \nu_L)|^2$ , in which  $f_L = 1/T_L$  is the laser pulse repetition rate. Then applying Eq. 2-15 the intra-cavity field intensity in frequency domain is<sup>[31,34]</sup>

$$\hat{I}_c(\nu) = I_0 G_c(\nu) |\hat{e}(\nu - \nu_L)|^2 \sum_{m=-\infty}^{m=+\infty} \delta\left(\frac{\Delta\Phi_{ce}}{2\pi} - \nu_L T_L - m\right), \quad (2-20)$$

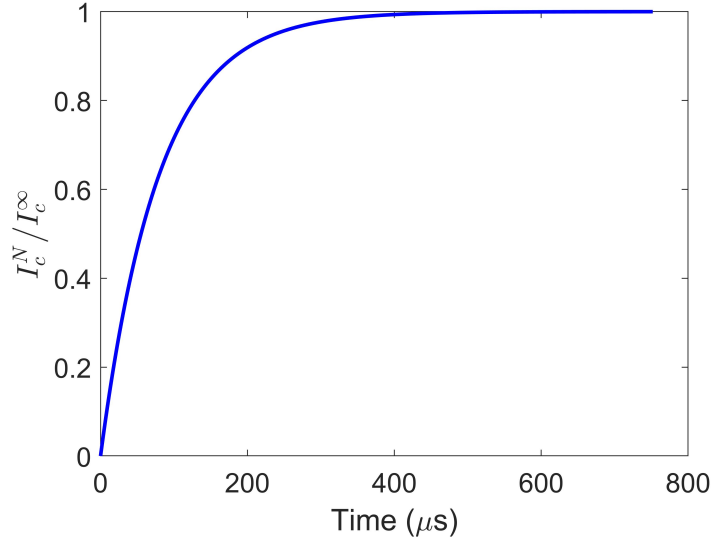


Figure 2.4 Normalized cavity gain versus time of example cavity SBOX with perfectly coupled pulsed wave injection laser.

which is consistent with time domain analysis since  $\hat{I}_c(\nu) = FT\{I_c(t)\}$ .

More generally for PW laser injection, each peak of the spectrum should be with finite linewidth  $\Delta\nu_L$ . For example for PW injection laser with Lorentzian shaped teeth of comb expressed as  $\hat{I}_L(\nu) = \frac{|\hat{e}(\nu)|^2}{\pi} \frac{\frac{1}{2}\Delta\nu_L}{(\nu-\nu_L)^2 + (\frac{1}{2}\Delta\nu_L)^2}$ , with central wavelength  $\lambda = 1030$  nm, linewidth  $\Delta\nu_L = 3$  kHz, repetition rate  $f_L = 133.33$  MHz, being injected into the example cavity SBOX, graphically the intra-cavity field spectrum, as illustratively shown in Fig. 2.5, is the product of cavity frequency comb with laser frequency comb.

## 2.3 Coupling of Injection Laser into Fabry-Perot Cavity

In this section, methods of coupling injection laser to external Fabry-Perot cavity are analyzed transversely and longitudinally.

### 2.3.1 Transverse Mode Matching with Telescope

Transversely, from a view of geometrical optic, the injection laser beam size and angle should match with that of the cavity mode at the position of injection coupling mirror, which can be achieved by telescope composed of one to multiple lenses and can be designed with calculation of ABCD matrix. In experiment, the beam size  $w_0$  and divergence angle  $\theta_0$  of the output of laser can be measured at position  $z_0$ , then the injection laser beam size  $r_{in}$  and angle  $\theta_{in}$  can be calculated with the transferring matrix  $T_t$  of the

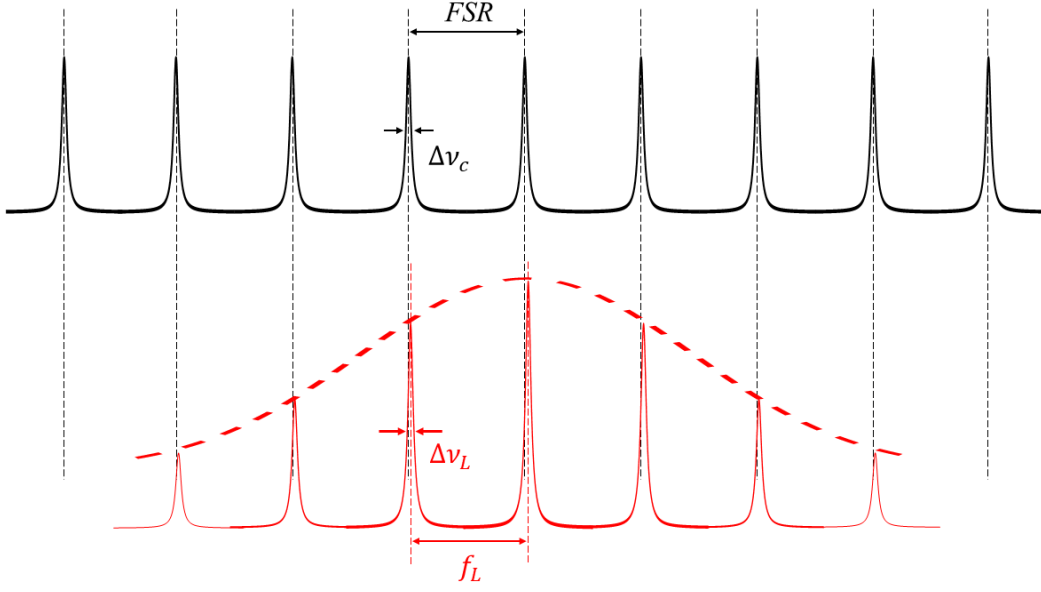


Figure 2.5 Illustrative plot of cavity frequency comb (black) with pulsed wave laser frequency comb (red), the intra-cavity field spectrum is mathematically the product of the two.

optical path from position  $z_0$  to injection coupling mirror position  $z_{M_1}$  as

$$\begin{bmatrix} r_{in} \\ \theta_{in} \end{bmatrix} = T_t \begin{bmatrix} r_0 \\ \theta_0 \end{bmatrix}. \quad (2-21)$$

The design of telescope can be achieved by optimization of the difference between  $\begin{bmatrix} r_{in} \\ \theta_{in} \end{bmatrix}$  and  $\begin{bmatrix} r_c \\ \theta_c \end{bmatrix}$ , where variables with subscript "c" represent the quantities of the cavity mode which can be calculated with ABCD matrix depending on cavity structure.

From a view of wave optic, telescope design can also be done with calculation of ABCD matrix, but using Gaussian laser beam and following the rule of  $q$  parameter changing with transferring ABCD matrix as expressed in Eq. 2-7. The field of output of laser  $E_L(x, y, z)$  at position  $z_0$  can be expressed as Eq. 2-8, of which the corresponding parameters can be measured experimentally. The injection laser field  $E_{in}(x, y, z)$  at injection coupling mirror position  $z_{M_1}$  can be calculated following the rule of  $q$  parameter of  $E_L(x, y, z)$  changing with transferring matrix. Field of cavity mode  $E_c(x, y, z)|_{z=z_{M_1}}$  can be calculated according to cavity structure. Then telescope design can be achieved by optimization of coupling which is expressed as<sup>[31]</sup>

$$C = \frac{\int \int_{-\infty}^{+\infty} |E_{in}(x, y, z) E_c^*(x, y, z)|^2 dx dy}{\int \int_{-\infty}^{+\infty} |E_{in}(x, y, z)|^2 dx dy \int \int_{-\infty}^{+\infty} |E_c(x, y, z)|^2 dx dy} \Big|_{z=z_{M_1}}. \quad (2-22)$$

For cavity with asymmetric transferring matrix on tangential and sagittal axes, the

cavity mode sizes are asymmetric. And the asymmetry will evolve with the mirror surface thermoelastic deformation alongside the increasing intra-cavity power. So to do mode matching for asymmetry cavity mode, more elaborate design of telescope should be implemented which could tune mode size on tangential and sagittal axes independently.

### 2.3.2 Longitudinal Phase Locking with PDH Technique

A high precision feedback is needed to keep the injection laser being resonated with the external Fabry-Perot cavity. The most commonly used feedback method is Pound-Drever-Hall (PDH)<sup>[62-63]</sup> technique. If it is the optical frequency of injection laser to be tuned to resonate with the Fabry-Perot Cavity, then the key is to find an error signal that can tell which side of the injection laser central frequency deviates from the central resonance frequency. A control signal will be generated after process of the error signal to tune the optical frequency of the injection laser. Fig. 2.6 shows the basic layout of locking a laser to external Fabry-Perot cavity using PDH technique.

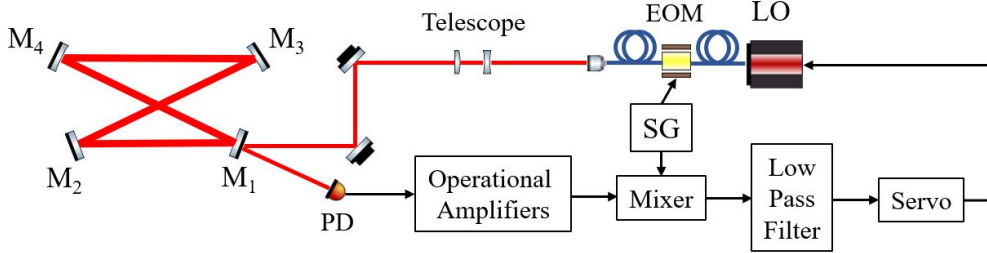


Figure 2.6 The basic layout of locking a laser to external Fabry-Perot cavity using PDH technique. LO: laser oscillator. EOM: electro-optic modulator. PD: photodiode. SG: signal generator.

An error signal containing information both about the cavity and injection laser beam should be taken at the position of the reflection of injection coupling mirror  $M_1$  by photodiode as shown in Fig. 2.6. The steady state cavity reflection function can be written as

$$F(\omega) = \frac{E_r^\infty}{E_L} = r_1 - \frac{\rho}{r_1} \frac{T_1 e^{-i\omega T_c}}{1 - \rho e^{-i\omega T_c}} \quad (2-23)$$

For a monochromatic CW injection laser  $E_L = E_0 e^{i\omega t}$ , a sine wave with frequency of  $\Omega$  and amplitude of  $\beta$  is generated by signal generator and applied to electro-optic modulator (EOM) to produce a phase modulation on the injection laser wave. The laser

beam after EOM modulation can be expressed as  $E'_L = E_0 e^{i(\omega t + \beta \sin(\Omega t))}$ . Generally, using the Jacobi-Anger expansion relation  $e^{iz \sin \theta} = \sum_{n=-\infty}^{+\infty} J_n(z) e^{in\theta}$  and the Bessel function property  $J_{-n}(z) = (-1)^n J_n(z)$ , the sine wave phase modulation can be rewritten as sum of infinite number of sidebands with frequency of  $(\omega \pm n\Omega)$ , in which  $n$  is positive integer.

$$E'_L = E_0 J_0(\beta) e^{i\omega_L t} + \begin{cases} \sum_{n=1}^{\infty} E_0 J_n(\beta) [e^{i(\omega_L + n\Omega)t} - e^{i(\omega_L - n\Omega)t}], & n \text{ odd}; \\ \sum_{n=2}^{\infty} E_0 J_n(\beta) [e^{i(\omega_L + n\Omega)t} + e^{i(\omega_L - n\Omega)t}], & n \text{ even}. \end{cases} \quad (2-24)$$

Here the modulation depth is set as  $\beta \ll 1$ , such that the power being shifted from the central optical frequency of the injection laser can be neglected. So a first order expansion would be enough. The CW laser field after EOM modulation can be written as

$$E'_L = E_0 (e^{i\omega t} + J_1(\beta) e^{i(\omega + \Omega)t} - J_1(\beta) e^{-i(\omega - \Omega)t}). \quad (2-25)$$

The resulted cavity reflection field is

$$E'_r = E_0 [F(\omega) e^{i\omega t} + J_1(\beta) F(\omega + \Omega) e^{i(\omega + \Omega)t} - J_1(\beta) F(\omega - \Omega) e^{i(\omega - \Omega)t}]. \quad (2-26)$$

And the intensity measured by photodiode at the reflection position of  $M_1$  is

$$\begin{aligned} P_r &= |E'_r|^2 \\ &= 2J_1(\beta) \text{Re} [F(\omega) F^*(\omega + \Omega) - F^*(\omega) F(\omega - \Omega)] \cos(\Omega t) \\ &\quad + 2J_1(\beta) \text{Im} [F(\omega) F^*(\omega + \Omega) - F^*(\omega) F(\omega - \Omega)] \sin(\Omega t) \\ &\quad + (\text{const terms}) + (2\omega \text{ terms}). \end{aligned} \quad (2-27)$$

The single  $\Omega$  component in the cavity reflection signal as a result of interference between the sideband signal with the cavity reflected central frequency signal will provide information of the cavity central resonance frequency thus will provide error signal used for PDH feedback. In practice, the modulation frequency  $\Omega$  is far off the resonance linewidth of cavity, where we have  $F(\omega \pm \Omega) = -1$ . Then the coefficient of *cosine* term vanishes. The error signal can be demodulated out by mixer with a  $\sin(\Omega t)$  signal with proper phase as

$$\epsilon = 2J_1(\beta) \text{Im} [F(\omega) F^*(\omega + \Omega) - F^*(\omega) F(\omega - \Omega)]. \quad (2-28)$$

For example, error signal of laser with frequency  $\nu$  modulated by  $\Omega = 8.2$  MHz injected into example cavity SBOX is shown in Fig. 2.7 and Fig. 2.8.

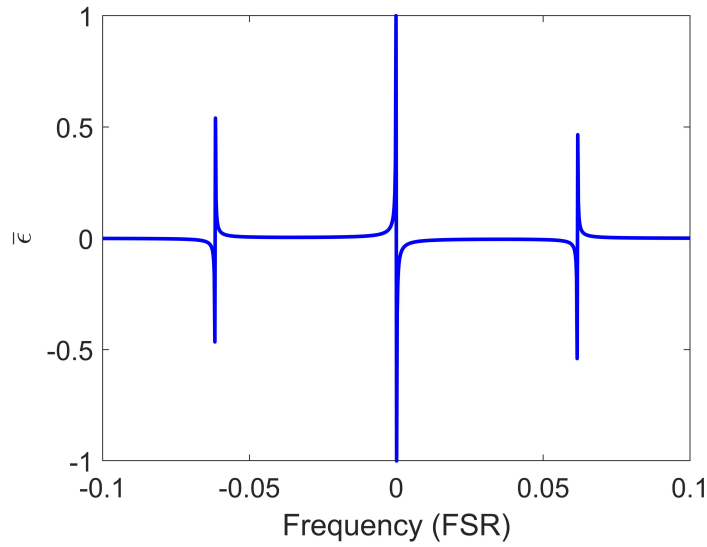


Figure 2.7 Normalized error signal of laser with frequency  $\nu$  modulated by  $\Omega = 8.2$  MHz injected into example cavity SBOX. Normalization is made by dividing the maximum.

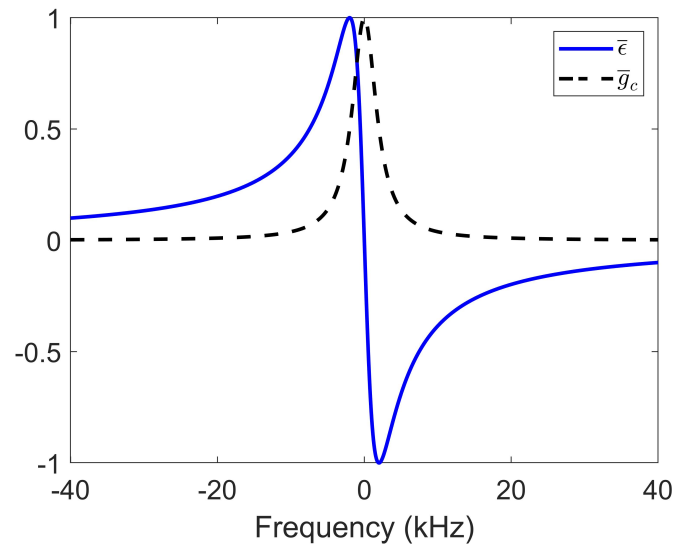


Figure 2.8 Zoom of the normalized error signal (blue) shown in Fig. 2.7 of laser with frequency  $\nu$  modulated by  $\Omega = 8.2$  MHz injected into example cavity SBOX, overlapped with cavity frequency comb (black). Both curves are normalized by dividing their maximums respectively.

## Chapter 3 Nonparaxial Expression of Highly Focused Laser Field

In Thomson scattering experiments, a highly focused laser beam with waist radius of few tens of micrometers is needed to match the transverse size of the electron beam to increase the yield of the scattered photon as much as possible. Highly focused laser field couldn't be precisely described by a paraxial approximated expression. Here in this section presented an expression of the highly focused linearly polarized laser field derived through a generalized Lax expansion series method<sup>[69]</sup>.

Several approaches have been used in the past to model the laser beam in the focusing region, each corresponding to different assumptions. Closed form solutions satisfying exactly Maxwell equations were obtained for radially polarized laser beams provide self-consistent expressions that however correspond to definite boundary conditions that may not be representative of an actual experiment<sup>[70]</sup>. Alternatively, Maxwell equations consistent integral expressions are also available but suffer from approximations and are also bound to specific boundary conditions<sup>[71]</sup>. Finally, the historical technique consisting in expanding paraxial solutions of the wave equations in series<sup>[72]</sup> has been recently shown to offer the unique ability to account for arbitrary boundary conditions<sup>[73]</sup>. This ability may be seen as crucial when considering the sensitivity of the scattering process to boundary conditions that is likely to limit the predictive power of detailed and expansive simulations.

Though the vectorial approach is elegant and provide self-consistent solutions to the Maxwell equations, but still suffers from some approximations, the resulting integral expressions require large computational time, especially when precision is required, which may not be practical in many cases. Also they are usually bound to give boundary conditions that may not be relevant to a specific experimental situation<sup>[73]</sup>. The sensitivity to these may thus not be easy to gauge, being a critical aspect for experimental demonstration. An alternative approach consist in a generalized series expansion<sup>[73]</sup> which is self-consistent only at a given order of the series expansion (this may not be of numerical importance) but allows to assert the sensitivity to a choice of boundary conditions (i.e. non-predictive aspects of a specific experiment thus giving a clue for tolerance studies) and analytic direct-space expressions, that are computationally efficient. As mentioned

in Ref.<sup>[71]</sup>, this approach entails far-field divergences<sup>[74]</sup> that are sometimes of importance in the phase space of interest for the studied problem, though this problem can be solved<sup>[75]</sup>.

It is sometimes thought that vectorial models cannot be represented by means of series expansions<sup>[71]</sup> whereas providing more accurate expressions of the fields. In the following part of this chapter this statement will be rebutted. As an example, a generalized perturbation expansion method is applied to linearly polarized laser beam and compared with the Ignatovsky solution<sup>[76]</sup> revisited in Ref.<sup>[71]</sup>. The formalism of the former (latter) is presented in Section 3.1 (3.2). Coefficients of the series expansion are fit to the expressions of Ignatovsky in Section 3.3 and field distribution compared between that from the generalized Lax series expansion method and that from the Ignatovsky formalism.

### 3.1 Series Expansion Formalism

Linearly polarized electromagnetic field expressions beyond paraxial approximation can be obtained by means of series expansion<sup>[72]</sup> with the prescription of Davis<sup>[77]</sup>. Though a careful explicit symmetrization of the result is required<sup>[78]</sup> which is naturally embedded in the Hertz potentials  $\vec{\Pi}_e, \vec{\Pi}_m$ <sup>[70,79]</sup>. The electromagnetic fields read

$$\begin{aligned}\vec{E} &= \vec{\nabla} \times \vec{\nabla} \times \vec{\Pi}_e - \mu_0 \frac{\partial}{\partial t} \vec{\nabla} \times \vec{\Pi}_m \\ \vec{B} &= \mu_0 \vec{\nabla} \times \vec{\nabla} \times \vec{\Pi}_m + \frac{1}{c^2} \frac{\partial}{\partial t} \vec{\nabla} \times \vec{\Pi}_e,\end{aligned}\tag{3-1}$$

in which, for a linearly polarized wave focused along  $z$  axis and polarized along  $x$  axis,  $\vec{\Pi}_e = \hat{a}_x \Psi(x, y, z, t)$ ,  $\vec{\Pi}_m = \hat{a}_y \eta_0^{-1} \Psi(x, y, z, t)$ , where  $\hat{a}_{x,y,z}$  are unit vectors in the directions  $x, y, z$  of the reference frame. It is explicit in these expressions that a single scalar function  $\Psi(x, y, z, t)$  is required to describe the focused field. Scalar and vector potentials are then related to the Hertz potentials by  $V \equiv -\vec{\nabla} \cdot \vec{\Pi}_e$  and  $\vec{A} \equiv (1/c^2) \partial \vec{\Pi}_e / \partial t + \mu_0 \vec{\nabla} \times \vec{\Pi}_m$ , since  $\vec{B} \equiv \vec{\nabla} \times \vec{A}$  and  $\vec{E} \equiv -\vec{\nabla} V - \partial \vec{A} / \partial t$  in the Lorenz gauge.

It is thus possible to expand perturbatively the scalar function  $\Psi(x, y, z, t)$  in series to derive field expressions beyond the paraxial approximation, but it is rather usually performed with the scalar function  $\mathcal{A}(x, y, z, t)$  that defines the vector potential  $\vec{A}'(x, y, z, t) = \hat{a}_x \mathcal{A}(x, y, z, t)$  and its symmetric counterpart  $\vec{A}''(x, y, z, t) = \hat{a}_y \mathcal{A}(x, y, z, t)$ , that allows to rewrite the electromagnetic fields  $\vec{E} = \vec{E}' + \vec{E}''$  and  $\vec{B} = \vec{B}' + \vec{B}''$  where  $\vec{B}' = \vec{\nabla} \times \vec{A}'$  and  $\vec{E}'' = \vec{\nabla} \times \vec{A}''$ . The  $\vec{E}'$  and  $\vec{B}''$  are consistently defined by the Maxwell equations. Both approaches provide equivalent fields at first order in the expansion series. The expansion

could also be performed on the six fields projections themselves<sup>[80]</sup>, which provides another equivalent procedure at first order in the expansion. In the following, we choose to follow the customary procedure that consists in expanding the scalar function  $\mathcal{A}(x, y, z, t)$  by writing it in the form

$$\mathcal{A}(x, y, z, t) = \mathcal{A}_0 g(\phi/\phi_0) e^{i(\phi - \delta\phi)} \psi(x, y, z), \quad (3-2)$$

where  $g(\phi/\phi_0)$  is the envelope of the pulse,  $\delta\phi$  the carrier to envelope phase shift,  $\phi = kz - \omega_0 t$ ,  $\phi_0 = \omega_0 \tau / g^{-1}(\exp(-1))$ ,  $\tau$  is the single-sided  $\exp(-1)$  pulse width and  $\psi(x, y, z)$  is the spatial profile. The scalar wave equation  $\nabla^2 \mathcal{A} - \frac{1}{c^2} \frac{\partial^2}{\partial t^2} \mathcal{A} = 0$  simplifies under slowly varying envelope approximation,  $\left| \frac{1}{g(\phi/\phi_0)} \frac{\partial g(\phi/\phi_0)}{\partial \phi} \right| \ll 1$ , into a scalar equation for the spatial envelope  $\nabla^2 \psi + 2ik \frac{\partial \psi}{\partial z} = 0$ . Employing dimensionless coordinates,  $\vec{\rho} = (\xi, \eta) = (x, y)/w_0$  and  $\zeta = z/z_R$ , it reads  $\nabla_{\perp}^2 \psi + \varepsilon^2 \frac{\partial^2}{\partial \zeta^2} \psi + 4i \frac{\partial \psi}{\partial \zeta} = 0$ , where  $\varepsilon = w_0/z_R$  and  $\nabla_{\perp}^2 = \frac{\partial^2}{\partial \xi^2} + \frac{\partial^2}{\partial \eta^2}$ , with  $w_0$  the waist of the laser beam and  $z_R$  its Rayleigh length. The solution of this equation can be obtained by means of a perturbation method<sup>[72]</sup> when  $\varepsilon$  is sufficiently small. It reads

$$\psi = \sum_{n=0}^{\infty} \varepsilon^{2n} \psi_{2n}. \quad (3-3)$$

Successive orders  $\psi_{n \geq 1}$  are solved from the recursive equations by equalizing the terms with the same order of  $\varepsilon^2$

$$(\nabla_{\perp}^2 + 4i \frac{\partial}{\partial \zeta}) \psi_{2n} = \begin{cases} 0, & \text{if } n = 0 \\ -\frac{\partial^2 \psi_{2(n-1)}}{\partial \zeta^2}, & \text{if } n > 0. \end{cases} \quad (3-4)$$

The  $n = 0$  paraxial solution is  $\psi_0 = f \exp(-f \rho^2)$  where  $f = 1/(1 + i\zeta)$ . Solutions of the higher order can be obtained by solving recursively in momentum space the Eq. 3-4, that translates into

$$(-\kappa_{\xi}^2 - \kappa_{\eta}^2 + 4i \frac{\partial}{\partial \zeta}) \tilde{\psi}_{2n} = \begin{cases} 0, & \text{if } n = 0 \\ -\frac{\partial^2 \tilde{\psi}_{2(n-1)}}{\partial \zeta^2}, & \text{if } n > 0, \end{cases} \quad (3-5)$$

where  $\tilde{\psi}$  is the Fourier transform of  $\psi$  and  $\kappa_{\xi, \eta}$  are the transverse momenta corresponding to  $\xi, \eta$ . The paraxial solution of this equation is  $\tilde{\psi}_0 = \exp(-(\kappa_{\xi}^2 + \kappa_{\eta}^2)/(4f))$ . Solutions of these equations can be obtained as  $\tilde{\psi}_{2n} = \tilde{\psi}_0(Q_n + P_n)$  where  $P_n$  is a polynomial in  $\zeta$  and  $\kappa_{\xi}^2 + \kappa_{\eta}^2$  determined by the equation  $\tilde{\psi}_0 P_n = -\frac{\partial^2 \tilde{\psi}_{2(n-1)}}{\partial \zeta^2}$  and  $Q_n = \sum_{j=1}^{n+1-k} \sum_{k=1}^{n+1} C_{2n, j, k} \kappa_{\xi}^{2(j-1)} \kappa_{\eta}^{2(k-1)}$ . It is chosen not to include higher powers of  $\kappa_{\xi, \eta}^2$  since they are naturally accounted for by higher order terms of the expansion. The coefficients

corresponding to the lower powers of  $\kappa_{\xi,\eta}^2$  in principle can be set to zero since they correspond to a redefinition of the scaling of the field or of the expansion parameter  $\varepsilon$ . Though we will see they are useful in some cases. In the direct space, the solutions in case of a symmetric  $x \leftrightarrow y$  solution of the paraxial expansion of the scalar  $\psi$  function can be found in Ref.<sup>[73]</sup>. It can be useful to consider a more general version where this symmetry is explicitly broken, but yet no general astigmatism is introduced<sup>[81]</sup>. The first term in the expansion reads

$$\begin{aligned} \psi_2(\xi, \eta, f) = & f \left( -\frac{1}{2} + 2C_{2,1,2} + 2C_{2,2,1} \right) \\ & + f^2 \left( \frac{1}{2} + \rho^2 - 4(\xi^2 C_{2,1,2} + \eta^2 C_{2,2,1}) + 4C_{2,2,2} + 12(C_{2,1,3} + C_{2,3,1}) \right) \\ & + f^3 \left( -\frac{\rho^4}{4} - \rho^2(1 + 8C_{2,2,2}) - 48(\xi^2 C_{2,1,3} + \eta^2 C_{2,3,1}) \right) \\ & + f^4 \left( \frac{\rho^4}{4} + 16(\xi^4 C_{2,1,3} + \eta^4 C_{2,3,1}) + 16\xi^2 \eta^2 C_{2,2,2} \right). \end{aligned} \quad (3-6)$$

These expression match those previously obtained in Ref.<sup>[73]</sup>, where the  $x \leftrightarrow y$  symmetry is enforced i.e. when  $C_{2,1,2} = C_{2,2,1} = \tilde{C}_{2,2}$  and  $C_{2,1,3} = C_{2,3,1} = C_{2,2,2}/2 = \tilde{C}_{2,4}$ , where the tilde coefficients are those of the Ref.<sup>[73]</sup>. Higher orders are straightforwardly calculated by means of a symbolic computation software, whose results are piped into a numerical computation software. Obtained expression for the order 2 are too long to be reproduced here but they are similar to those of Ref.<sup>[73]</sup> with the  $x \leftrightarrow y$  relaxed. It is then plugged into Eq. 3-3, further used in Eq. 3-2 and to compute the vectors  $\vec{A}'$  and  $\vec{A}''$ . These  $C$  parameters were found to allow matching known solutions of the scalar wave equation expanded up to the second term of the expansion, corresponding to various boundary conditions<sup>[73]</sup>. They in general depend on the injecting laser beam and the boundary conditions imposed by the optical system and are in principle complex numbers. Indeed nothing bounds them to the real space in the derivation previously described. They can, in principle, be obtained by means of a fit to a given numerical description of the electromagnetic field numerically derived or experimentally measured, up to a certain precision. The procedure that is described here is strictly valid for monochromatic pulses only, which is sufficient in the case studied in this article, though it can be extended to generally astigmatic beams<sup>[81]</sup> and electromagnetic fields involving spatiotemporal couplings<sup>[82]</sup>. Extreme cases where a very broad angular spectrum as those considered for instance in Ref.<sup>[83]</sup> are unlikely described by such series expansion, owing to large values of the expansion parameter  $\varepsilon$ .

### 3.2 Ignatovsky Formalism

The Ignatovsky solution<sup>[71]</sup> is derived from a collimated linearly polarized Gaussian beam  $\vec{E}_i(x, y, z) = e(t)e^{i(kz-\omega_0t)}\hat{x}$ , where  $w_i$  is the radius of the beam and  $e(t) = E_0e^{-(x^2+y^2)/w_i^2}$ , focused by a perfect and perfectly aligned parabolic mirror with focal length  $f$  whose surface is denoted as  $z' = -f + (x'^2 + y'^2)/(4f)$ , in which  $(x', y', z')$  are specialized to represent the points on the parabolic mirror surface. Several approximations are made in the derivation. First of all the Debye approximation is employed, the focusing mirror residing far from the focus, and the transverse electromagnetic field envelope is supposed to vary slowly laterally on the mirror surface. The reflected fields<sup>[71]</sup> are expressed as

$$\begin{aligned}\vec{E}(x, y, z) &= -ikf e^{i(kf-\omega_0t)} \left[ \hat{x} \left( I_0 + \frac{x^2 - y^2}{r^2} I_2 \right) + \hat{y} \frac{2xy}{r^2} I_2 - i\hat{z} \frac{x}{r} I_1 \right], \\ \vec{B}(x, y, z) &= -i \frac{kf}{c} e^{i(kf-\omega_0t)} \left[ \hat{x} \frac{2xy}{r^2} I_2 + \hat{y} \left( I_0 - \frac{x^2 - y^2}{r^2} I_2 \right) - i\hat{z} \frac{y}{r} I_1 \right],\end{aligned}\quad (3-7)$$

in which

$$\begin{aligned}I_0 &= \int_0^\pi d\theta e(t)(r') J_0(kr \sin \theta) \sin \theta e^{ikz \cos \theta}, \\ I_1 &= 2 \int_0^\pi d\theta e(t)(r') \sqrt{\eta(\theta)} J_1(kr \sin \theta) \sin \theta e^{ikz \cos \theta}, \\ I_2 &= \int_0^\pi d\theta e(t)(r') \eta(\theta) J_2(kr \sin \theta) \sin \theta e^{ikz \cos \theta},\end{aligned}\quad (3-8)$$

where  $x = r \cos \phi$ ,  $y = r \sin \phi$  and  $\eta(\theta) = (1 - \cos \theta)/(1 + \cos \theta)$ .

This integral solution of the Maxwell equations may sound elegant since it provides expressions based on assumptions that are easier to gauge compared to the expression of the field at the focus point, as done in the series expansion method. If it may appear easier to accept that the input beam envelope can be approximated by a pure paraxial Gaussian beam, it may be more difficult to accept that the key focusing element of a corresponding experimental setup may be a perfect surface, aberration free, and perfectly aligned, which would break the symmetry. This renders the practical utility of such an approach difficult to gauge. These integral formulae have been compared against few existing series expansions without much success<sup>[71]</sup>, since they are corresponding to different boundary conditions. However, using a generalized approach as that described in section 2, may

allow to approximate with enough precision these integral formulae and at the same time allowing for gauging effects as misalignments by rotating space coordinates and reducing significantly the computer calculation time.

### 3.3 Approximating the Ignatovsky Formulae with the Series Expansion

As already mentioned, nothing forbids to extract the arbitrary coefficients of the series expansion by a fit on numerical expressions that are obtained, for instance, by a theoretical integral model. We illustrate this possibility in this section by fitting the first order, except otherwise explicitly stated, expansion coefficients to the numerical field values obtained with Ignatovsky's expressions.

The field amplitude is set to be  $E_0 = 1$  that is an unnecessary scale factor for the extraction of the free coefficients. We also use  $\lambda = 1 \mu\text{m}$ ,  $w_i = 0.1 \text{ m}$ ,  $f = 2w_i$ . For the fitting process the expressions from Ignatovsky are scaled by the value of the electric field along the  $x$  direction at the ideal focus point parameterized by  $x = 0, y = 0, z = 0$ . In order to allow for a slight mismatch in the total field energy, a scale coefficient is introduced in front of terms independent of the previously introduced  $C$  coefficients.  $N_c = 7$  coefficients are thus obtained by matrix inversion since the obtained field expressions are linearly dependent on those. The contribution of each of the six projections of the real parts of the electromagnetic field to each term proportional to a given coefficient is filled in a  $6N_s \times N_c$  matrix denoted  $M$ . The  $6N_s$  real field projections at the  $N_s$  sampling points for the expression of Ignatovsky is stored in a vector  $F$ . The best fit coefficients are thus obtained by

$$C_f = (M^T \cdot M)^{-1} \cdot M^T \cdot F, \quad (3-9)$$

where the superscript  $T$  denotes the transposition operator. The quality of the fit is gauged by a parameter

$$\chi^2 = \sum_{N_s} |F - M \cdot C_f|^2. \quad (3-10)$$

The waist  $w_0$  of the Gaussian beam used for the series expansion is fixed in this procedure, that is thus repeated for various  $w_0$  values that are scanned in an appropriate range. The  $\chi^2$  dependence on the  $w_0$  value, shown on Fig. 3.1, is approximately parabolic with a minimum value in the range of interest, thus uniquely defining the best fitting set

of coefficients  $C_b$  associated to a value of  $w_{0,b}$  that provide the best approximation of the integral expressions.

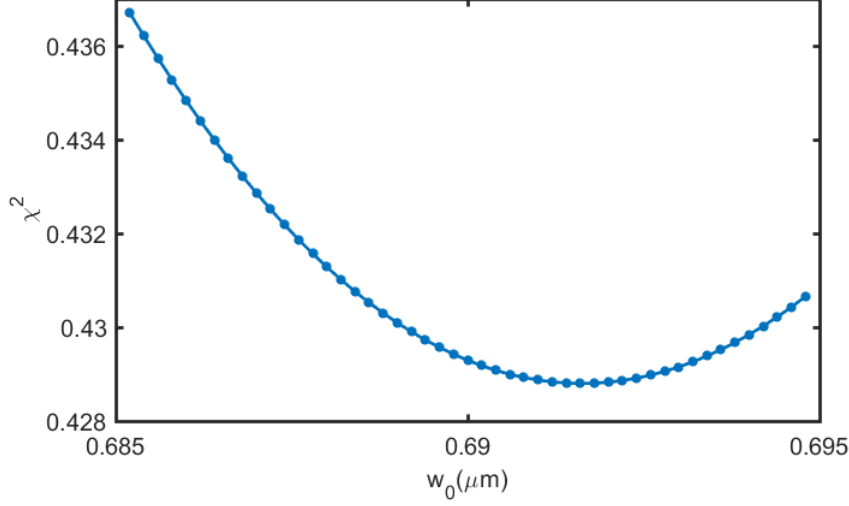


Figure 3.1 Example of the dependence of the value of  $\chi^2$  as function of the value of  $w_0$  used to define the Gaussian beam that is series expanded according to the technique described in Section 2. The step size in  $w_0$  goes down to 0.2 nm. The sampling procedure is the number 2.

One key ingredient in this procedure consist in the choice of a definite set of sampling points. We decide to always sample randomly the focal plan defined by  $z = 0$ . The choice of the randomization range and distribution is however extremely dependent on the application that is sought for. For instance, in the specific case of direct laser acceleration discussed in the introduction, it is difficult to decide *a priori* what sampling distribution is most appropriate i.e. the one that allows extracting the set of parameters for which, for instance, the beam energy versus initial position matches best the numerical results based on the numerical integrals from Ignatovsky formulation. Thus we have decided to treat the choice of the sampling distribution as a nuisance, and thus a systematic uncertainty on the extraction of the coefficients. To estimate this effect, five sampling methods are employed. They are listed below:

1. sampling points are Gaussian random distributed with  $\sigma_{x,y} = 0.5w_{0T}$ ,
2. sampling points are Gaussian random distributed with  $\sigma_{x,y} = w_{0T}$ ,
3. sampling points are uniformly random distributed with  $x, y$  ranging within  $(0, \lambda)$ ,
4. sampling points are uniformly random distributed with  $x, y$  ranging within  $(0, 3\lambda)$ ,

where

$$w_{0T} = \sqrt{\frac{w_i^2 - \sqrt{w_i^4 - 4\lambda^2 f^2/\pi^2}}{2}} = 0.63 \mu\text{m} \quad (3-11)$$

is the estimated waist of the paraxial beam, and all the sampling points of either method are taken on the focal plane. Alternatively to sample points in the plane  $z = 0$  they can also be distributed longitudinally. A uniform longitudinal distribution of points along the  $z$  axis in the range  $[0, z_R]$  has been investigated along with a transverse distribution of points corresponding to that of sampling number 2. It is found to give a result that lies in between those of samplings 2 and 4. The improvement is not significant.

The  $N_c$  parameters calculated with these four sampling methods and the related waist sizes are listed in Table. 3.1. Several remarks are in order. First of all, the  $x \leftrightarrow y$  symmetry seem approximately respected, which is expected for a perfectly aligned optical system. The scaling factor  $C_1$  does not change by more than 5% and the best fitted waist is stable within 1% and relatively close to the naive expectation  $w_{0T}$ , when considering several sampling distributions. This is somehow expected since these parameters are mainly driven by the overall normalization of the field and the paraxial approximation, respectively. The other parameters are varying more significantly, up to 50% in relative values. This is expected since their value is driven by the accurateness with which tails of the field distributions are fitted, which as expected depends on the transverse excursion of the sampling points far from the beam center. The obtained parameters do not correspond to values previously obtained<sup>[73]</sup> as expected from Ref.<sup>[71]</sup>. In any of the situation the obtained coefficients seem to fit relatively well the Ignatovsky solution. As can be seen on the Fig. 3.2 for the sampling distribution number 2, the residuals are within 1% relative to the maximum field value  $E_{x0} = E_x(0, 0, 0)$ . It is apparent that the first diffraction ring that is present in the Ignatovsky model on the  $E_x$  and  $E_z$  components is also present in the fitted series expansion though with a different amplitude, contrary to those in the  $E_y$  component. However second diffraction rings are not present. It is striking that despite the fit is performed in the  $z = 0$  plane, the obtained parameterization is also matching Ignatovsky model at  $z = z_R$  within a few per mil of the maximum field value, see Fig. 3.3. This represents a clear improvement in the approximation of the Ignatovsky model with analytic formulae from series expansions of the paraxial Gaussian beam<sup>[71]</sup>. We thus investigate the improvements obtained when introducing the next order correction in the series expansion, which adds 9 parameters to the fit. The results are given in

Figs.3.4 and 3.5. It is noticed that the description of the tails of the Ignatovsky model improves in the sense that the diffraction rings magnitude are better fitted than with the first order only. A diffraction ring the series expansion model appears in these plots for the  $E_y$  component which is a new feature with respect to the inclusion of the first order only. The presence of additional diffraction rings when considering higher order terms in the parameterization remains an open point but may well happen. The tails at  $z = z_R$  are impressively well fitted while the residual of the fit at  $(x = 0, y = 0, z = z_R)$  gets larger when the order 2 is included.

Table 3.1 Series expansion parameters that fit best Ignatovsky's model for the four sampling methods. The value of the  $\chi^2$  is also mentioned.

Sampling method	1	2	3	4
$C_1$	0.97	0.95	0.98	0.92
$C_{2,2,1}$	0.35	0.43	0.38	0.50
$C_{2,3,1}$	-0.025	-0.033	-0.030	-0.037
$C_{2,1,2}$	0.36	0.43	0.38	0.50
$C_{2,2,2}$	-0.050	-0.066	-0.067	-0.075
$C_{2,1,3}$	-0.025	-0.033	-0.029	-0.038
$\omega_0$ ( $\mu\text{m}$ )	0.69	0.69	0.68	0.69
$\chi^2$	0.07	0.43	0.42	0.14

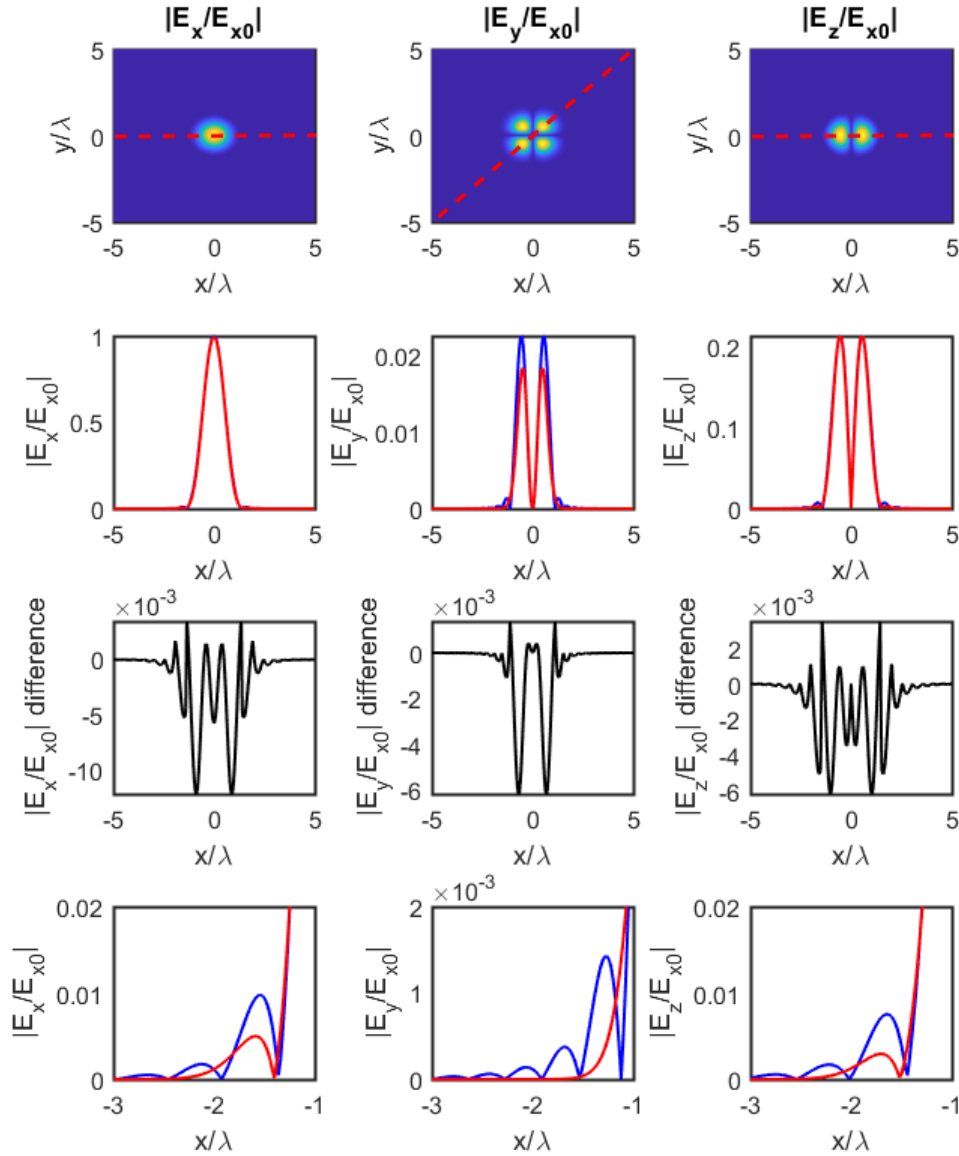


Figure 3.2 (Top) magnitude of the complex electric fields components at  $z = 0$  normalized by its maximum value in the focal plane  $E_x(0, 0, 0)$ . (Second line) normalized magnitude of the electric field components for the (blue) Ignatovsky model and the (red) generalized series expansion model on the axes that are represented by red dashed lines on the top plots. (Third line) difference between the curves of the middle plots. The differences are in the per mil range which is a clear improvement compared to the results presented in Ref.<sup>[71]</sup>. (Bottom) zoom on the tails in the region  $[-3\lambda, -\lambda]$  of the normalized magnitude of the electric field components for the (blue) Ignatovsky model and the (red) generalized series expansion model. These plots correspond to the series expansion composed of the first order term in the expansion and the sampling distribution number 2.

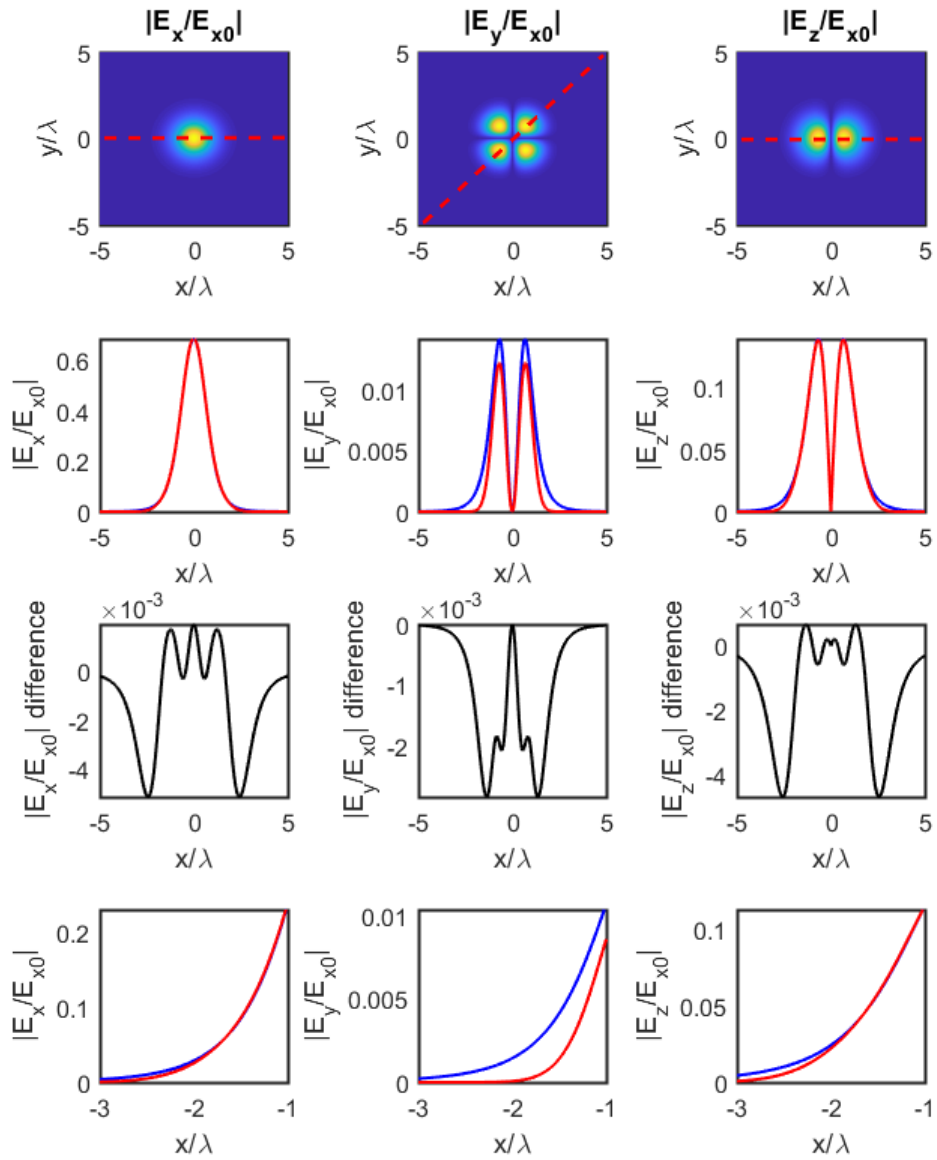


Figure 3.3 Same as Fig. 3.2 except that  $z = z_R$ .

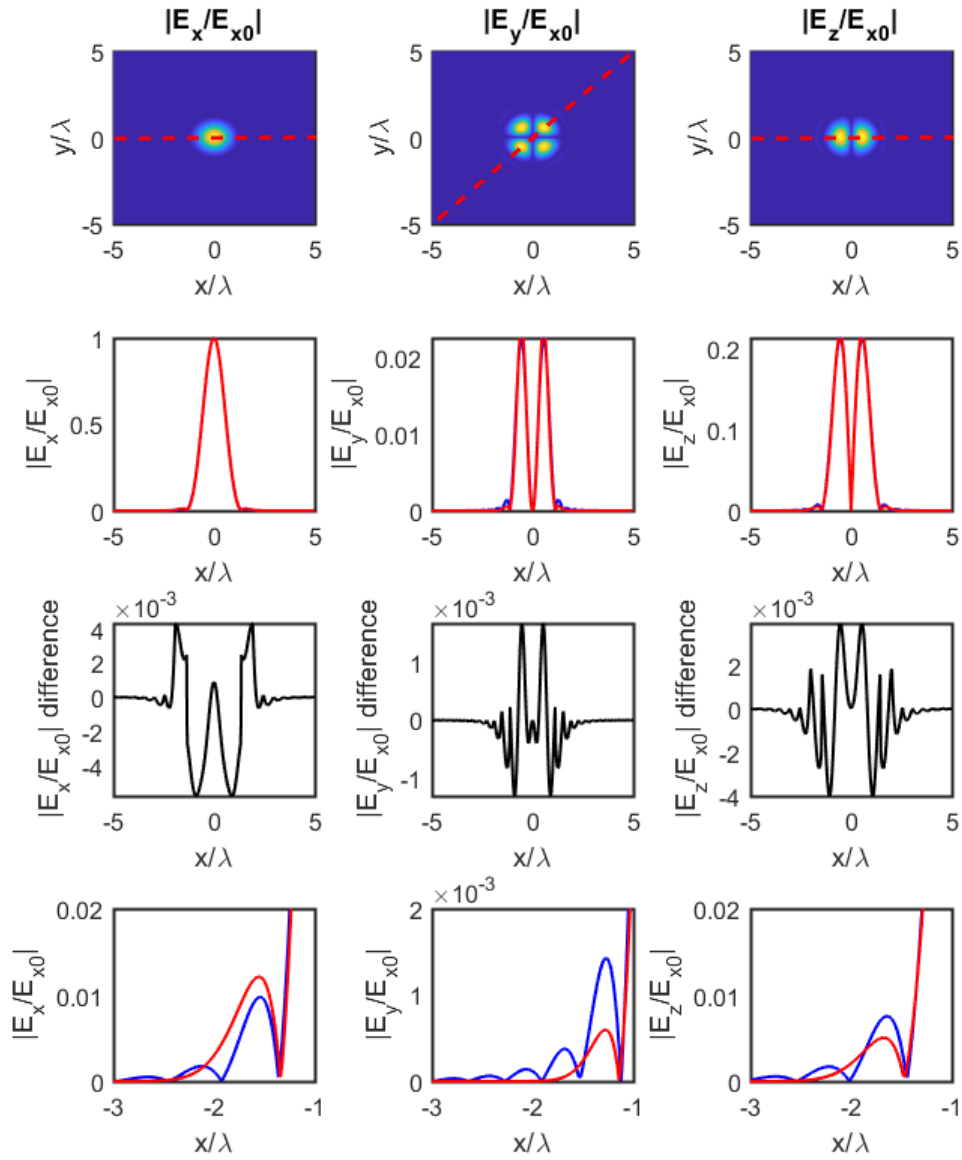


Figure 3.4 Same as Fig. 3.2 except that the series expansion is composed of the first and second order terms in the expansion.

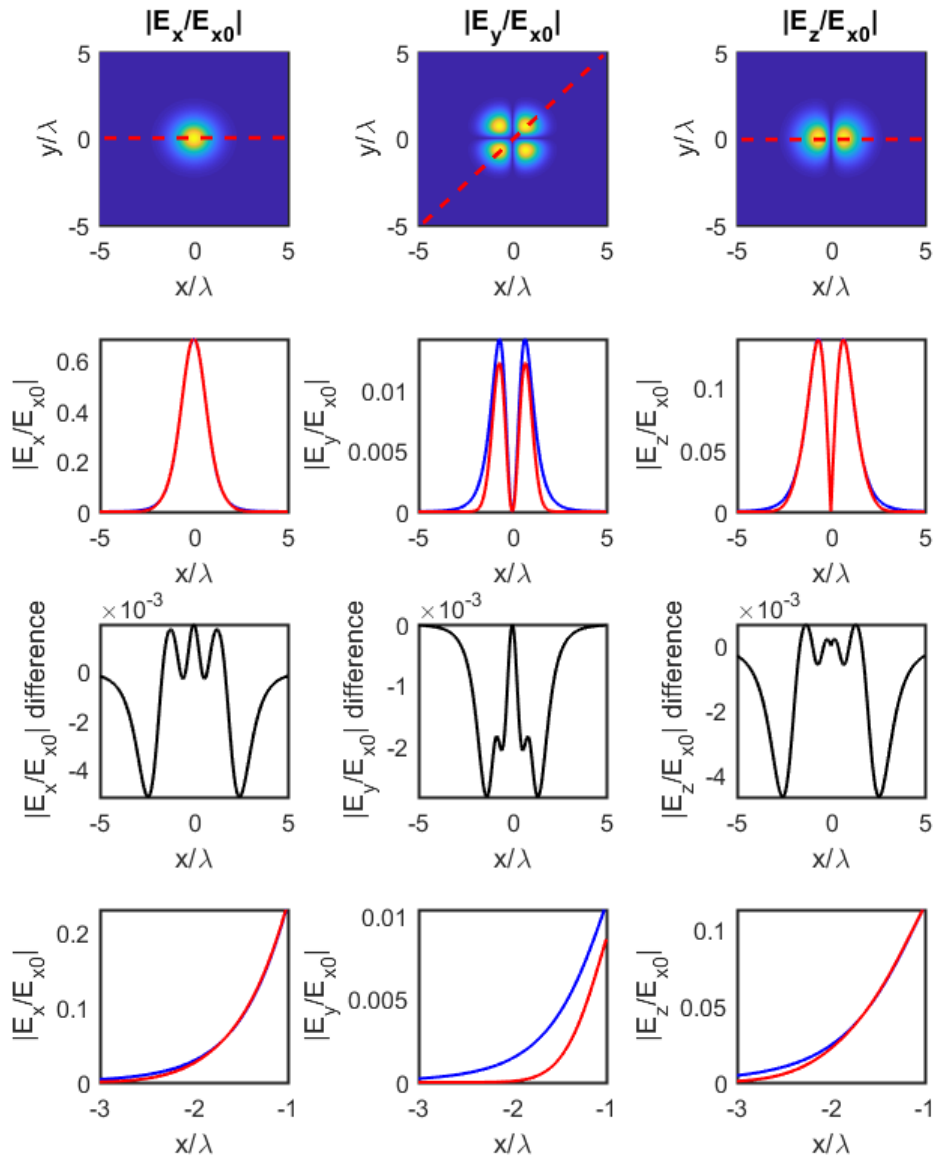


Figure 3.5 Same as Fig. 3.4 except that  $z = z_R$ .

## Chapter 4 Suppression of Modal Instabilities

ThomX, Thomson scattering light source located inside campus of Paris-Saclay University in France, is now under commissioning. Before the commissioning of the optical enhancement cavity (OEC) of ThomX, extensive R&D studies were done on the prototype OEC of ThomX which is called SBOX. The prototype SBOX is independent from electron storage ring to realize the design goals demanded for OEC itself. The goals include a laser beam waist with radius size of few tens of micrometers inside OEC, intra-cavity laser pulse length of  $\sim 10$  ps with repetition rate of few tens of MHz, and an hour-time-scale stable intra-cavity average power of few hundreds of kilowatts. The experimental setup of SBOX is presented in Section 4.1. During experiment, the injection laser power is gradually increased to increase the intra-cavity laser power. Modal instabilities began to show when intra-cavity average power reaches around 100 kW as presented in Section 4.2. The experimentally observed modal instabilities can be well described with mode degeneracy induced by mirror surface thermoelastic deformation which is presented in Section 4.3. Finally, in Section 4.4, method of D-shape mirror is brought up to be implemented close to the optical path between cavity mirrors to break the boundary conditions of high order modes which are degenerated with fundamental mode. Through simulation of cavity mode with ANSYS<sup>[84]</sup> and OSCAR<sup>[85]</sup> code, the capability of D-shape mirror to suppress modal instabilities is well proved and the experimental data of intra-cavity power change versus D-shape mirror position is well recovered. High power experiment is launched with implementation of D-shape mirrors inside cavity, an hour-time-scale stable intra-cavity average power of 200 kW is realized.

### 4.1 Prototype Cavity SBOX of ThomX

Prototype optical enhancement cavity (OEC) of ThomX, called SBOX, of which the experimental setup is schematically shown in Fig. 4.1. The OEC is in a four-mirror planar bow-tie structure with a round trip length of  $\sim 2.25$  m as shown more detailedly in Fig. 4.2. Distances  $L_1, L_2, L_3, L_4$  are designed to be [620, 454, 508, 674] mm,  $d = 75.1$  mm. Incidence angle on  $M_2$  is  $\theta = \alpha/2 = 4.76^\circ$ . Cavity mirrors  $M_1$  and  $M_2$  are planar mirrors,  $M_3$  and  $M_4$  are concave mirrors with radius of curvature of 0.5 m. SBOX is injected with laser of 1030 nm central wavelength. A laser beam waist with radius size

of  $83.8 \mu\text{m}$  on tangential axis and  $75.8 \mu\text{m}$  on sagittal axis is designed to be positioned in the middle between  $M_3$  and  $M_4$  as shown in Fig. 4.3.

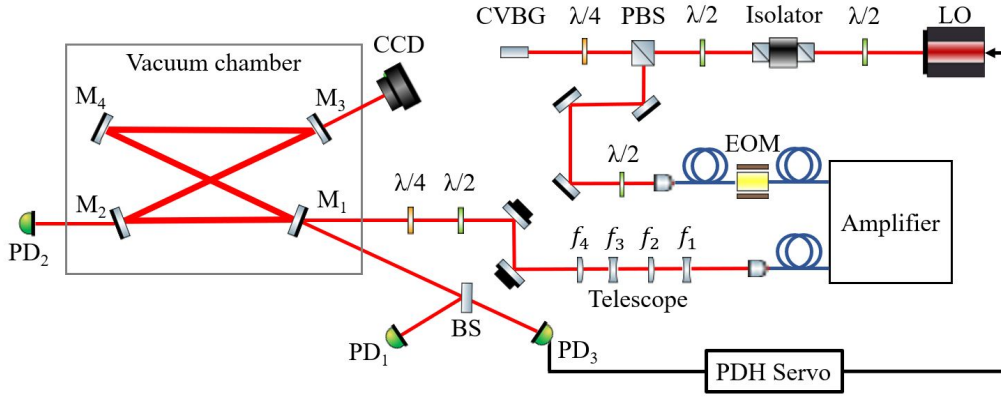


Figure 4.1 Experimental setup of SBOX. LO: laser oscillator. PBS: polarized beam splitter. CVBG: chirped volume Bragg grating stretcher. EOM: electro-optic modulator. BS: beam splitter. PD: photodiode. CCD: camera.

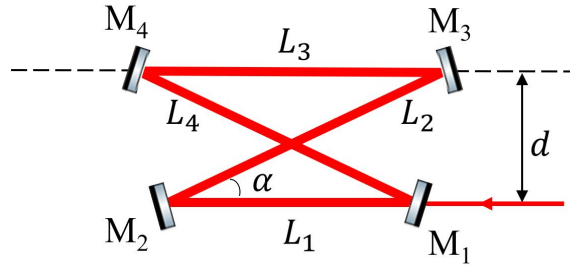


Figure 4.2 Optical enhancement cavity SBOX is in a four-mirror planar bow-tie structure. Distances  $L_1, L_2, L_3, L_4$  are  $[620, 454, 508, 674]$  mm,  $d = 75.1$  mm. Incidence angle on  $M_2$  is  $\theta = \alpha/2 = 4.76^\circ$ .

Intra-cavity laser beam waist size could be tuned by changing  $L_3$  as the relation of waist radius versus  $L_3$  shown in Fig. 4.4. Repetition rate of laser pulse circulating inside OEC could be tuned with changing OEC round trip length by changing  $L_1$  without varying much the laser beam waist size as shown in Fig. 4.5.

All four cavity mirrors are with 1" diameter and 1/4" thickness, the key parameters of which are summarized in Table. 4.1. The substrate of the injection coupling mirror  $M_1$  is made of very low absorption Suprasil glass while ultra low expansion (ULE) glass is used for  $M_2, M_3$  and  $M_4$  [58]. Cavity mirrors were coated with highly reflective coatings at Laboratoire des Matériaux Avancés (LMA) by using the ion beam sputtering (IBS) technique at the end of 2015. The highly reflective coatings are consist of quarter wave  $\text{Ta}_2\text{O}_5/\text{SiO}_2$  stacks designed for laser with 1030 nm central wavelength and an incident

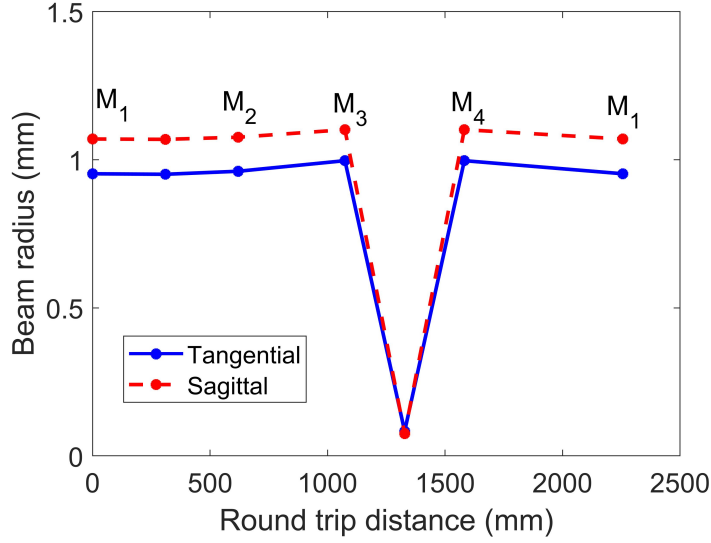


Figure 4.3 Laser beam radius size change inside SBOX on tangential (blue) and sagittal (red) axes with respect to the round trip distance starting from  $M_1$ . The texts " $M_1, M_2, M_3, M_4$ " mark the corresponding cavity mirror positions. A laser beam waist with radius size of  $83.8 \mu\text{m}$  on tangential axis and  $75.8 \mu\text{m}$  on sagittal axis exists in the middle position between cavity mirror  $M_3$  and  $M_4$ .

angle of  $4.76^\circ$ . Mirror optical properties were measured just after coating as summarized in Table 4.1. And the mirror substrates are backside anti-reflection coated. For cavity round trip loss (RTL) defined as

$$RTL = \sum_i^N (T_i + A_i + S_i), \quad (4-1)$$

in which  $N$  is the total number of cavity mirrors;  $T_i$ ,  $A_i$  and  $S_i$  are the power transmission, absorption and scattering coefficients of the  $i$ -th cavity mirror. And using the approximation

$$\rho^2 = 1 - RTL, \quad (4-2)$$

in which  $\rho$  is the effective cavity field reflection coefficient with consideration of all kinds of cavity power losses. While it has been defined as  $\rho = \prod_i^N r_i$  in Section 2.1.3 when considering no loss inside cavity except the noncomplete cavity mirrors' reflections. With the definitions in Eq. 2-11 and Eq. 2-12, the designed cavity linewidth, finesse and gain can be calculated with the parameters shown in Table 4.1 as 4.6 kHz, 29000 and 15000 respectively. The designed cavity finesse and gain is dominated by variation of  $T_1$ . With all other coefficients of cavity mirror transmission, absorption and scattering kept the same as shown in Table 4.1, the cavity finesse and gain versus the varying  $T_1$  are shown in Fig. 4.6, in which the black dashed lines indicate the condition of SBOX where

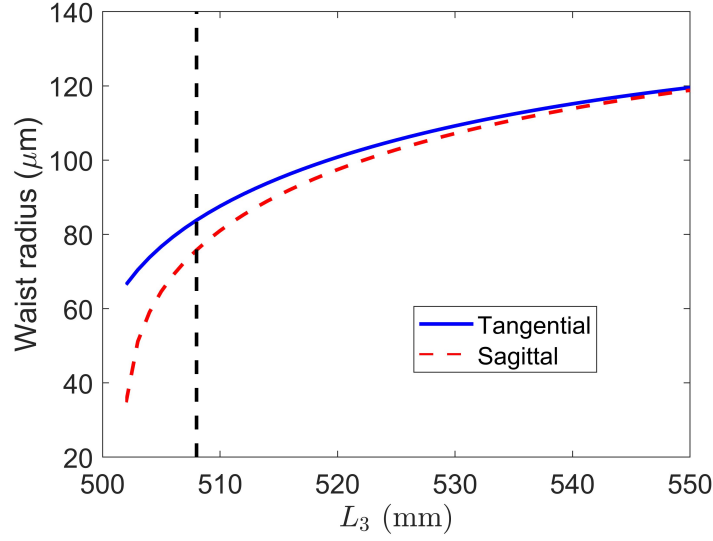


Figure 4.4 For SBOX, relation of intra-cavity laser beam waist radius versus  $L_3$  the distance between cavity mirror  $M_3$  and  $M_4$  when distances between other mirrors are fixed. Black dashed line indicates the condition of SBOX where  $L_3 = 508$  mm. Tuning of intra-cavity laser beam waist size could be realized by changing  $L_3$ .

$T_1=180$  ppm. From Fig. 4.6 we can see that SBOX works at a over-coupled regime where the gain curve is with a rather flat slope than the left side of the maximum gain. It means the SBOX cavity gain is rather less affected with the variation of  $T_1$ .

Table 4.1 Key parameters of SBOX cavity mirrors.

Mirror	Type	Substrate Material	Transmission (ppm)	Absorption (ppm)	Scattering (ppm)
$M_1$	Planar	Suprasil	180	1.00	9.0
$M_2$	Planar	ULE	3	1.15	5.0
$M_3$	Concave	ULE	3	1.27	4.3
$M_4$	Concave	ULE	3	1.20	4.3

The cavity mirrors are mounted inside a primary vacuum chamber with  $10^{-2}$  mbar residual pressure. The whole optical setup is located below an ISO5 air-flow as shown in Fig. 4.7. The cavity is seeded by an ultra-low phase noise femtosecond oscillator, Onefive ORIGAMI, of central wavelength 1030 nm and repetition rate 133.33 MHz. The laser beam is stretched to 250 ps, and then sent to a fiber amplifier (see Ref.<sup>[24]</sup> for details) to reach a maximum average power of 40 W. The low phase noise property of the laser oscillator is well maintained after amplification which makes it suitable to be injected into a high finesse cavity. The laser pulses are not compressed after amplification and

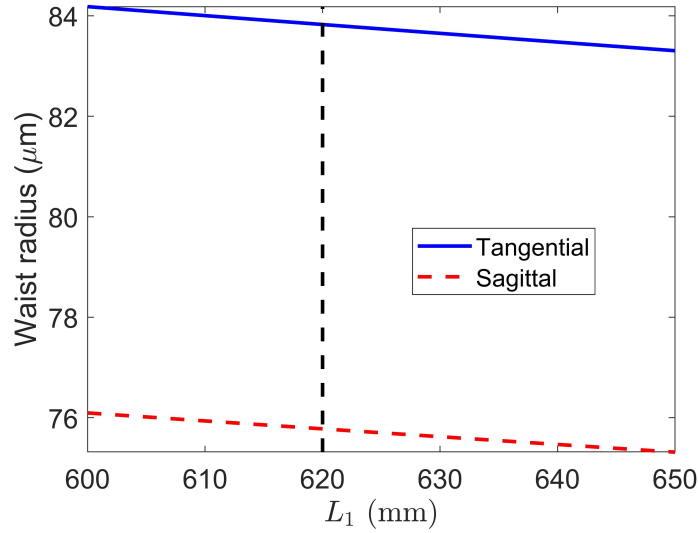


Figure 4.5 For SBOX, relation of intra-cavity laser beam waist radius versus  $L_1$  the distance between cavity mirror  $M_1$  and  $M_2$  when distances between other mirrors are fixed. Black dashed line indicates the condition of SBOX where  $L_1 = 620$  mm. Repetition rate of laser pulse circulating inside OEC could be tuned with changing OEC round trip length by changing  $L_1$  without varying much the intra-cavity laser beam waist size.

kept to 250 ps for cavity injection. The laser frequency-comb<sup>[86]</sup> is locked on the cavity round-trip frequency by the Pound-Drever-Hall (PDH)<sup>[62,87]</sup> technique.

A brief history of the SBOX performance is summarized as follows. The cavity gain and finesse measurements performed just after mirror coating manufacturing were consistent with the parameters in Table 4.1<sup>[31]</sup>. However, mirrors have been manipulated, vacuum has been broken, and intra-cavity average power of hundreds of kilowatts have been stacked many times during the following four years. Temperature sensors have also been glued inside the vacuum vessel. As a result, 400 kW intra-cavity average power was obtained with injection laser power of 40 W in 2017 for few seconds<sup>[31,34]</sup>. Later, phenomenon of modal instabilities began to be observed during experiment. With the implementation of a pair of D-shape mirrors, modal instabilities was successfully suppressed and stable intra-cavity power of 200 kW was achieved for hour time scale in 2018 with the same injection laser power of 40 W<sup>[88]</sup>, of which the details of this work will be introduced in following content of this chapter. Then efforts were put into investigating the reason of gain decrease with respect to intra-cavity average power increase. Mirror surface conditions were investigated using optical microscopes and atomic force microscopy (AFM)<sup>[89]</sup> but no defect was observed. A careful cleaning procedure, similar to the one described in Ref.<sup>[90]</sup>, was also applied before mirror installation but the intra-cavity power could

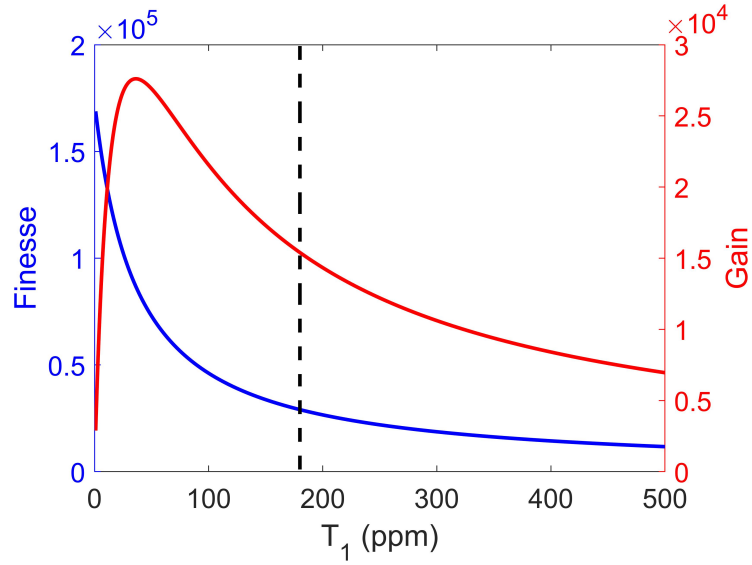


Figure 4.6 For SBOX, with all other coefficients of cavity mirror transmission, absorption and scattering kept the same as shown in Table 4.1, cavity finesse (blue) and cavity gain (red) versus transmission  $T_1$  of cavity mirror  $M_1$  are calculated by Eq. 2-11 and Eq. 2-12. The black dashed line indicates the condition of SBOX where  $T_1=180$  ppm with cavity finesse of 29000 and cavity gain of 15000, which is working at a over-coupled regime.

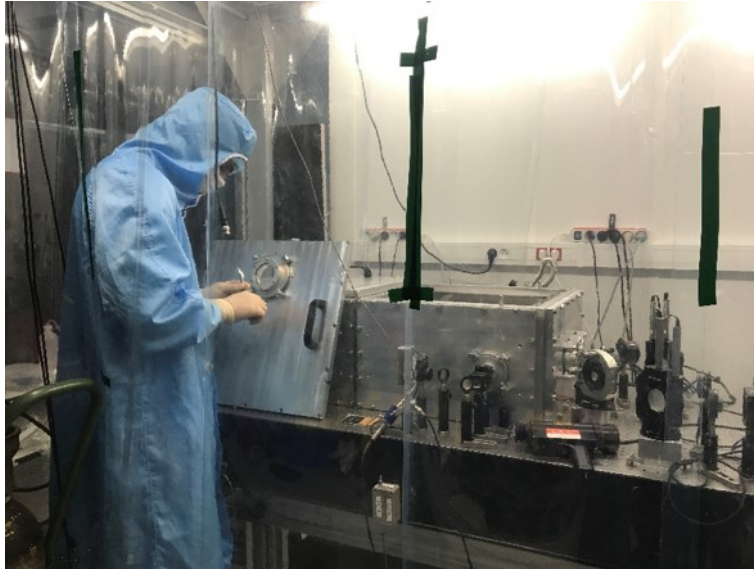


Figure 4.7 Photo of SBOX setup.

not be further increased. During the process of investigating gain decrease, in 2019, phenomenon of fast intra-cavity power drop was observed which finally led to unrecoverable mirror coating damage. With a post mortem analysis, a qualitative model was brought up to successfully explaining the prior-damage dynamics of cavity. The details of this work will be presented in Chapter 5. So until now, the problem of gain decrease is still open

and should be addressed in advance of future needs for intra-cavity average power at the megawatt level.

## 4.2 Observation of Modal Instabilities

During experiment, the injection laser power  $P_{in}$  was gradually increased to increase the intra-cavity power  $P_c$ . The modal instabilities began to be observed when  $P_c$  reached around 100 kW. Example screenshot of CCD camera image put at the transmission of  $M_3$  is shown in Fig. 4.8 when  $P_c$  was around 110 kW. The ideal cavity working mode  $TEM_{00}$  is superimposed with a high order mode, in which  $TEM_{00}$  mode is saturated in the center of the image aiming for capture of clear high order mode. The typical cavity transmission signal when modal instabilities occur measured by photodiode  $PD_2$  put at the transmission position of  $M_2$  is shown in Fig. 4.9, which is periodically separated into four stages: first, the cavity is locked to a single  $TEM_{00}$  mode, second the cavity switches to a degenerated mode, third the cavity reaches a steady state of degenerated mode, fourth the cavity enters a oscillation state whose amplitude of oscillation will finally be out of the adjustment range of feedback loop which leads to lose of lock. It takes about one second characteristically for cavity going through one period of the modal instabilities. The modal instabilities must be suppressed to make the cavity to be able to work stably at a time scale of hour to be used for Thomson scattering light sources.

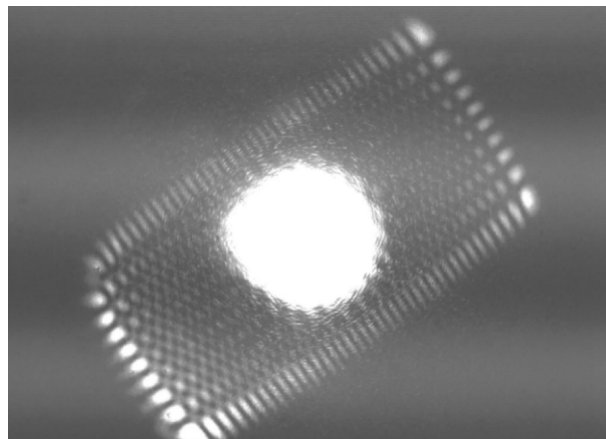


Figure 4.8 Screenshot of camera put at transmission position of  $M_3$  when modal instabilities occur at intra-cavity power around 110 kW. The ideal cavity working mode  $TEM_{00}$  is superimposed with a high order mode, in which the  $TEM_{00}$  is saturated to capture a clear high order mode.

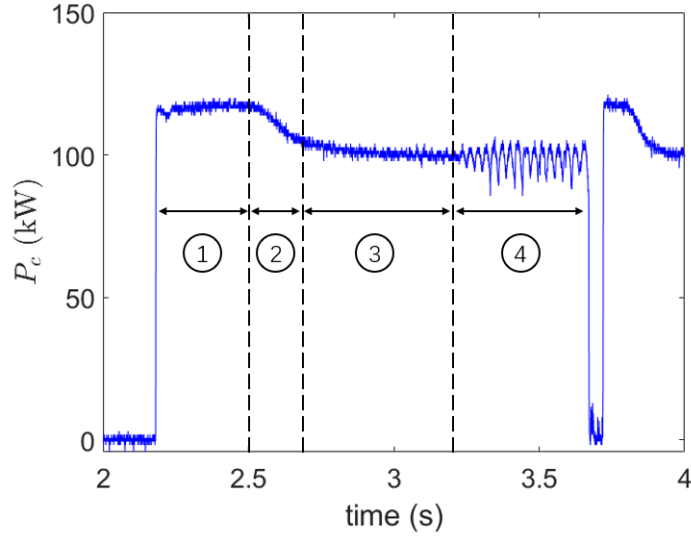


Figure 4.9 Typical intra-cavity power evolution when modal instabilities occur measured by photodiode PD<sub>2</sub> put at transmission position of M<sub>3</sub> then divided by the transmission coefficient of M<sub>2</sub> as shown in Table 4.1, which is periodically separated into four stages: first, the cavity is locked to a single TEM<sub>00</sub> mode, second the cavity switches to a degenerated mode, third the cavity reaches a steady state of degenerated mode, fourth the cavity enters a oscillation state whose amplitude of oscillation will finally be out of the adjustment range of feedback loop which leads to lose of lock.

### 4.3 Modeling of Modal Instabilities

To suppress the modal instabilities, first the reason of the modal instabilities must be understood. The modal instabilities of fundamental TEM<sub>00</sub> mode degenerated with high order mode are ascribed to thermoelastic deformation of mirror surface which is modeled by Winkler model<sup>[91]</sup> with ABCD matrix.

#### 4.3.1 Mirror Thermoelastic Deformation Characterized by Winkler Model

As the geometry shown in Fig. 4.10, it is considered in Winkler model that the laser power to thermal power conversion and absorption dominantly happens in dielectric coating, which is equivalently treated as the mirror surface, as the thickness of mirror coating is much smaller than that of the substrate. And thermoelastic deformation of mirror surface dominantly happens in the area with radius of  $w_m$  that of the laser beam radius on mirror, introducing a linear change of sagitta  $\delta s$  with respect to intra-cavity power  $P_c$  as

$$\delta s = \frac{\alpha A P_c}{4\pi k}, \quad (4-3)$$

in which  $\alpha$  is the thermal expansion coefficient of mirror substrate, the value of which is  $0.01 \times 10^{-6} \text{ K}^{-1}$  and  $0.6 \times 10^{-6} \text{ K}^{-1}$  for ULE and Suprasil respectively;  $k$  is the thermal

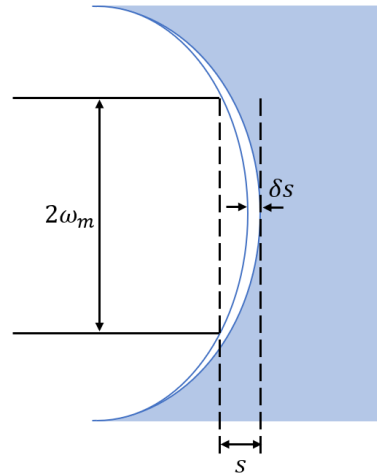


Figure 4.10 Illustrative plot of geometry used in Winkler model. Thermoelastic deformation of mirror surface dominantly happens in the area with radius of  $\omega_m$  that of the laser beam radius on mirror, introducing a linear change of sagitta  $\delta s$  with respect to intra-cavity power  $P_c$ .

conductivity of mirror substrate, the value of which is  $1.31 \text{ Wm}^{-1}\text{K}^{-1}$  and  $1.38 \text{ Wm}^{-1}\text{K}^{-1}$  for ULE and Suprasil respectively;  $A$  is the laser power to thermal power conversion and absorption coefficient which shall be taking the value of 1.2 ppm as measured by a *mirage* effect setup<sup>[92]</sup> at the factory of LMA. The precision of the measured  $A$  value is estimated to be 10 %. The mirror surface deformation calculated by Winkler model with the intra-cavity power range from 0 to 500 kW is shown in Fig. 4.11.

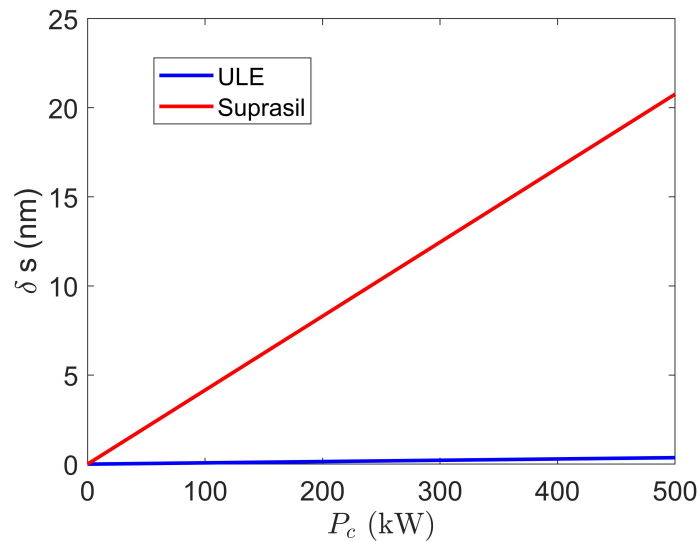


Figure 4.11 For SBOX, mirror surface deformation of cavity mirror with substrate of ULE (blue) and Suprasil (red) calculated by Winkler model.

As the mirror surface is locally treated as spherical, we have the relation  $s \approx$

$w_m^2/(2R)$ , in which  $R$  is the radius of curvature of the concave cavity mirror surface. The deformed radius of curvature of mirror surface can be written as

$$\frac{1}{R'} = \frac{1}{R} - \frac{\alpha A P_c}{2\pi k w_m^2}. \quad (4-4)$$

The change of radius of curvature  $\delta R = R' - R$  of SBOX concave cavity mirror calculated by Winkler model with the intra-cavity average power range from 0 to 500 kW is shown in Fig. 4.12. The difference of  $\delta R$  on tangential and sagittal axes is because of the different laser beam size on mirror along the two axes which is resulted from the astigmatism of the cavity. The cavity astigmatism can be described by the asymmetry transferring matrix along tangential and sagittal axes.

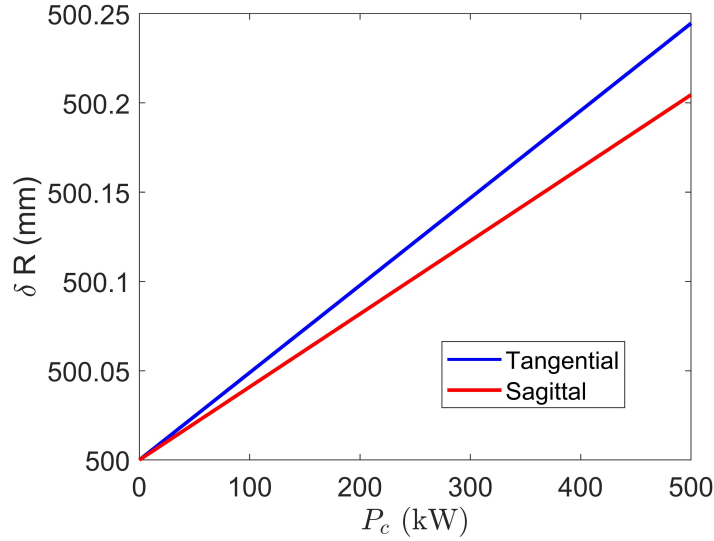


Figure 4.12 Radius of curvature change on tangential axis (blue) and sagittal axis (red) of SBOX concave cavity mirror calculated by Winkler model.

For SBOX transferring matrix expressed as below, the matrix multiplication is calculated with left multiplying that the multiplication is in the order from right to left.

$$\begin{aligned} T_x &= \begin{bmatrix} 1 & 0 \\ -\frac{2}{R_3} \frac{1}{\cos\theta} & 1 \end{bmatrix} \begin{bmatrix} 1 & L_1 + L_2 \\ 0 & 1 \end{bmatrix} \begin{bmatrix} 1 & L_4 \\ 0 & 1 \end{bmatrix} \begin{bmatrix} 1 & 0 \\ -\frac{2}{R_4} \frac{1}{\cos\theta} & 1 \end{bmatrix} \begin{bmatrix} 1 & L_3 \\ 0 & 1 \end{bmatrix}, \\ T_y &= \begin{bmatrix} 1 & 0 \\ -\frac{2}{R_3} \cos\theta & 1 \end{bmatrix} \begin{bmatrix} 1 & L_1 + L_2 \\ 0 & 1 \end{bmatrix} \begin{bmatrix} 1 & L_4 \\ 0 & 1 \end{bmatrix} \begin{bmatrix} 1 & 0 \\ -\frac{2}{R_4} \cos\theta & 1 \end{bmatrix} \begin{bmatrix} 1 & L_3 \\ 0 & 1 \end{bmatrix}, \end{aligned} \quad (4-5)$$

The mode side on cavity mirror  $M_3$  can be calculated from  $q$  parameter as defined in Eq. 2-6 by solving the equation  $q = \frac{Aq+B}{Cq+D}$ . The evolution of cavity fundamental mode size change versus intra-cavity power calculated by Winkler model is shown in Fig. 4.13. The mode will become more elliptical with major axis along sagittal direction with increasing

intra-cavity power.

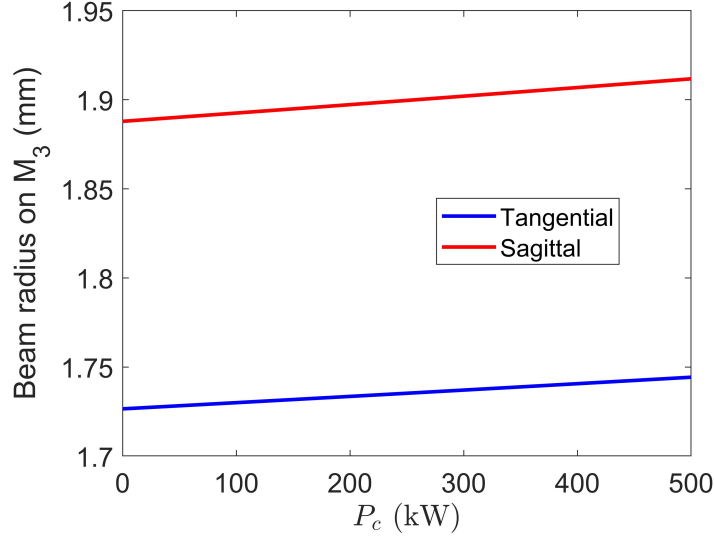


Figure 4.13 The change of SBOX fundamental mode size on  $M_3$  versus intra-cavity average power calculated by Winkler model. The mode will become more elliptical with major axis along sagittal direction with increasing intra-cavity power.

#### 4.3.2 Modal Instabilities Induced by Mode Degeneracy

The resonance condition for  $TEM_{mn}$  regulating that the phase change in one cavity round trip  $L$  is integer of  $2\pi$  as

$$(m + n + 1)\zeta(L) + 2\pi\frac{L}{\lambda} = p \cdot 2\pi, \quad (4-6)$$

in which  $\zeta$  is the Gouy phase defined in Eq. 2-5,  $p$  is integer. For SBOX with an intra-cavity power in the range of 0 to 500 kW and calculated by ABCD matrix, the lowest orders of high order mode degenerated with  $TEM_{00}$  are shown in Fig. 4.14, without considering the limitation from the finite mirror size.

The difference of the calculated order of degenerated high order mode with that of the experimentally observed ones could come from the uncertainties in the mirror-coating absorption coefficient and the radius of curvatures of mirrors. The calculated order could be matching with the experimental data with an increase of radius of curvature of the concave mirrors by  $170 \mu\text{m}$ , compared to a  $\pm 1 \text{ mm}$  manufacturing precision. So it is considered that the experimental observation of the modal instabilities could be satisfactorily described through mirror surface thermoelastic deformation by Winkler model.

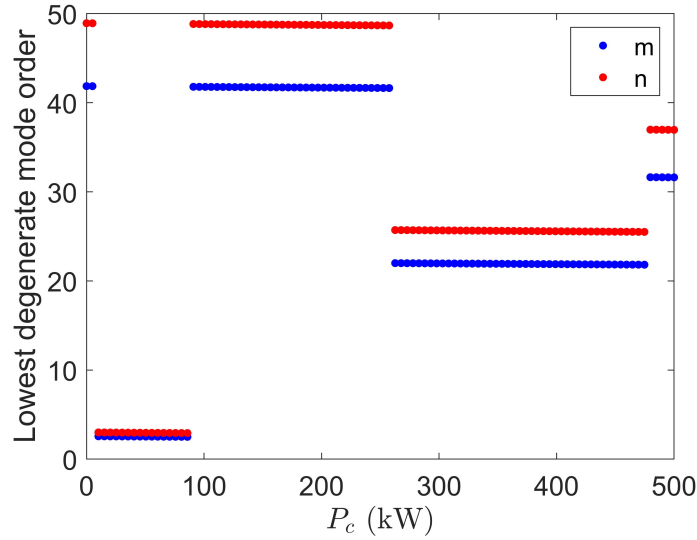


Figure 4.14 For SBOX with intra-cavity average power  $P_c$  range from 0 to 500 kW, the lowest order of high order modes degenerated with  $TEM_{00}$ , in which  $m$  corresponds to the mode order on tangential axis,  $n$  corresponds to the mode order on sagittal axis. The calculation is without considering the limitation from the finite mirror size.

#### 4.4 Implementation of D-shape Mirrors for Suppressing Modal Instabilities

As one can see from Fig. 4.14 that the degenerated mode orders are pretty high and the Gaussian laser beam size is scaling as  $\sqrt{nw_{00}}$  for a large  $n$ <sup>[67]</sup>, in which  $w_{00}$  is the beam radius of  $TEM_{00}$ . Inspired by the method of inserting a pinhole in the middle of a QED cavity to remove high order mode by increasing the losses of the high order transverse mode<sup>[93]</sup>, and considering the conditions of a cavity used for Thomson scattering experiment that it is designed to be working at high power state, which will potentially lead to the damage of any absorbing optical element, so it's not proper to implement pinhole inside OEC for Thomson scattering. And the laser beam in between  $M_3$  and  $M_4$  is designed to be scattering with electron beam which makes it impractical for inserting extra optical elements in the proximity of the interaction point. So a method of inserting a pair of D-shape mirrors in between  $M_1$  and  $M_2$  is proposed as schematically shown in Fig. 4.15. D-shape mirrors  $D_1$  and  $D_2$  are separately mounted on optical stages connected to motors thus can be separately moved tangentially and sagittally. The knife-edge mirrors are chosen to be placed in an angle of 175 mrad with respect to the laser beam, thus the high order beams are reflected from D-shape mirrors to vacuum chamber walls rather than cavity mirrors, resulting in effective dump of high order mode.

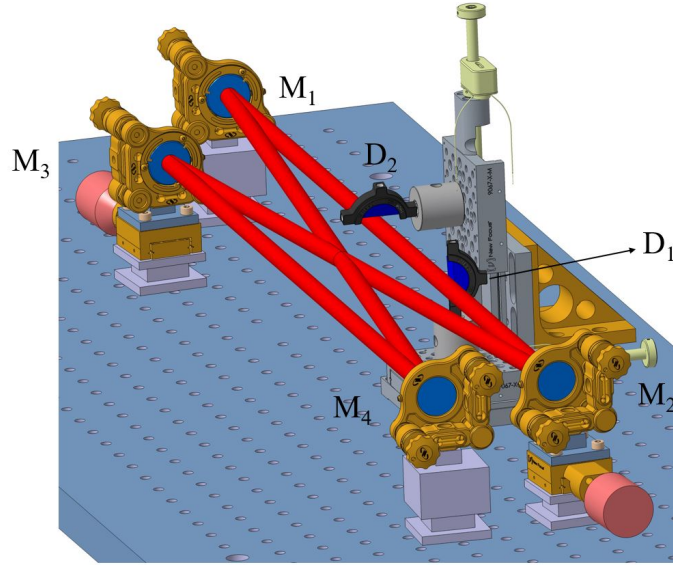


Figure 4.15 Schematic drawing of implementation of D-shape mirrors inside SBOX.

#### 4.4.1 Simulation of Cavity Mode with Implementation of D-shape Mirrors

Simulations were done to show the effectiveness of D-shape mirrors for dumping high order mode. The mirror surface deformations are calculated with ANSYS<sup>[84]</sup> using a 2D axisymmetric geometry of cavity mirror as shown in Fig. 4.16. The same flat surface geometry is used for simulation of concave mirror with neglecting the curved surface as its sagitta is less than 1% of the mirror diameter. Taking a timing constant heat source with average power of 0.1 W, it is equivalent to an average intra-cavity power of 100 kW with absorption coefficient  $A = 1$  ppm. The heat source is set with  $1/e^2$  radius of 1 mm Gaussian distributed on  $M_1$  surface. Heat absorption is considered to be happening in mirror coating and equivalently set as the mirror surface since the thickness of mirror coating is much smaller than thickness of mirror body. The temperature distribution in mirror body is calculated with the Gaussian distributed heat applied on line  $oa$ . Heat radiations with emissivity of 0.9 are set on all outer surfaces of mirror body which are lines  $oa$ ,  $ab$  and  $bc$  in Fig. 4.16. Perfect insulation is set defaultly by ANSYS at the axisymmetric axis  $oc$ . Then the temperature distribution of mirror body is imported to *Static Structural* calculation in ANSYS. The structural boundary condition is set as the point  $b$  with zero displacement on  $z$  axis, which has been checked the deformation result being consistent with that of 3D geometry with the cavity mirror mount (Newport ZeroDrift thermally compensated mirror mount) mechanical design file implemented into ANSYS. Example results of mirror surface deformation are shown in Fig. 4.17. To compare with the results calculated with Winkler model, the Suprasil mirror surface deforms  $\sim 5$  nm for

$P_c = 100$  kW as shown in Fig. 4.11, it can be interpreted as an globally averaged effect of the results shown in Fig. 4.17 since the Winkler model is a linear model for describing the mirror surface thermoelastic deformation.

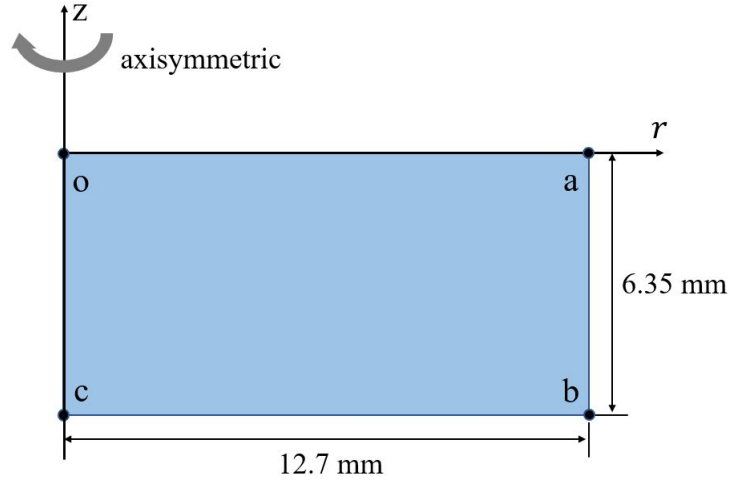


Figure 4.16 2D axisymmetric geometry of cavity mirror used in ANSYS for calculation of mirror surface deformation.

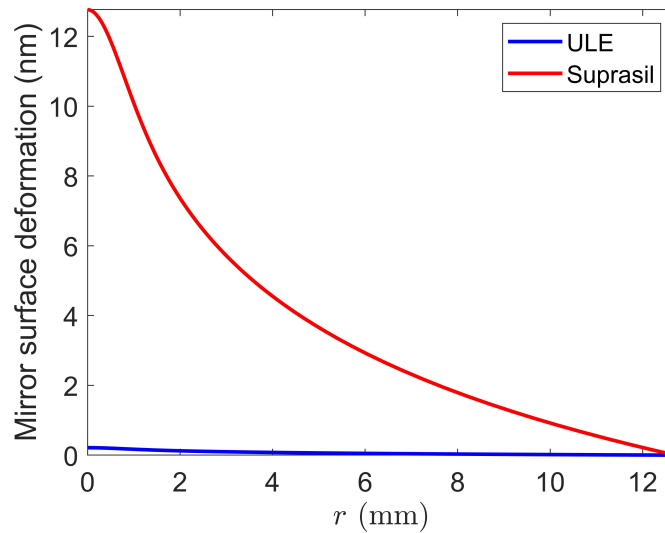


Figure 4.17 Deformations of mirror surfaces with substrate material of ULE (blue) and Suprasil (red) with 0.01 W constant heat power Gaussian distributed on mirror surfaces with a  $1/e^2$  radius of 1 mm, calculated through ANSYS using the mirror geometry shown in Fig. 4.16. It is corresponding to the deformation on line  $oa$  in Fig. 4.16.

Then the mirror surface deformation data are imported into OSCAR<sup>[85]</sup> code for calculation of cavity mode. The pair of D-shape mirrors are implemented using function

*mask* of OSCAR code and the setting is shown in Fig. 4.18, with the D-shape mirror edges positioned at  $D_x = D_y = 3$  mm with respect to center of cavity mirror  $M_2$ . Cavity mode profiles without and with D-shape mirrors implementation are separately shown in Fig. 4.19(a) and Fig. 4.19(b). The different degenerated high order mode compared to that shown in Fig. 4.14 is resulted from the different calculation method of mirror surface deformation and cavity mode. Through comparison between Fig. 4.19(a) and Fig. 4.19(b), one sees that the modal instabilities could be effectively suppressed by D-shape mirrors.

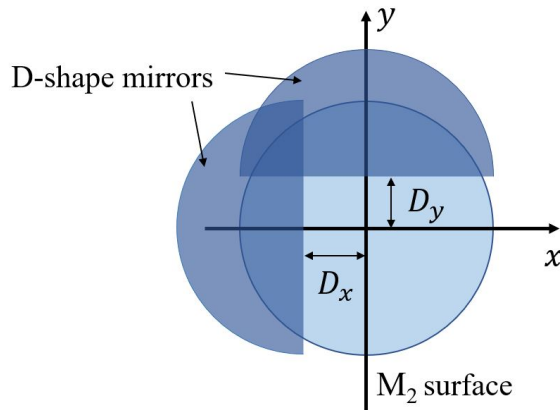


Figure 4.18 The pair of D-shape mirrors are implemented using function *mask* of OSCAR code with the D-shape mirrors' edges positioned at  $D_x$  and  $D_y$  with respect to center of cavity mirror  $M_2$ .

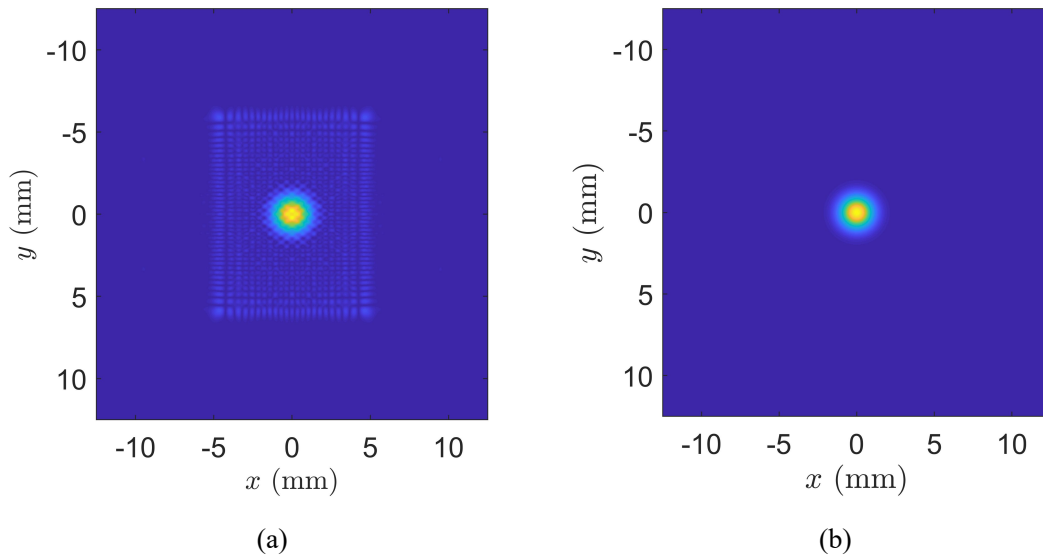


Figure 4.19 Simulation results proving the capability of D-shape mirrors dumping high order mode. (a) cavity mode profile on  $M_1$  without D-shape mirrors, (b) cavity mode profile on  $M_1$  with the pair of D-shape mirrors.

#### 4.4.2 High Power Experiments with Suppression Modal Instabilities

D-shape mirrors were then implemented inside cavity. Test of the D-shape mirrors performance is done by investigating the intra-cavity power change versus the different D-shape mirror positions. Intra-cavity average power  $P_c$  is calculated from measurement of cavity transmission average power made by power meter put at transmission position of  $M_4$  with division of the power transmission coefficient of  $M_4$ . Fig. 4.20 shows intra-cavity power change versus D-shape mirror relative displacement of  $D_x$  on tangential axis and of  $D_y$  on sagittal axis. We can see from the flat part of the curves that there exist positions of D-shape mirrors where degenerated high order transverse mode can be successfully removed and stabilized state reached by cavity, where also the losses of fundamental mode are negligible. And the behavior of intra-cavity power versus D-shape mirrors displacement are different on tangential and sagittal axis which can be attributed to the asymmetry increase of the ellipticity of the planar-cavity beam size in the two axes<sup>[58]</sup>. Experimentally, proper positions of D-shape mirrors can be chosen by moving the D-shape mirror position to where no high order mode and no clear variation of cavity transmission power is observed.

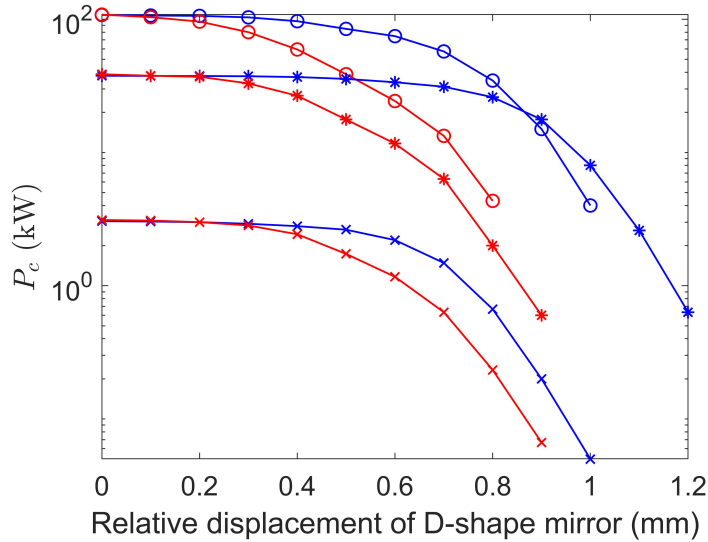


Figure 4.20 Intra-cavity power change versus D-shape mirror relative displacement of  $D_x$  on tangential axis (blue) and of  $D_y$  on sagittal axis (red). When one D-shape mirror is being moved, the other one is not implemented. Points in symbol "o, \*, x" separately show data of intra-cavity power optimally to be 117 kW, 40 kW and 3.3 kW.

The power change versus D-shape mirror positions shown in Fig. 4.20 can be consistently recovered by simulation as the comparison of data set with  $P_c \sim 117$  kW shown

in Fig. 4.21. The simulation follows the same procedure that has been described above using ANSYS and OSCAR. The  $y$  axis of normalized intra-cavity average power is calculated by dividing the maximum that is  $\overline{P}_c = P_c / 117 \text{ kW}$ . The absolute D-shape mirror position of the experimental data shown in Fig. 4.20 can be pinned down through a fit with the simulation data. The zero displacement positions of the curves for  $P_c = 117 \text{ kW}$  are corresponding to  $D_x = 2.62 \text{ mm}$ ,  $D_y = 2.50 \text{ mm}$  with a precision of  $\pm 0.01 \text{ mm}$ . The stepping behavior showing up in the simulation curves in Fig. 4.21 where  $\overline{P}_c$  kept being constant at some ranges is resulted from the noncontinuous change of intra-cavity average power with noncontinuous mode order when D-shape mirror moves.

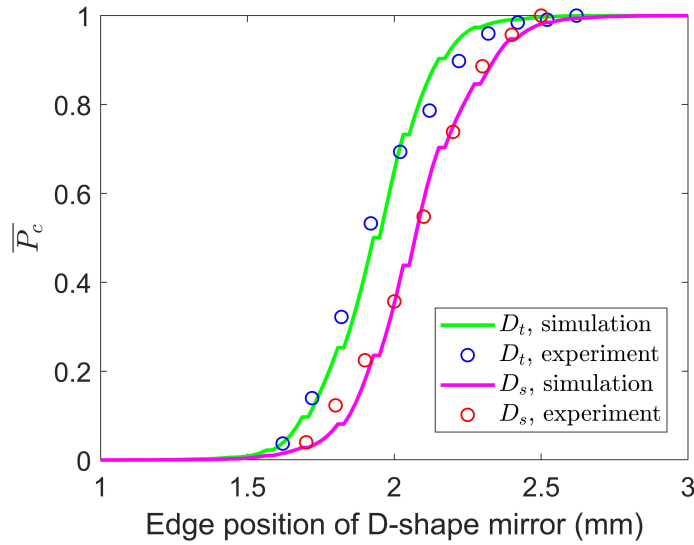


Figure 4.21 Experimental data (in symbol "o") same as the dataset with  $P_c \sim 117 \text{ kW}$  shown in Fig. 4.20, and simulation data on tangential axis (green) and sagittal axis (magenta). For this dataset, the absolute edge positions of D-shape mirror for the zeros displacement positions in Fig. 4.20 are fitted to be  $D_x = 2.62 \text{ mm}$ ,  $D_y = 2.50 \text{ mm}$  with a precision of  $\pm 0.01 \text{ mm}$ .

High power experiments are launched with the implementation of D-shape mirrors inside cavity. As the experimental data shown in Fig. 4.22, the intra-cavity power is calculated with measurement of photodiode  $PD_2$  put at transmission position of  $M_2$  as shown in Fig. 4.1, and divided by the transmission coefficient of  $M_2$  shown in Table 4.1. As a result of the successful suppression of modal instability with D-shape mirrors, intra-cavity power stabilized at  $\sim 200 \text{ kW}$  and data were recorded for 30 min, during which no alignment and correction has been done and intra-cavity power dropped from 205 kW to 197 kW due to the thermal stabilization of the cavity. The optimum intra-cavity power of 205 kW can be recovered with quick optimization of the alignment and feedback

system. With radius at  $1/e^2$  of the maximum with Gaussian fit approximately to be 1.8 mm on tangential axis and 2 mm on sagittal axis, the intra-cavity average power of 200 kW is corresponding to a laser energy density of  $\sim 0.01 \text{ J/cm}^2$  on mirror surface, which is much lower than the laser-induced-damage-threshold at a level of  $\sim 1 \text{ J/cm}^2$  as reported in Ref.<sup>[94]</sup> from measurement done with single-pulse irradiation of 500 fs laser pulse with central wavelength 1030 nm.

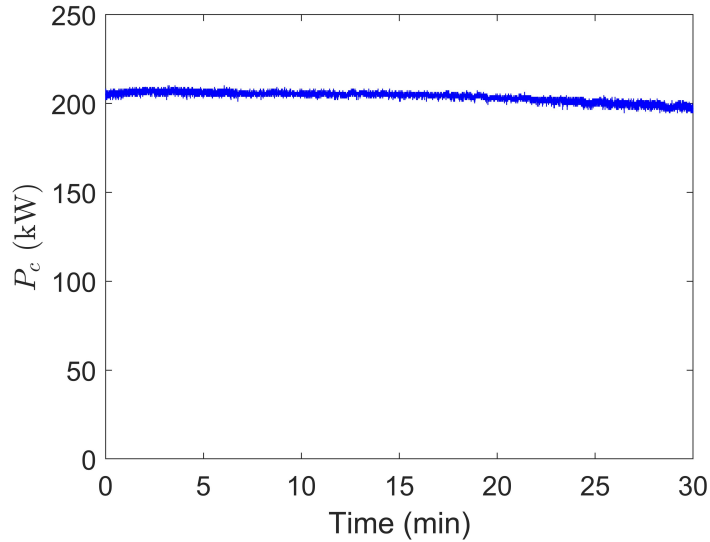


Figure 4.22 Intra-cavity average power of SBOX for 30min with 40W injection laser power.

As it can be seen from Fig. 4.23 the comparison of intra-cavity average power versus injection laser average power between year 2017 and 2018, the cavity gain dropped from 9100 to 5500 with the same injection laser average power of 40 W. The reason of gain drop needs to be understood and the optimum cavity gain needs to be recovered.

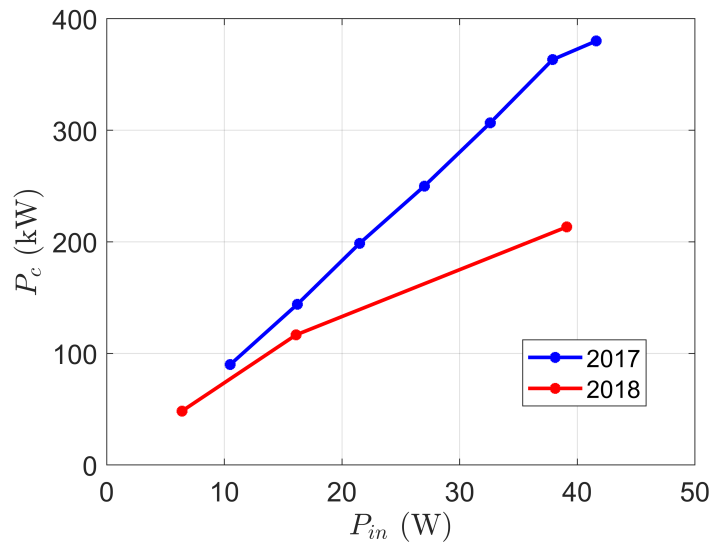


Figure 4.23 Comparison of intra-cavity average power versus injection laser average power between year 2017 and 2018.

## Chapter 5 Study of Prior-damage Dynamics

After achieving the 200 kW intra-cavity average power in 2018, with the purpose of investigating the reason of cavity gain decrease, extensive R&D works were done on the SBOX experimental setup which has been shown in Section 4.1 with implementation of the pair of D-shape mirrors as shown in Section 4.4.2. A prior-damage phenomenon is observed in 2019 which is presented in Section 5.1. The phenomenon behaves with fast intra-cavity average power drop with magnitude and time scale depending on the power level. Increasing further the incident laser power led to irreversible damage of the cavity coupling mirror surface. The origin of this phenomenon is investigated with *post mortem* mirror surface imaging and analysis of the signals reflected and transmitted by the optical enhancement cavity. Scattering losses induced by surface deformation due to a hot-spot surface contaminant is found to be most-likely the dominant physics process behind this phenomenon as presented in Section 5.2. A good consistency is achieved between the simulation results using the hot-spot model with the experimental data, which is presented in Section 5.3.

### 5.1 Observation of Prior-damage Phenomenon

For investigating reason of gain decrease issue as presented in the end of Section 4.4.2, R&D works were launched on the experimental setup as shown in Fig. 5.1, which is the experimental setup that has been described in Section 4.1 with implementation of the pair of D-shape mirrors as shown in Section 4.4.2 to suppress modal instabilities. Prior-damage phenomenon was observed on the SBOX optical enhancement cavity in 2019.

During the power up experiments, the injection laser beam average power  $P_{in}$  was incremented step by step. At each step, the optical intensity on PD<sub>3</sub> is tuned to remain constant in order to avoid saturation and the proportional–integral–derivative (PID) feedback parameters are checked (and slightly adjusted if necessary) to maximize the intra-cavity power for each input power. The intra-cavity average power  $P_c$  was inferred from the signal of PD<sub>2</sub>. The transmission of each of the four cavity mirrors has been regularly measured during the four years of operations. Results consistent with the values reported in Table 4.1 were always obtained. The reflected average power  $P_r$  was inferred from PD<sub>1</sub>.

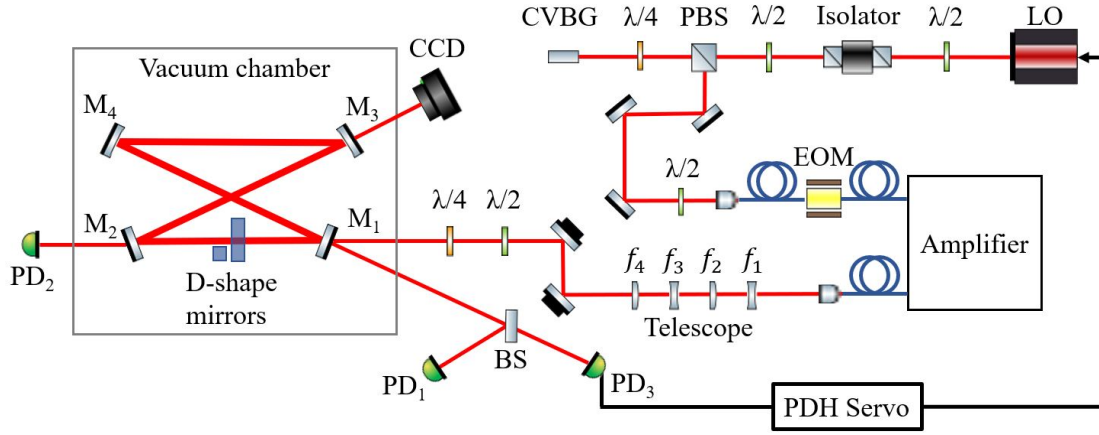


Figure 5.1 Experimental setup of SBOX with implementation of the pair of D-shape mirrors. LO: laser oscillator. PBS: polarized beam splitter. CVBG: chirped volume Bragg grating stretcher. EOM: electro-optic modulator. BS: beam splitter. PD: photodiode.

The calibrated  $PD_1$  and  $PD_2$  photodiodes are readout by a large bandwidth oscilloscope.

For  $P_{in} > 1$  W, a clear fast drop of  $P_c$  as a function of time appears right after cavity locking. Measurements of  $P_c$  and  $P_r$  as a function of time for various  $P_{in}$  values are shown in Figs. 5.2 and 5.3 respectively. Six datasets were recorded. A large cavity gain decrease is observed for  $P_{in} = 28.7$  W. Mirror surfaces were inspected after experiment. It turned out that  $M_1$  has been damaged at  $P_{in} = 28.7$  W as shown in Fig. 5.4. A crater with radius  $\sim 25 \mu m$  is positioned at the center of coupling mirror surface. A crack zone around the crater extends the damage area with radius up to  $\sim 100 \mu m$ . So that the first five sets of data correspond to a prior-damage regime. Steep and fast drops are observed in Fig. 5.2 whereas time variations are smooth in Fig. 5.3. This is another feature that a realistic model may describe.

We define  $t = 0$  as the instant when  $P_c$  reaches its maximum.  $P_{c,i}$  and  $P_{r,i}$  correspond to the values of  $P_c$  and  $P_r$  at  $t = 0$  respectively; the steady state values of  $P_{c,f}$  and  $P_{r,f}$  are defined by the average values of  $P_c$  and  $P_r$  over the time interval  $[1s, 2s]$ . We also introduce the relative steady state average power drop  $\Delta = 1 - P_{c,f}/P_{c,i}$ . The characteristic half power drop time  $t_{1/2}$  is defined as the time it takes for  $P_c$  to drop from its maximum value down to  $(P_{c,i} + P_{c,f})/2$ . The cavity gain is estimated at  $t = 0$  by  $G_{c,i} = P_{c,i}/P_{in}$ . These parameters are summarized in Table 5.1. The expected relative uncertainty on parameters in Table 5.1 depends on the accuracy of the power meter, the noise of the oscilloscope wave-form measurements, feedback parameter tuning and beam alignments. We estimate a conservative relative uncertainty of 5 – 10 % on our measurement quantities. Since we are looking for a qualitative model, we will not account further

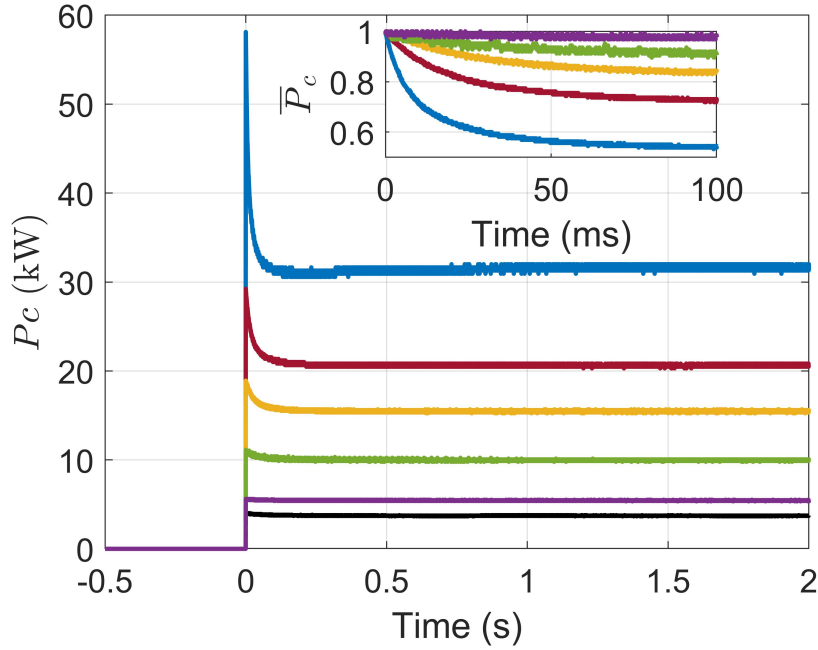


Figure 5.2 Experimental measurements of the SBOX intra-cavity power  $P_c(t)$  as a function of time for various values of injection laser beam average power  $P_{in}$ . The six datasets are shown, from the top to the bottom:  $P_{in} = 16.4$  W (blue), 7.9 W (red), 5.1 W (yellow), 2.9 W (green), 1.5 W (purple) and 28.7 W (black). The last dataset has been shifted by -2 kW. The inset plot shows the normalized intra-cavity power  $\bar{P}_c(t) = P_c(t)/P_{c,i}$  between 0 and 100 ms. Only five of the six datasets are shown, from the bottom to the top:  $P_{in} = 16.4$  W (blue), 7.9 W (red), 5.1 W (yellow), 2.9 W (green) and 1.5 W (purple).

for measurement uncertainties.

According to Table 5.1 and Fig. 5.2, the steady state power drop  $\Delta$  increases from 3.6 % for  $P_{in} = 1.5$  W to 46 % for  $P_{in} = 16.4$  W whereas  $t_{1/2}$  decreases from 57 ms to 7 ms. The sixth dataset exhibits a different behavior as expected since mirror  $M_1$  was damaged. The initial cavity gain corresponds to a cavity finesse of 18000 (see Table 5.2 and Section 5.2). Despite a careful mirror surface cleaning, this is significantly lower than the finesse measurement of 25000-28000 performed right after coating manufacturing<sup>[31]</sup>. Cavity mirrors were passed through a UV-air cleaner, carefully cleaned again and reinstalled after completing the experiments reported above. With  $M_1$  shifted by a few millimeters to avoid losses induced by the crater, we obtained a finesse of 23000. The finesse decrease observed here is then most likely due to a surface contamination.

It needs to be mentioned that we repeated twice the power rising experiment.  $P_{in}$  was kept below 20 W during the first experiment and data were only recorded during the second one. The data were similar in both experiments showing qualitatively the

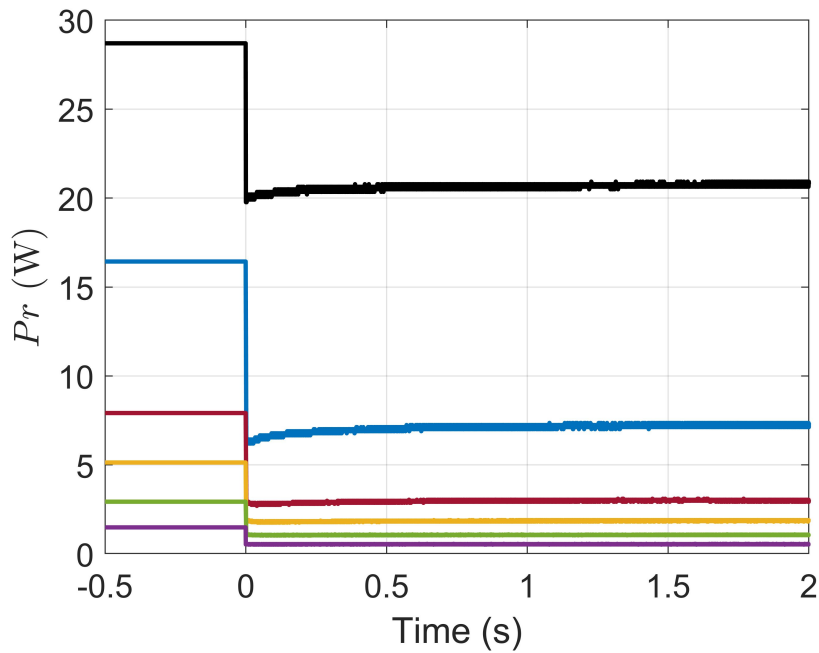


Figure 5.3 Experimental data of the SBOX cavity reflected average power  $P_r$  as a function of time for various values of injection laser beam average power  $P_{in}$ . The six datasets are shown, from the top to bottom:  $P_{in} = 28.7$  W (black), 16.4 W (blue), 7.9 W (red) 5.1 W (yellow), 2.9 W (green) and 1.5 W (purple).

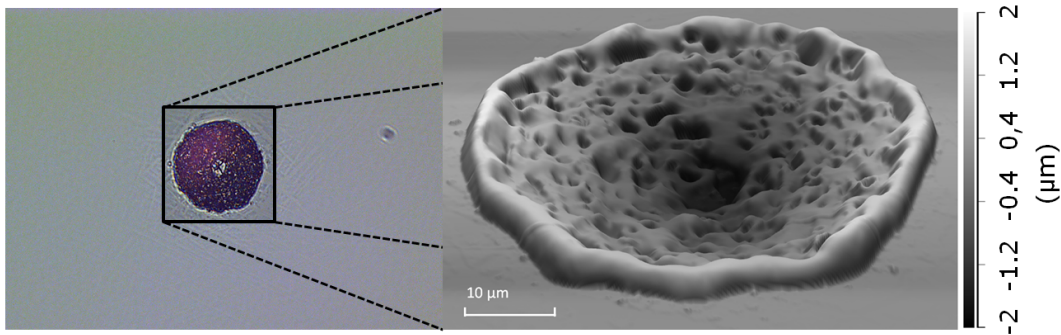


Figure 5.4 Left: optical microscope image of the damage area on surface of cavity mirror  $M_1$ . Right: 3D AFM image of crater. A crater with radius  $\sim 25 \mu m$  is positioned at the center of coupling mirror surface. A crack zone around the crater extends the damage area with radius up to  $\sim 100 \mu m$ .

repeatability of the phenomenon. For a given  $P_{in}$  value, magnitude of the power drops was also repeatable as shown in Fig. 5.5 where a sequence of locking-unlocking of the cavity was recorded.

Table 5.1 Characteristic values of six experimental datasets derived from the reflected and transmitted average power measurements.  $t = 0$  is defined as the instant when  $P_c$  reaches its maximum.  $P_{c,i}$  and  $P_{r,i}$  correspond to the values of  $P_c$  and  $P_r$  at  $t = 0$  respectively; the steady state values of  $P_{c,f}$  and  $P_{r,f}$  are defined by the average values of  $P_c$  and  $P_r$  over the time interval  $[1s, 2s]$ . The relative steady state average power drop  $\Delta = 1 - P_{c,f}/P_{c,i}$ . The characteristic half power drop time  $t_{1/2}$  is defined as the time it takes for  $P_c$  to drop from its maximum value down to  $(P_{c,i} + P_{c,f})/2$ . The cavity gain is estimated at  $t = 0$  by  $G_{c,i} = P_{c,i}/P_{in}$ .

$P_{in}$ (W)	1.5	2.9	5.1	7.9	16.4	28.7
$P_{c,i}$ (kW)	5.6	11.1	18.9	29.2	58.1	6.1
$P_{c,f}$ (kW)	5.4	9.9	15.5	20.6	31.6	5.7
$\Delta$ (%)	3.6	11	18	30	46	6
$P_{r,i}$ (W)	0.5	1.1	1.9	3.0	6.8	19.9
$P_{r,f}$ (W)	0.5	1.1	1.9	3.0	7.2	20.7
$t_{1/2}$ (ms)	57	41	25	15	7	60
$G_{c,i}$	3800	3800	3700	3700	3500	210

## 5.2 Modeling of Prior-damage Dynamics

Dedicated experiments have addressed mirror damage by implementing metallic contaminants on the mirror surface or inside the coating layers, see e.g. [95-96]. Here we have no a priori indication on the origin of mirror damage and, presumably to the prior-damage dynamics described in the previous Section We are thus providing a *post mortem* analysis. From an AFM study in contact mode operation of the crater (see Fig. 5.4) we derived no indication neither on the hot spot constituting matter nor on its depth position inside the mirror coating. We could only measure its dimensions and position which is located at the mirror center. We then restrict ourselves to finding the dominant physics process that drove the prior-damage dynamical behavior. Our goal is thus to obtain a qualitative description of the main features of Table 5.1. Namely the steady state drop  $\Delta$  as a function of  $P_{in}$  and the transient behavior of  $P_c$  and  $P_r$  described by  $t_{1/2}$  as a function of  $P_{in}$ .

Nonlinear coupling<sup>[97]</sup> and power absorption in the multilayer coating<sup>[98-99]</sup> may contribute to describe the observed power drop. The former physics process is most likely negligible with intra-cavity laser pulse width of 250 ps and energy below 200  $\mu\text{J}$  respectively. Time scale of nonlinear effects is also expected to be much shorter than the observed values of  $t_{1/2}$ . The later process induces local temperature increase and thermoelastic surface deformation. As we shall see below, if a portion of the mirror surface

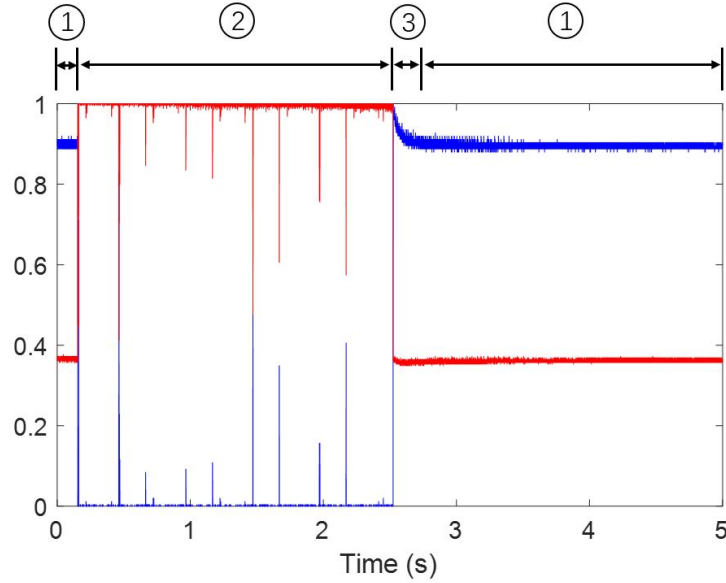


Figure 5.5 Normalized measurements of  $P_r$  (red) and  $P_c$  (blue) as a function of time for  $P_{in} = 2.9$  W. Region 1 and 2 correspond to the locked and unlocked cavity states respectively. Peaks in region 2 correspond to unlocked cavity resonances: the fundamental mode correspond to the higher peaks and the remaining higher order modes to the smaller peaks. Region 3 exhibits the transient power drop of the locked cavity.

is contaminated (chemically or with dust), a larger absorption of the intra-cavity average power may occur leading to locally high temperature increase. This leads to a thickness expansion and a shift of the optical indices of the mirror coating layers<sup>[100]</sup>. We estimated numerically the variation of the  $M_1$  coating transmission coefficient with two independent codes<sup>[101-102]</sup>. We assumed that the whole coating structure was at the same temperature that we chose to be  $400^\circ\text{C}$ , which corresponds to the maximum value observed during the simulations described in Section 5.3 as the temperature distribution on mirror surface shown in Fig. 5.6. As a result, we obtained a transmission decrease of  $\approx 14$  ppm with respect to the value of Table 4.1 meaning that, if this effect would be responsible for the phenomenon, we would observe a rising instead of a power drop. We further neglect it in our analysis since the level of this effect is small with regard to the expected induced losses. Nevertheless, a decrease of  $M_2$ 's transmission would also lead to a decrease of the signal measured by PD2 (see Fig. 5.2 and Fig. 5.2). One could thus underestimate the intra-cavity power measurement by not accounting for this effect. Beside, we didn't observed any hot-spot on  $M_2$ . We can thus assume that the heat source is solely related to the coating absorption for calculating the transmission decrease<sup>[101-102]</sup>. Taking  $P_c = 100$  kW, a decrease below 0.1 ppm was obtained<sup>[84,101-102]</sup>. We thus also neglect this effect.

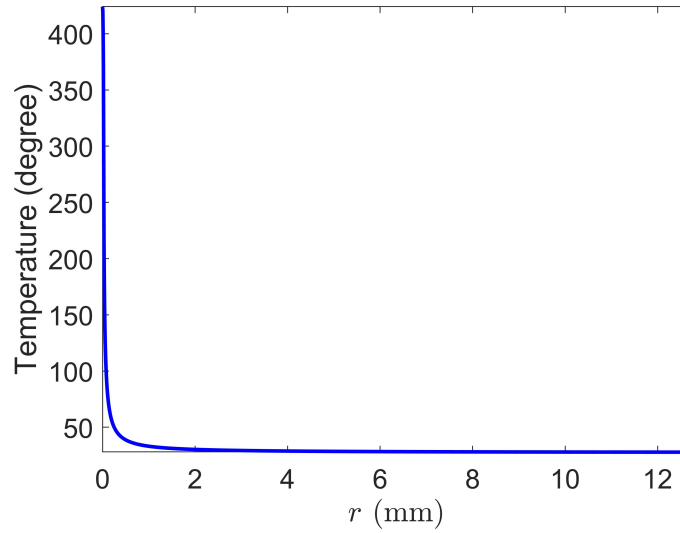


Figure 5.6 Temperature distribution on coupling mirror front surface calculated with ANSYS, with timing constant and spatially averaged heat of 0.05 W applied at hot spot region with radius of  $r_s = 25 \mu m$ , in which the properties of hot spot are more detailedly defined in Section 5.2.2.

### 5.2.1 Mirror Temperature Increase Characterized by Hello-Vinet Model

Transient thermal behavior of cavity coupling mirror induced by the heating of Gaussian laser beam with  $1/e^2$  radius of  $\sim 1$  mm is investigated with Hello-Vinet model<sup>[98-99]</sup>. Hello-Vinet model is a set of commonly used solution for describing the mirror thermoelastic behavior, including the steady and transient solution of mirror temperature and thermoelastic deformation distribution. In this section, only the temperature steady state and transient solutions<sup>[98]</sup> are revisited and used for characterization of the cavity mirror temperature increase behavior with the heating of Gaussian laser beam. The geometry used in Hello-Vinet model is shown in Fig. 5.7. The laser power to thermal power conversion and absorption is considered to be happened in the mirror coating and equivalently regarded as the mirror front surface since the thickness of coating is much smaller than thickness of mirror body. The steady state and transient temperature distribution in mirror could be derived with solving Fourier equation:

$$\rho C \frac{\partial T}{\partial t} - K \Delta T = 0, \quad (5-1)$$

in which density of silica  $\rho = 2202 \text{ kg/m}^3$ , specific heat  $C = 745 \text{ J/kg/K}$ , thermal conductivity  $K = 1.38 \text{ W/m/K}$ . The cavity mirrors are positioned in vacuum chamber,

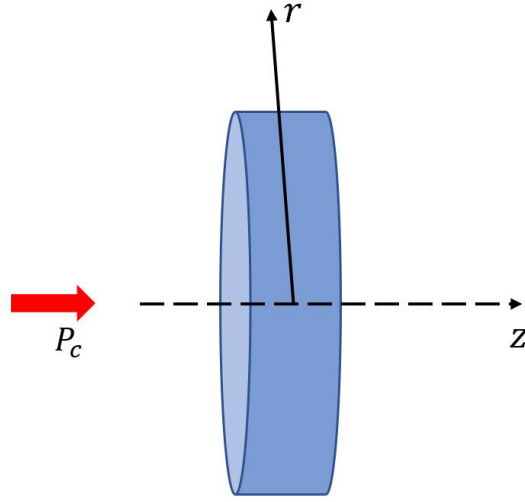


Figure 5.7 Illustrative plot of the geometry used in Hello-Vinet model. Cavity mirror is in a cylindrical structure with radius of  $a$  and thickness of  $h$ . The front and back mirror surfaces are positioned at planes  $z = -h/2$  and  $z = +h/2$  respectively. Laser beam of average power  $P_c$  is incidenting on the cavity mirror front surface.

so the only heat dissipation way is heat radiation

$$F = \sigma' (T^4 - T_{ext}^4), \quad (5-2)$$

where  $\sigma'$  is Stefan-Boltzman constant corrected for emissivity,  $T_{ext}$  is the environment temperature set to be  $22^\circ$ . With the low heating condition that the maximum temperature increase is much less than the environment temperature  $\frac{T_{max} - T_{ext}}{T_{ext}} \ll 1$ , the heat radiation could be linearized with respect to mirror temperature increase

$$F = \sigma' [T^4 - T_{ext}^4] \simeq 4\sigma' T_{ext}^3 \delta T. \quad (5-3)$$

Assume the steady-state solution can be written as

$$T(r, z) = T_{ext} + T_\infty(r, z). \quad (5-4)$$

Boundary conditions are:

$$\begin{aligned} -K \frac{\partial T_\infty}{\partial r}(a, z) &= 4\sigma' T_{ext}^3 T_\infty(a, z), \\ -K \frac{\partial T_\infty}{\partial z}\left(r, -\frac{h}{2}\right) &= AI(r) - 4\sigma' T_{ext}^3 T_\infty\left(r, -\frac{h}{2}\right), \\ -K \frac{\partial T_\infty}{\partial z}\left(r, +\frac{h}{2}\right) &= 4\sigma' T_{ext}^3 T_\infty\left(r, \frac{h}{2}\right), \end{aligned} \quad (5-5)$$

where  $A = 1 \text{ ppm}$  is the laser power to thermal power conversion and absorption coefficient. For steady state solution, it needs to be satisfied that

$$\Delta T_\infty(r, z) = 0. \quad (5-6)$$

A general solution of Eq. 5-6 can be expressed as

$$T_{\infty}(r, z) = \sum_m [A_m e^{k_m z} + B_m e^{-k_m z}] J_0(k_m r), \quad (5-7)$$

where the coefficients  $k_m, A_m, B_m$  could be determined from boundary conditions.  $k_m = \zeta_m/a$ , where  $\zeta_m$  is the  $m$ -th solution of equation  $xJ_1(x) - \tau J_0(x) = 0$ , with the reduced radiation constant defined as  $\tau = 4\sigma' T_{ext}^3 a/K$ . The intensity of laser beam with Gaussian distribution  $I(r) = \frac{2P_c}{\pi w^2} e^{-2r^2/w^2}$  needs to be discretized with Dini series  $I(r) = \sum_m p_m J_0\left(\zeta_m \frac{r}{a}\right)$  where coefficient  $p_m = \frac{P_c}{\pi a^2} \frac{\zeta_m^2}{(\zeta_m^2 + \tau^2) J_0(\zeta_m)^2} \exp\left[-\frac{1}{8} \zeta_m^2 \frac{w^2}{a^2}\right]$ . Then coefficients  $A_m, B_m$  can be found as

$$\begin{aligned} A_m &= \frac{\varepsilon p_m \alpha}{K} e^{-3\zeta_m h/2a} \frac{\zeta_m - \tau}{(\zeta_m + \tau)^2 - (\zeta_m - \tau)^2 e^{-2\zeta_m h/a}}, \\ B_m &= \frac{\zeta p_m \alpha}{K} e^{-\zeta_m h/2a} \frac{\zeta_m + \tau}{(\zeta_m + \tau)^2 - (\zeta_m - \tau)^2 e^{-2\zeta_m h/a}}. \end{aligned} \quad (5-8)$$

The steady state temperature distribution on mirror front surface calculated through Hello-Vinet model with laser beam heating of  $P_c = 50$  kW,  $w = 1$  mm is resulted as the blue curve shown in Fig. 5.8, compared with the result calculated with the same setting by ANSYS shown in red curve. A good consistency is achieved.

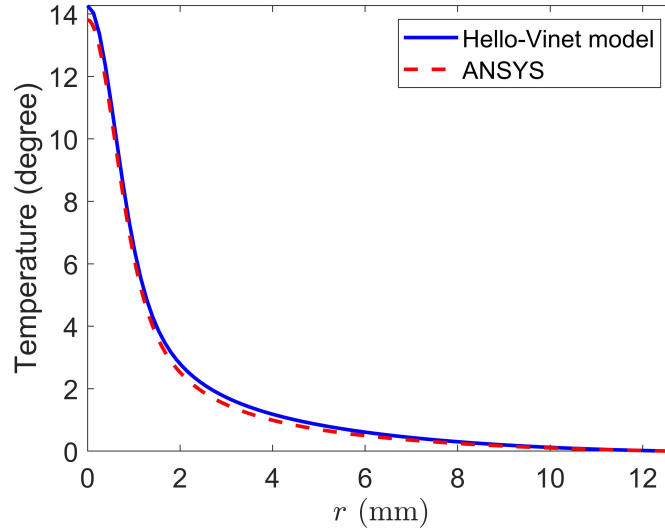


Figure 5.8 Steady state temperature distribution on coupling mirror  $M_1$  front surface calculated with Hello-Vinet model (blue) and ANSYS (red), with laser beam heating of  $P_c = 50$  kW,  $w = 1$  mm. Environment temperature of  $22^\circ$  has been subtracted.

Then we continue to transient solution of temperature distribution, which is assumed

in the form

$$T(t, r, z) = T_{ext} + T_{\infty}(r, z) + T_{tr}(t, r, z). \quad (5-9)$$

$T_{ext}$  is the steady state solution that has been represented above.  $T_{tr}$  is the solution of Eq. 5-1 and satisfy the boundary conditions:

$$\begin{aligned} -K \frac{\partial T_{tr}}{\partial r}(a, z) &= 4\sigma' T_{ext}^3 T_{tr}(a, z) \\ -K \frac{\partial T_{tr}}{\partial z}(r, \pm \frac{h}{2}) &= \pm 4\sigma' T_{ext}^3 T_{tr}(r, \pm \frac{h}{2}) \end{aligned} \quad (5-10)$$

The transient solution is

$$\begin{aligned} T_{tr}(t, r, z) &= \sum_{p,m} e^{-\alpha_{pm}t} A_{pm} \cos(u_p z/a) J_0(\zeta_m r/a) \\ &+ \sum_{p,m} e^{-\beta_{pm}t} B_{pm} \cos(v_p z/a) J_0(\zeta_m r/a), \end{aligned} \quad (5-11)$$

where the time constants are  $\alpha_{pm} = \frac{K}{\rho C a^2} [u_p^2 + \zeta_m^2]$ ,  $\beta_{pm} = \frac{K}{\rho C a^2} [v_p^2 + \zeta_m^2]$ . According to the time constants we define the characteristic time

$$t_c = \frac{\rho C a^2}{K}. \quad (5-12)$$

It can be used for estimation of the temperature rising time scale. For example for silica mirror  $t_c \simeq 191$  s. Coefficients  $u_p, v_p$  are respectively the p-th solution of equations  $u = \tau \cot \left[ \frac{uh}{2a} \right]$  and  $v = -\tau \tan \left[ \frac{vh}{2a} \right]$ . Coefficients  $A_m, B_m$  are then defined as

$$\begin{aligned} A_{pm} &= \frac{2}{hc_p} \int_{-h/2}^{h/2} \cos(u_p \frac{z}{a}) \theta_m(z) dz, \\ B_{pm} &= \frac{2}{hs_p} \int_{-h/2}^{h/2} \sin(v_p \frac{z}{a}) \theta_m(z) dz, \end{aligned} \quad (5-13)$$

with the normalization constants  $c_p = 1 - \frac{a}{v_p h} \sin(v_p h/a)$ ,  $s_p = 1 + \frac{a}{u_p h} \sin(u_p h/a)$  and  $\theta_m$  is corresponding to the coefficients in Dini series for expansion of  $T_{\infty}(r, z) = -\sum_m \theta_m(z) J_0(\zeta_m r/a)$ .

With the same setting of Gaussian laser beam heating with  $P_c = 50$  kW,  $w = 1$  mm, the transient maximum temperature of coupling mirror  $M_1$  is calculated by Hello-Vinet model as shown in Fig. 5.9. The maximum temperature is equivalently calculated at position of center of mirror front surface according to symmetry. The calculation speed is orders faster using Hello-Vinet model than ANSYS. The time step in transient calculation with ANSYS needs to be set as small enough ( $\sim 50 \mu s$ ) as the calculation of nonlinear

thermal process depends on former step result, while it is not the case for calculation with Hello-Vinet model since it has been linearized. The transient maximum temperature of mirror is only calculated for the first one hour time range, and the steady state is still not reached as shown in Fig. 5.9. The cavity temperature rising time defined as the time it takes for reaching the half of the steady state value is  $\sim 80$  s, which is close to the scale of characteristic time  $t_c \simeq 191$  s. So we see the time scale of the thermal effect induced by the 1 mm Gaussian laser beam is much larger than the intra-cavity power drop time scale with a few tens of milliseconds. The thermal effect induced by the 1 mm Gaussian laser beam is negligible during time of few tens of milliseconds when power drop phenomenon happens. From simulations, it came out that hot spots of radii between tens and hundreds of micrometers were the only possible heating source leading to a time scale evolution below 100 ms.

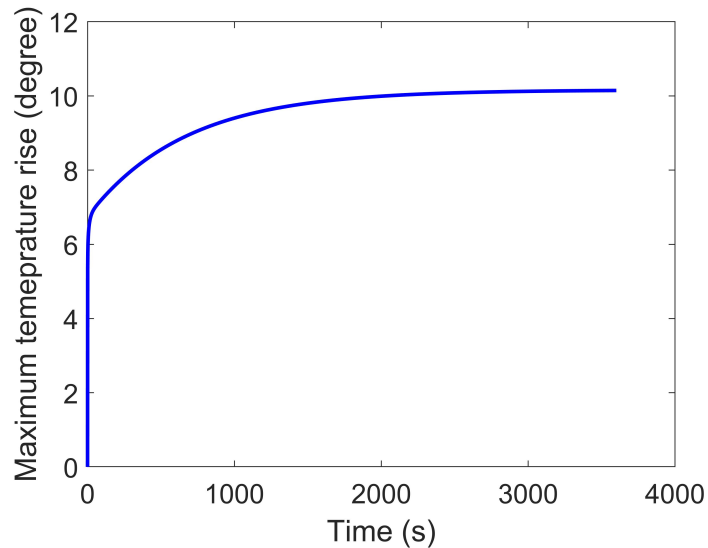


Figure 5.9 Maximum temperature rise of mirror body versus time calculated with Hello-Vinet model, using the parameters of 50 kW laser beam average power Gaussian distributed on mirror surface with  $1/e^2$  radius of 1 mm, laser power to thermal power conversion and absorption coefficient  $A = 1$  ppm.

### 5.2.2 Prior-damage Dynamics Induced by Hot Spot

Thermoelastic deformation induced by coating power absorption leads to surface bumps with heights depending on  $P_c$  [98-99]. These bumps become in turn a scattering source that populate higher-order cavity modes [103]. Losses to the higher order modes are finally induced by the D-shape mirrors [88]. This process can thus explain the observed power drops since higher the bump height, higher the scattering loss. Finally the time

scale  $t_{1/2}$  is a good quantity to identify the dominant heating source.

Therefore, we will assume here that a hot spot is the source of the phenomenon described in Section 5.1. For the sake of simplicity, we also assume that it consists in an homogeneous absorbing disc of radius  $r_s$  located close to the center of  $M_1$ 's surface. This model thus depends on six parameters, the hot spot radius  $r_s$ , the power absorption coefficient  $A$ , the hot spot position  $(d_x, d_y)$  with respect to the center of  $M_1$ 's surface, the D-shape mirrors' edge position  $(D_x, D_y)$  with respect to the center of  $M_2$ 's surface, see Fig. 5.10. To model the effect of the hot spot on the four-mirror cavity mode, we first use the ANSYS program for computing the thermoelastic deformations (in steady and transient states) of the  $M_1$  mirror. The cavity modes are further computed with the OSCAR program<sup>[85]</sup> in which deformed  $M_1$  surfaces and D-shape mirrors acting as a mask on  $M_2$ 's surface are implemented, see Fig. 5.10.

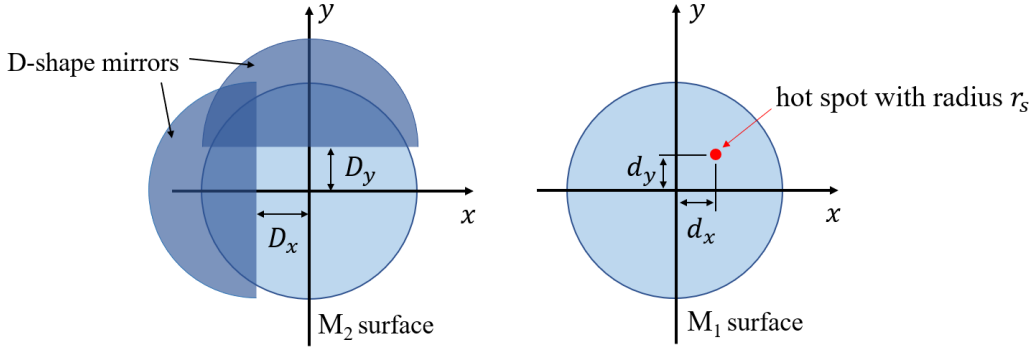


Figure 5.10 Schematic drawing of parameter definitions. A hot spot with radius  $r_s$  is positioned at  $(d_x, d_y)$  on the inner-cavity-side surface of coupling mirror  $M_1$ . D-shape mirrors' edges positioned at  $(D_x, D_y)$  with respect to the center of  $M_2$ 's surface.

To compare simulations and experimental results one must first relate power and cavity gain measurements of Table 5.1 to the round trip loss (RTL) determined by the OSCAR code. Extending the expression in Ref.<sup>[104]</sup> to the case of a four-mirror cavity and accounting for imperfect matching between injection laser beam and cavity mode, the following expressions hold

$$\begin{aligned} P_c &\approx |c_{00}|^2 \cdot \frac{4T_1}{RTL^2} P_{in}, \\ P_r &\approx \left( 1 - |c_{00}|^2 \frac{4T_1}{RTL^2} (RTL - T_1) \right) P_{in}, \end{aligned} \quad (5-14)$$

where high finesse limit<sup>[105]</sup> was also assumed. In these equations,  $|c_{00}|^2$  is coupling ratio of injection laser power to cavity<sup>[105]</sup>, it is assumed that the injection laser field is

composed of a laser field identical to cavity mode plus an orthogonal field, that is

$$\vec{E}_i(\vec{r}, t) = c_{00}\vec{E}_{00}(\vec{r}, t) + c_{mn}\vec{E}_{mn}(\vec{r}, t), \quad (5-15)$$

with the properties that  $|c_{00}|^2 + |c_{mn}|^2 = 1$ ,  $\int \vec{E}_{00}(\vec{r}, t)\vec{E}^*(\vec{r}, t)d\vec{r}dt = 0$ , in which  $\vec{E}_{00}(\vec{r}, t)$  is cavity mode field;  $T_1$  is the mirror  $M_1$  transmission and  $RTL$  is the round trip loss defined by  $RTL = 1 - \rho^2$  with  $\rho = r_1r_2r_3r_4$  where  $r_i$  stands for the electric field reflection coefficient of the  $i^{th}$  mirror. Rewriting Eq. 5-14 one gets

$$\begin{aligned} RTL &\approx T_1 + \frac{P_{in} - P_r}{P_c}, \\ |c_{00}|^2 &\approx \frac{P_c}{P_{in}} \cdot \frac{RTL^2}{4T_1}. \end{aligned} \quad (5-16)$$

$RTL$  and  $|c_{00}|^2$  are thus inferred from laser beam power measurements using  $T_1 = 180$  ppm and the cavity finesse is estimated using the formula  $\mathcal{F} \approx 2\pi/RTL$ <sup>[105]</sup>. Numerical values are shown in Table 5.2 for  $t = 0$  (with subscript "i") and steady state values calculated with averaging over the time interval [1s, 2s] (with subscript "f"). One can notice that our cavity is over coupled, that is  $RTL \neq 2T_1$ , unlike in the optimal optical coupling case. Parameter values extracted at  $t = 0$  are in agreement for all five datasets within 5 % accuracy. As for  $|c_{00}|^2$ , we get  $\approx 65$  %. This is consistent with the quality of the coupling of injection laser power to cavity achieved for these experiments (see Fig. 5.5).

Table 5.2 Round-trip losses, coupling ratios of injection laser power to cavity, and finesse inferred from the five sets of experimental data. Variables with subscript "i" are calculated at  $t = 0$ . Variables with subscript "f" are corresponding to steady state values calculated with averaging over the time interval [1s, 2s].

$P_{in}$ (W)	1.5	2.9	5.1	7.9	16.4
$RTL_i$ (ppm)	350	350	360	360	360
$RTL_f$ (ppm)	350	370	390	420	470
$ c_{00,i} ^2$ (%)	65	65	65	65	62
$ c_{00,f} ^2$ (%)	64	64	64	63	59
$\mathcal{F}_i$	18000	18000	18000	18000	18000
$\mathcal{F}_f$	18000	17000	16000	15000	13000

Analyzing the transient power drop regime one must also account for time response of the photodiode and electronic readout as well as cavity filling time. The former time scale is estimated by  $t_{readout} = RC \sim 60 \mu s$ , where the impedance  $R = 100 k\Omega$  is

dominated by an external resistor connected to the oscilloscope and  $C = 600 \text{ pF}$  is the sum capacitance of the photodiode and three-meter-long cable.  $t_{readout}$  is thus two orders of magnitude smaller than  $t_{1/2}$  values in Table 5.1, we will thus neglect it in our model. As for the characteristic cavity filling time, it is given by  $t_{fill} \approx 2/(f_{RT}RTL)^{[32]}$  for  $RTL \ll 1$  where  $f_{RT} = 133.33 \text{ MHz}$  is the cavity round trip frequency. Here we get  $t_{fill} \approx 45 \text{ }\mu\text{s}$ , so that the effect of cavity filling process will also be neglected in our model. We will thus assume that each point of Fig. 5.2 corresponds to a steady state of the cavity.

### 5.3 Simulation Results of Prior-damage Dynamics

The first step of the simulations is to find values of  $r_s$  and  $A$  that describe the steady state  $RTL_f$  measurements of Table 5.2. As mentioned above, we are lacking knowledge about the nature of the hot spot and we concentrate on what is most-likely the dominant process, that is scattering loss. Therefore, we choose not to perform a fit but rather to find, for fixed  $r_s$ , an interval for  $A$  that bounds the data. The other parameters were fixed to their nominal measured values  $d_x = d_y = 0$  and  $D_x = D_y = 3 \text{ mm}$ . For the OSCAR simulations, because of the unknown hot spot properties, the initial value of  $RTL$  is fixed to 350 ppm, that is the measured values of  $RTL_i$  in Table 5.2.

With the purpose of saving calculation time and memory, an axisymmetric 2D model as shown in Fig. 5.11 is used in ANSYS. A good consistency has been checked and shown between the axisymmetric 2D model and 3D model with mirror mount mechanical design file implemented into ANSYS. As the hot spot size is in the scale of tens to hundreds of micrometers which is much smaller than the whole mirror surface size and the mirror surface deformation induced by hot spot is much smaller than the whole mirror surface size, so the hot spot is always set to be positioned in the center of mirror inside ANSYS and the hot spot position could be moved in the following calculation in OSCAR code.

For the steady state calculation, first the ANSYS *Steady-State Thermal* simulation is run with the boundary condition including  $P_{c,f}$  times  $A=1 \text{ ppm}$  as a timing constant heat source applied at the hot spot area represented by a red line, and radiation with emissivity of 0.9 at all outer edges of mirror body which are represented as lines  $oa$ ,  $ab$ ,  $bc$  in Fig. 5.11. Environment temperature is set to be  $22^\circ$ . Simulation including also the  $1\text{mm}/e^2$  radius Gaussian laser beam has been done and came to the conclusion that the global

Gaussian beam heating effect is negligible, so for simulation simplicity the Gaussian laser beam heating is not applied. Perfectly insulated boundary condition at the symmetry axis  $oc$  is automatically set by ANSYS. The whole mirror body temperature distribution results from the *Steady-State Thermal* simulation are calculated then imported to *Static Structural* simulation. Besides, structural boundary condition is set as zero displacement of point  $b$  on  $z$  axis. Mirror surface deformation is calculated at line  $oa$  and for each hot spot radius  $r_s$  we find the normalized deformation have almost the same shape (difference less than 5%) and a coefficient  $p_1$  is fitted to represent the linear relation between the maximum deformation amplitude and the heat power absorbed at the red line area. For example for  $r_s = 175\mu\text{m}$ ,  $d_x = d_y = 0$ ,  $p_1 = 800\text{nm}/\text{W}$  and the normalized deformation is shown in Fig. 5.12.

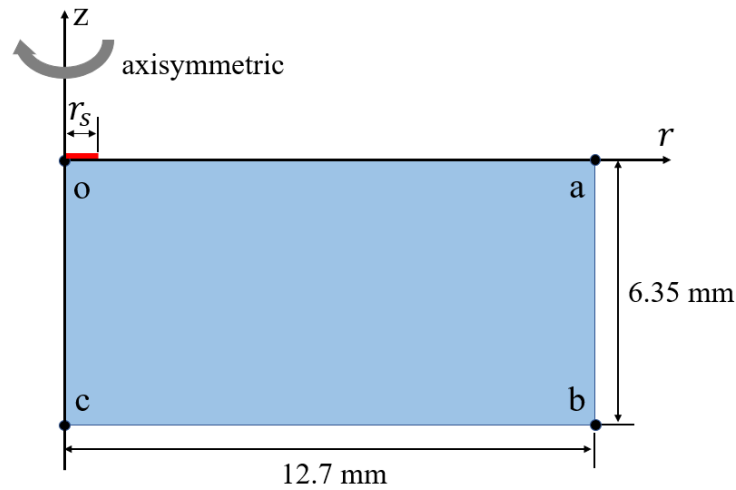


Figure 5.11 Schematic drawing of the axisymmetric 2D model used in ANSYS.

The thermoelastic deformation data are then implemented on surface of  $M_1$  inside OSCAR code to calculate the RTL. With OSCAR code, a four mirror cavity is generated with the SBOX parameters. We observed strong correlation between  $r_s$  and  $A$ . Table 5.3 gives a non-exhaustive set of values for these parameters that equally describe the data.  $A_+$  and  $A_-$  are the two values of  $A$  that give the upper and lower bound respectively of the  $RTL_f$  measurements. To pin down the origin of the correlation observed in Table 5.3, a few surface deformations calculated with the ANSYS code are shown in Fig. 5.13. For a fixed absorbed power, two hot spot sizes and a Gaussian beam of radius 1 mm are considered. For given  $A$  and  $P_c$  values, smaller the  $r_s$ , higher the thermoelastic deformation bump. Since the bump heights depend on the absorbed power, a larger value of  $A$  can thus compensate a larger value of  $r_s$ . Fig. 5.14 shows a comparison between experimental

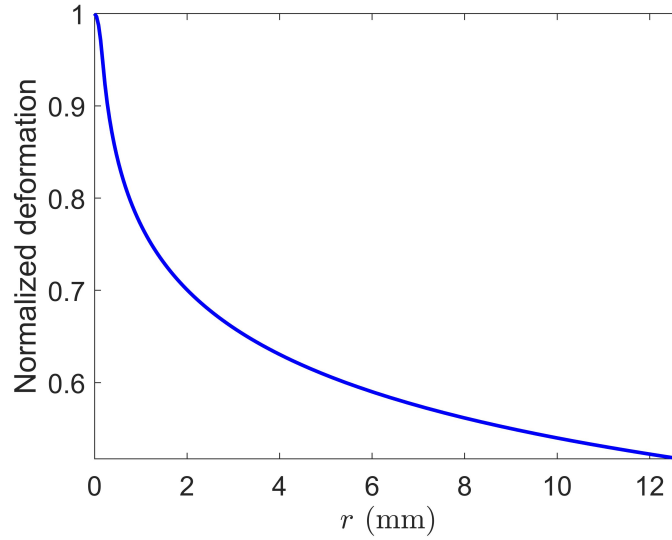


Figure 5.12 Normalized steady state  $M_1$  surface deformation with hot spot  $r_s = 175 \mu\text{m}$  positioned at center of  $M_1$ .

data and the simulation for  $r_s = 175 \mu\text{m}$ . The space between the curves corresponding to  $A_+$  and  $A_-$  has been colored for the sake of clarity. This plot shows that steady state data are qualitatively well described by our basic model for reasonable parameters values.

Table 5.3 Sets of  $A$  values that bound  $RTL_f$  for fixed  $r_s$ .

$r_s$ ( $\mu\text{m}$ )	$A_-$ (ppm)	$A_+$ (ppm)
25	2	2.8
100	2.3	3.3
150	2.6	4
175	2.9	4.5
200	3.2	5

The second step of the simulation aims at describing the time dependence of the observed intra-cavity power drops, *i.e.*  $P_c(t)$ . We will try to identify if a set of  $r_s$  and its related  $A$  values of Table 5.3 allows for a qualitative description of the measured  $t_{1/2}$ . We thus proceeded as follows. For fixed  $P_{in}$  we smoothed the measurements of  $P_c(t)$  and then sampled them by steps of 0.5 ms. Then we used the time dependence boundary condition mode of the ANSYS code to compute, step by step, the transient thermoelastic deformations as exemplarily shown in Fig. 5.15. Unlike for what we observed with steady state calculations, the height of the thermoelastic deformation determined by ANSYS doesn't scale linearly with the "instantaneous" power  $P_c(t)$ . Finally we used the resulting transient  $M_1$  surface deformations (sampled by steps of 0.5 ms) to compute the resulting  $RTL$

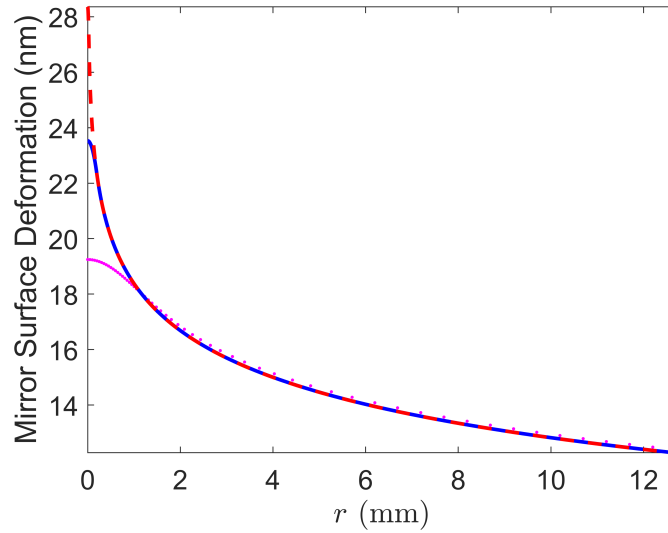


Figure 5.13 Steady state surface deformation computed with the ANSYS code as a function of the distance from the mirror center  $r$ . The absorbed power is fixed to be 0.03 W for: a Gaussian beam of  $1/e^2$  radius 1 mm (dotted magenta curve), hot spot of radius 200  $\mu\text{m}$  (blue full curve) and 25  $\mu\text{m}$  (dashed red curve).

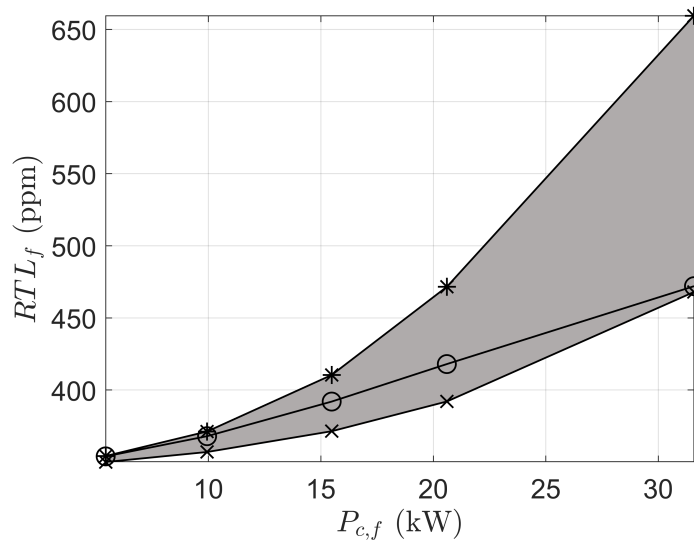


Figure 5.14 With simulation parameters of  $r_s = 175 \mu\text{m}$ ,  $D_x = D_y = 3 \text{ mm}$ ,  $A_- = 2.9 \text{ ppm}$  (crosses) and  $A_+ = 4.5 \text{ ppm}$  (stars), comparison between measured (circles) and simulated (crosses and stars)  $RTL_f$  values as a function of  $P_{c,f}$ .

with the OSCAR code. From this procedure we end up with a set of simulation values for  $P_c(t)$ . As a result, we could obtain a reasonable qualitative description of our data with  $r_s = 175 \mu\text{m}$ . Figs. 5.16 and 5.17 show the comparison between simulation and measurements of the intra-cavity and reflected power. For fixed  $P_{in}$ , the areas between the simulations made with  $A_- = 2.9 \text{ ppm}$  and  $A_+ = 4.5 \text{ ppm}$  have been colored. The

time variations around  $t = 0$  for all  $P_{in}$  values are well described. The overall qualitative agreement observed on these figures confirms that scattering losses of surface bump induced by a hot spot is most likely the main physics process responsible for the intra-cavity power drops.

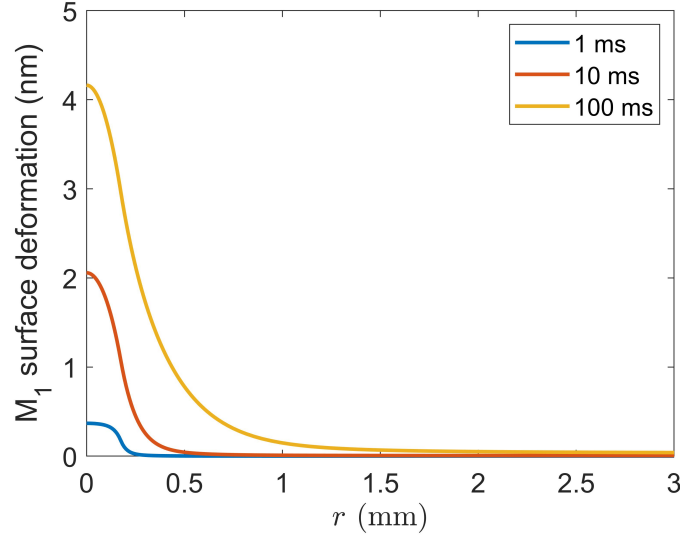


Figure 5.15 Transient  $M_1$  surface deformation with 1 ppm absorption of smoothed experimental data of  $P_c$  corresponding to  $P_{in} = 16.4$  W applied at hot spot area with  $r_s = 175 \mu\text{m}$ . Hot spot is positioned at center of  $M_1$ .

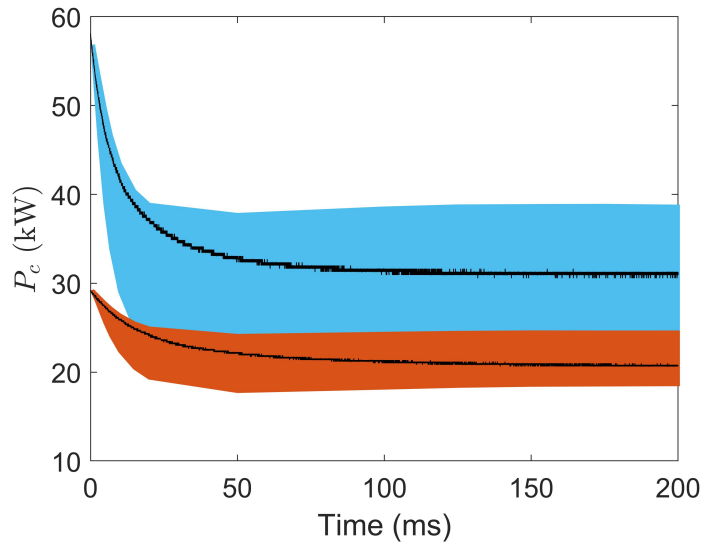
However the value  $r_s = 175 \mu\text{m}$  derived from our simulations doesn't correspond to the measured crater radius of  $25 \mu\text{m}$  (see Fig. 5.4). Since this measurement was performed in a cold mode, the damage area may differ from the one that is considered in our hot-spot model. From the left plot of Fig. 5.4 one indeed sees a crack zone around the crater that extends the radius of the damage area up to  $\approx 100 \mu\text{m}$ . In addition, crude assumptions have been made on the hot-spot nature in our model. The coating layer material<sup>[106]</sup>, the shape and the surface bond may indeed influence the shape of thermoelastic deformations.

Considering the observed coupling mirror damage area of radius  $25 \mu\text{m}$  and the precision of  $D_x, D_y$  measurement by ruler with precision of millimeter, experimental data compared with simulation results with the set of parameters of  $r_s = 25 \mu\text{m}, D_x = D_y = 2.5$  mm are presented in Fig. 5.18, Fig. 5.19 and Fig. 5.20, in which the trend of power drop can also be reproduced.

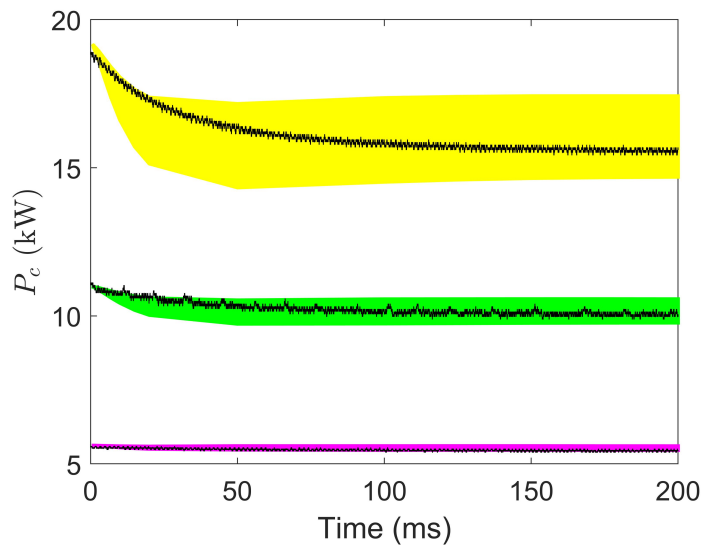
After inspection of the coupling mirror damage as shown in Fig. 5.4, an experiment was launched with coupling mirror  $M_1$  moved about 2 mm off the original center aiming for avoiding the damaged area. As it shown in Fig. 5.21 the mode is distorted with a high intensity spot marked with a red circle. Limited to the one inch mirror diameter, the

damage area is unavoidable. So the damaged mirror could not be used in experiments anymore. The analysis presented in this section could help to understand what happens inside OEC when this phenomenon appears and could help prevent permanent damage of the state of art ion beam sputtering technique coated mirrors used in high power OEC for wide range of applications.

The phenomenon described in this chapter occurred for moderate intra-cavity average power of the order of tens of kilowatts. However, the primary purpose of the experiments was trying to pin down the source of cavity gain decrease for intra-cavity stored average power around hundreds of kilowatts<sup>[58,88]</sup>. This issue has also been reported<sup>[58]</sup> with 200-fs short pulses<sup>[107]</sup> and for cavities in which optical components were inserted<sup>[108-109]</sup>. This issue is then still open and should be addressed in advance of future needs for intra-cavity average power at the megawatt level.



(a)



(b)

Figure 5.16 With simulation parameters of  $r_s = 175 \mu\text{m}$ ,  $D_x = D_y = 3 \text{ mm}$ ,  $A_- = 3 \text{ ppm}$  and  $A_+ = 4.5 \text{ ppm}$ , comparison between measurements and simulations of  $P_c$  as a function of time for various values of  $P_{in}$ : (a)  $P_{in} = 16.4 \text{ W}$  (top) and  $7.9 \text{ W}$  (bottom); (b) from top to bottom,  $P_{in} = 5.1 \text{ W}$ ,  $2.9 \text{ W}$  and  $1.5 \text{ W}$ . Color bands are the simulation results and black curves are the experimental points. Simulations and measurements are on the top of each other for the last dataset.

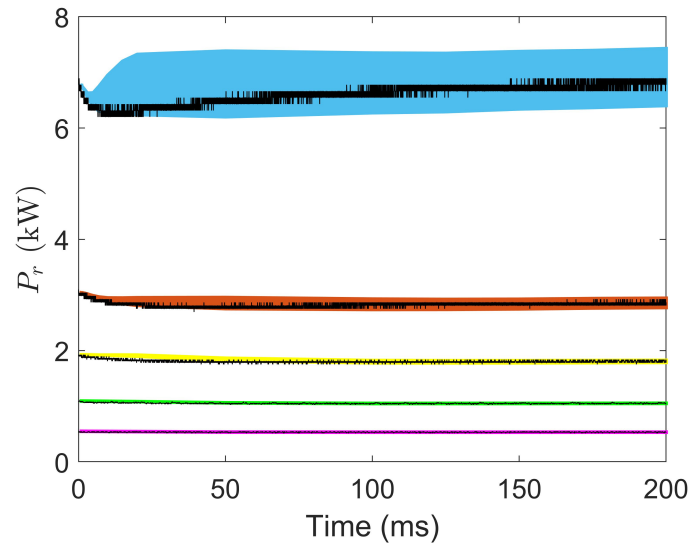


Figure 5.17 With simulation parameters of  $r_s = 175 \mu\text{m}$ ,  $D_x = D_y = 3 \text{ mm}$ ,  $A_- = 3 \text{ ppm}$  and  $A_+ = 4.5 \text{ ppm}$ , comparison between measurements and simulations of  $P_r$  as a function of time for various values of  $P_{in}$ . Color bands are the simulation results and black curves are the experimental points. The following datasets are shown, from top to bottom:  $P_{in}=16.4 \text{ W}$  (blue),  $7.9 \text{ W}$  (red),  $5.1 \text{ W}$  (yellow),  $2.9 \text{ W}$  (green) and  $1.5 \text{ W}$  (purple). Simulations and measurements are on the top of each other for the three latter datasets.

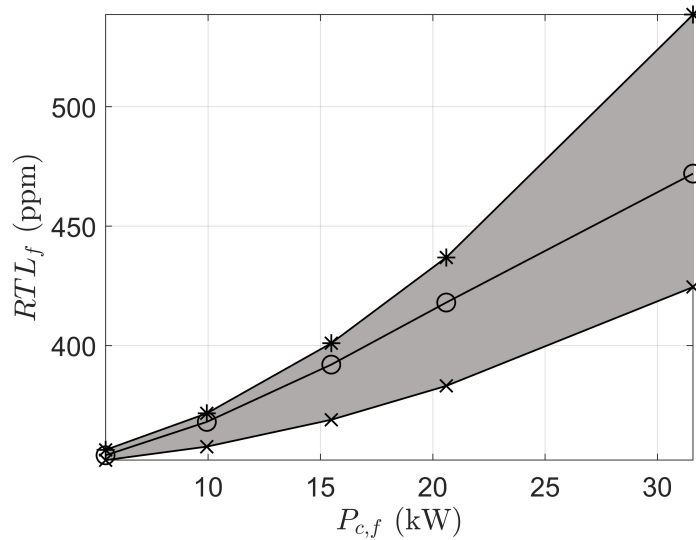
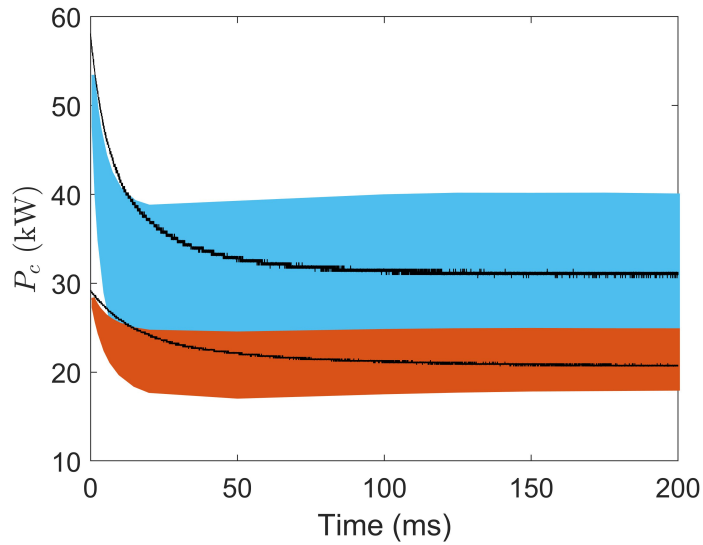
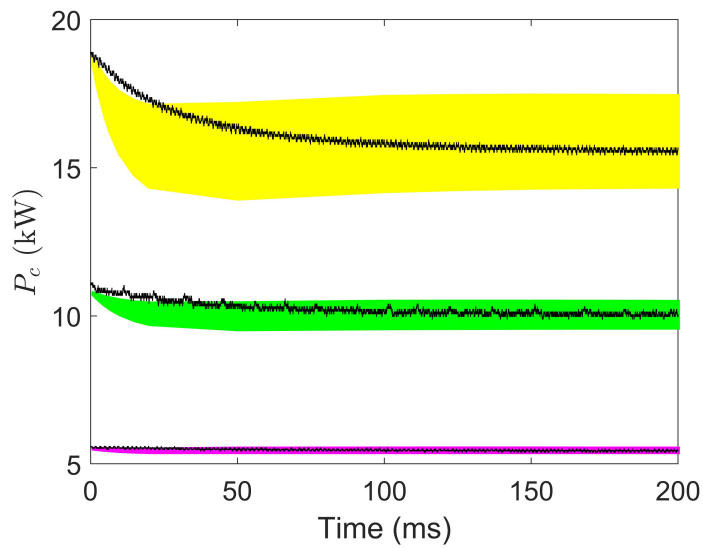


Figure 5.18 With simulation parameters of  $r_s = 25 \mu\text{m}$ ,  $D_x = D_y = 2.5 \text{ mm}$ ,  $A_- = 1.5 \text{ ppm}$  (crosses) and  $A_+ = 2.5 \text{ ppm}$  (stars), comparison between measured (circles) and simulated (crosses and stars)  $RTL_f$  values as a function of  $P_{c,f}$ .



(a)



(b)

Figure 5.19 With simulation parameters of  $r_s = 25 \mu\text{m}$ ,  $D_x = D_y = 2.5 \text{ mm}$ ,  $A_- = 1.5 \text{ ppm}$  and  $A_+ = 2.5 \text{ ppm}$ , comparison between measurements and simulations of  $P_c$  as a function of time for various values of  $P_{in}$ : (a)  $P_{in} = 16.4 \text{ W}$  (top) and  $7.9 \text{ W}$  (bottom); (b) from top to bottom,  $P_{in} = 5.1 \text{ W}$ ,  $2.9 \text{ W}$  and  $1.5 \text{ W}$ . Color bands are the simulation results and black curves are the experimental points. Simulations and measurements are on the top of each other for the last dataset.

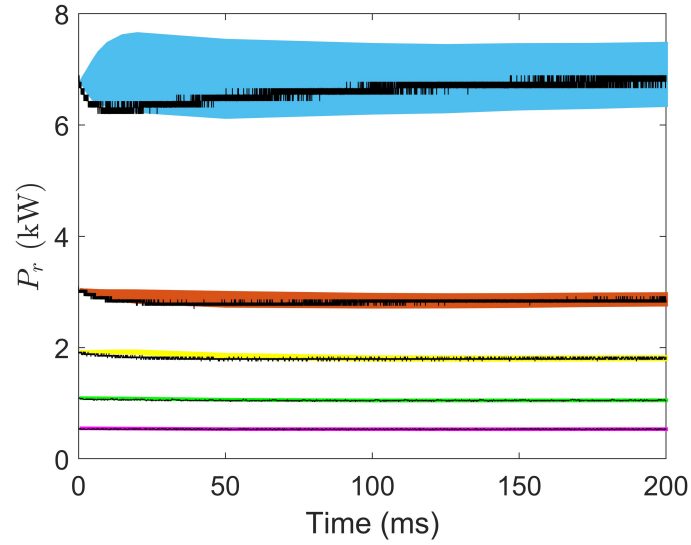


Figure 5.20 With simulation parameters of  $r_s = 25 \mu\text{m}$ ,  $D_x = D_y = 2.5 \text{ mm}$ ,  $A_- = 1.5 \text{ ppm}$  and  $A_+ = 2.5 \text{ ppm}$ , comparison between measurements and simulations of  $P_r$  as a function of time for various values of  $P_{in}$ . Color bands are the simulation results and black curves are the experimental points. The following datasets are shown, from top to bottom:  $P_{in}=16.4 \text{ W}$  (blue),  $7.9 \text{ W}$  (red),  $5.1 \text{ W}$  (yellow),  $2.9 \text{ W}$  (green) and  $1.5 \text{ W}$  (purple). Simulations and measurements are on the top of each other for the three latter datasets.

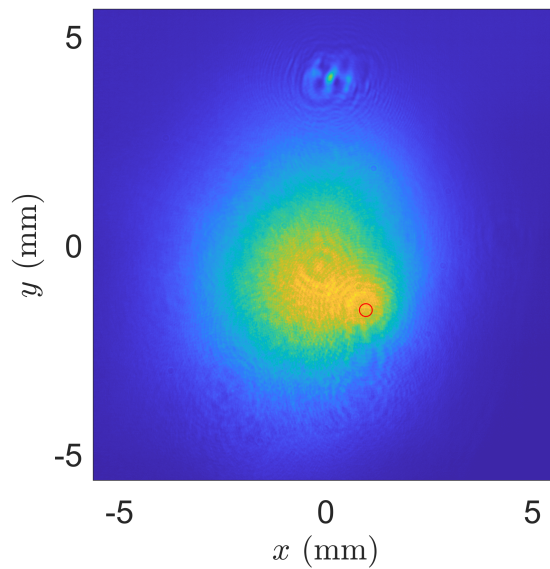


Figure 5.21 With the coupling mirror damaged as shown in Fig. 5.4, cavity mode with coupling mirror moved off the original center. Red circle marks a high intensity spot.

## Chapter 6 Study on Optical Enhancement Cavity of TTX

Currently, Tsinghua Thomson scattering X-ray source (TTX) is capable of producing X-rays via scattering between electron beams from linac with laser beams from terawatt laser system<sup>[22]</sup>. The yield of X-rays reaches  $\sim 10^6$  photons per pulse with a repetition rate of 10 Hz, which couldn't satisfy the need of some applications demanding for high average flux.

To improve the average flux of X-rays, TTX is planning to be upgraded to configuration combining optical enhancement cavity (OEC)<sup>[33][34]</sup> and electron storage ring<sup>[35][36]</sup>. Before the development of the OEC for combining with electron storage ring, R&D works need to be done on prototype OEC of TTX which is called TBOX. The prototype TBOX is independent from electron storage ring to realize the design goals demanded for OEC itself. The goals include a laser beam waist with radius size of few tens of micrometers inside OEC, intra-cavity laser pulse length of  $\sim 10$  ps with repetition rate of few tens of MHz, and an hour-time-scale stable intra-cavity average power of few hundreds of kilowatts. Previously, part of the design works for prototype OEC of TTX have been done as shown in Ref.<sup>[33][34]</sup>, but no experimental work has been done.

In this chapter, the full design of the experimental setup of TBOX and the preliminary experiments carried out on it will be presented in Section 6.1. The goal of the preliminary experiment is to lock a continuous wave injection laser with the 3.78 m round-trip-length Fabry-Perot cavity using PDH method<sup>[62-63]</sup>. Finesse and gain of the preliminary TBOX are measured to be  $\sim 1610$  and 133 respectively. The pathroute for future development of the OEC until final realization of combining OEC with electron storage ring to produce high average flux X-rays is planned. The design of the high power TBOX setup to realize few hundreds of kilowatts average power inside is presented in Section 6.2. The design of the final OEC which will be combined with electron storage ring is presented in Section 6.3.

## 6.1 Preliminary Experiments on TBOX

### 6.1.1 Preliminary Experimental Setup of TBOX

Prototype optical enhancement cavity (OEC) of TTX, called TBOX, of which the preliminary experimental setup is schematically shown in Fig. 6.1. The OEC is in a four-mirror planar bow-tie structure with a round trip length of  $\sim 3.78$  m as shown more detailedly in Fig. 6.2. Distances  $L_1, L_2, L_3, L_4$  are designed to be [882, 947, 1006, 947] mm,  $d = 80$  mm. Incidence angle on  $M_2$  is  $\theta = \alpha/2 = 2.422^\circ$ . Cavity mirrors  $M_1$  and  $M_2$  are planar mirrors,  $M_3$  and  $M_4$  are concave mirrors with radius of curvature of 1 m. TBOX is injected with laser of central wavelength 1064 nm. The intra-cavity laser beam size evolution on tangential and sagittal axes are calculated and shown in Fig. 6.3. A laser beam waist with radius size of  $102 \mu\text{m}$  on tangential axis and  $95 \mu\text{m}$  on sagittal axis is designed to be positioned in the middle between  $M_3$  and  $M_4$ .

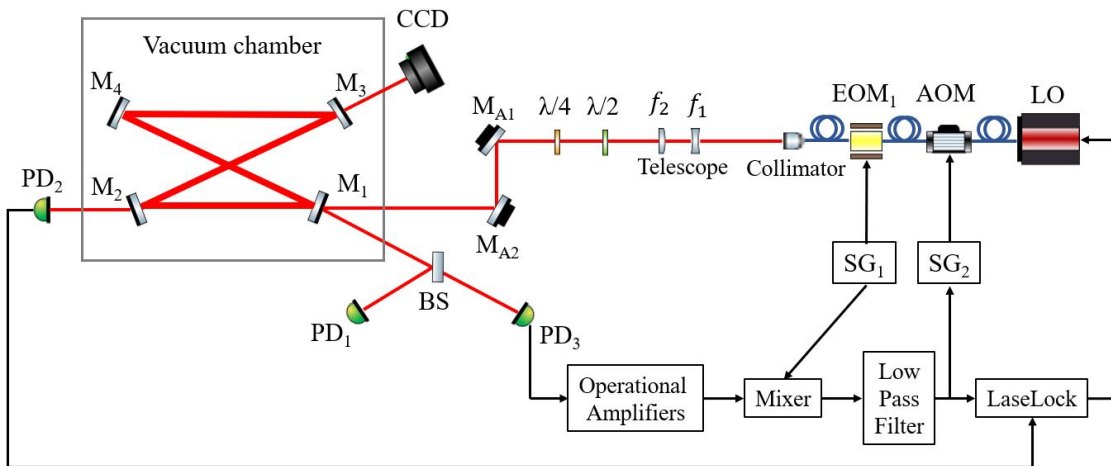


Figure 6.1 Preliminary experimental setup of TBOX. LO: laser oscillator. AOM: acousto-optic modulator. EOM: electro-optic modulator. BS: beam splitter. PD: photodiode. CCD: camera. SG: signal generator.

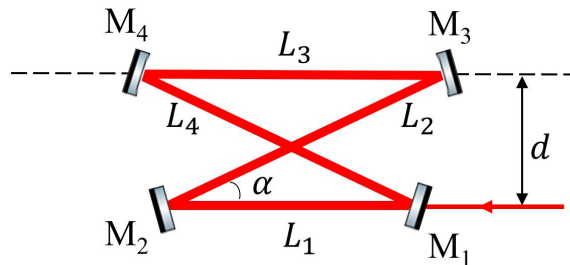


Figure 6.2 Preliminary TBOX is in a four-mirror planar bow-tie structure. Distances  $L_1, L_2, L_3, L_4$  are [882, 947, 1006, 947] mm,  $d = 80$  mm. Incidence angle on  $M_2$  is  $\theta = \alpha/2 = 2.422^\circ$ .

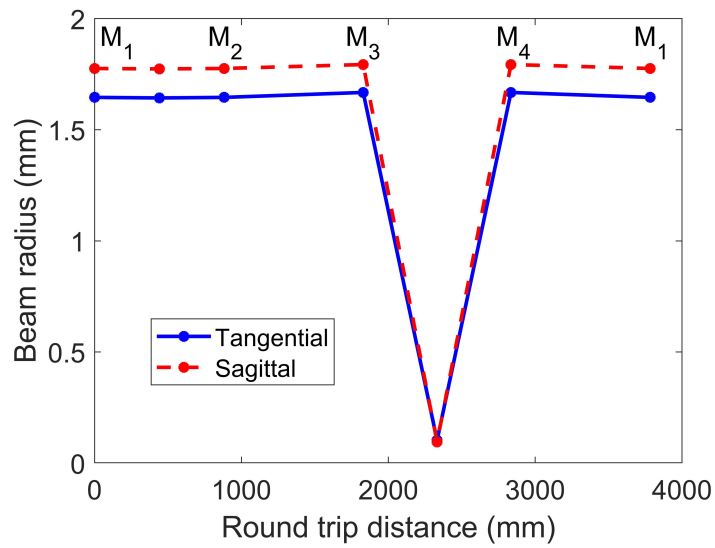


Figure 6.3 Laser beam radius size change inside preliminary TBOX on tangential (blue) and sagittal (red) axes with respect to the round trip distance from  $M_1$ . The texts " $M_1$ ,  $M_2$ ,  $M_3$ ,  $M_4$ " mark the corresponding cavity mirror positions. A laser beam waist with radius size of  $102 \mu\text{m}$  on tangential axis and  $95 \mu\text{m}$  on sagittal axis exists in the middle position between cavity mirror  $M_3$  and  $M_4$ .

Structure of two-mirror cavity is not chosen<sup>[110]</sup> for it will be highly unstable with a concentric configuration to have a small laser beam waist of few tens of micrometers inside which is needed by Thomson scattering. Besides, for four-mirror cavity compared with two-mirror cavity, tuning of the cavity round trip length could be decoupled from tuning the intra-cavity laser beam waist size, as the former one could be tuned with changing  $L_1$  by moving cavity mirror  $M_1$  or  $M_2$  and the latter one could be tuned with changing  $L_3$  by moving cavity mirror  $M_3$  or  $M_4$ . With the other distances kept as the same, the laser beam waist radius versus  $L_1$  and  $L_3$  are show in Fig. 6.4 and Fig. 6.5 respectively.

The spatial size parameters of the prototype cavity are chosen to be close to the final design of the OEC which will be combined with electron storage ring with a circumference of 5.668 m whose layout is shown in Fig. 6.6. The cavity length corresponds to a free spectral range (FSR) of 79.3 MHz, which is an harmonic of the 2856 MHz accelerating microwave frequency of S-band linac, so to match the repetition rate of laser beams and electron beams for Thomson scattering.

All four cavity mirrors are commercial products from Layertec GmbH with one inch diameter, the key parameters of which are summarized in Table 6.1. Cavity mirrors are highly reflective for laser with central wavelength of 1064 nm, with consideration for future high power OEC experiment the most commonly available high-average-power

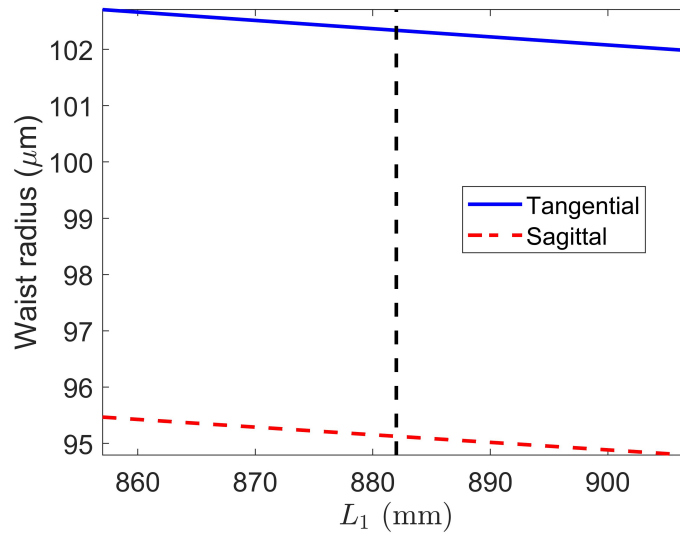


Figure 6.4 For prototype optical enhancement cavity TBOX, relation of intra-cavity laser beam waist radius versus  $L_1$  the distance between cavity mirror  $M_1$  and  $M_2$ , when distances between other mirrors are fixed. Black dashed line indicates the condition of TBOX where  $L_1 = 882$  mm. Tuning of cavity round trip length could be realized by changing  $L_1$  without varying much the intra-cavity laser beam waist size.

and high-repetition-rate laser are Yb: fiber lasers with wavelength around  $1 \mu\text{m}$ . Precise values of cavity mirror transmissions are calibrated after receiving the mirrors with power meter (Gentec PH100-Si-HA-OD1-D0). As lacking information of the cavity mirrors' absorption losses and scattering losses, considering only the cavity mirrors' noncomplete reflections, the ideal cavity linewidth, finesse and gain are calculated to be 20 kHz,  $\sim 3830$  and  $\sim 1060$  respectively by Eq. 2-11 and Eq. 2-12. Furthermore, with transmission  $T_2$ ,  $T_3$ ,  $T_4$  fixed and neglecting all other intra-cavity power losses, in Fig. 6.7 the blue and red curves correspondingly show the cavity finesse and gain versus the varying  $T_1$ , in which the black dashed lines indicate the condition of TBOX where  $T_1 = 712$  ppm. From Fig. 6.7 we can see that TBOX works at a condition close to the maximum gain position with impedance matching realized.

Four cavity mirrors are mounted inside a vacuum chamber as the mechanical design shown in Fig. 6.8<sup>[34]</sup>. The vacuum chamber is evacuated by dry pump (Leybold SCROLLVAC 15 plus) to  $10^{-2}$  mbar residual pressure. This primary vacuum helps to mitigate the transmission of vibrational noise through air thus helps to realize the lock between injection laser and cavity. The photo of the whole TBOX experimental setup is shown in Fig. 6.9.

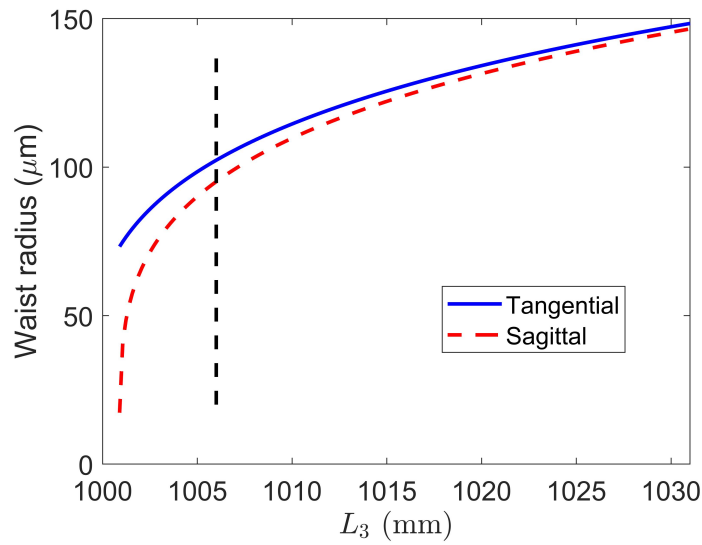


Figure 6.5 For prototype optical enhancement cavity TBOX, relation of intra-cavity laser beam waist radius versus  $L_3$  the distance between cavity mirror  $M_3$  and  $M_4$ , when distances between other mirrors are fixed. Black dashed line indicates the condition of TBOX where  $L_3 = 1006$  mm. Tuning of intra-cavity laser beam waist size could be realized by changing  $L_3$ .

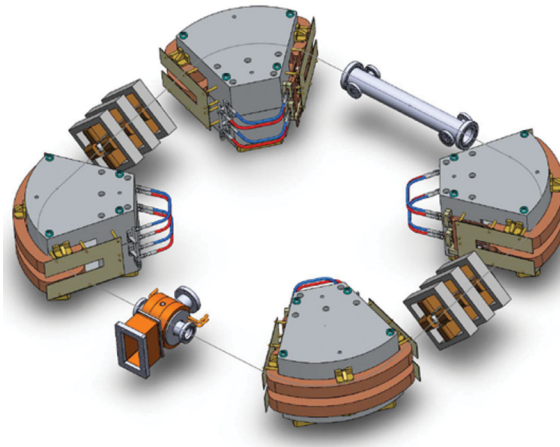


Figure 6.6 Layout of electron storage ring of TTX with circumference of 5.668 m<sup>[36]</sup>.

### 6.1.2 Locking a Continuous Wave Injection Laser with TBOX

Although pulsed wave (PW) laser beams stacked inside OEC are needed by Thomson scattering, a proper start of the experiment is to lock the cavity with a continuous wave (CW) laser. Because for the final goal of locking PW laser with cavity, the repetition rate of PW laser needs to be tuned to be consistent with the cavity FSR. So the FSR of OEC should firstly measured by EOM-based frequency scan<sup>[111]</sup> with locking of CW laser, thus to determine which direction to tune the repetition rate of PW laser. When the needed change of repetition rate is out of the tuning range of the PW laser, cavity mirror

Table 6.1 Key parameters of preliminary TBOX cavity mirrors. *Transmission calibrated* shows mirror transmission coefficients calculated from the measurement made after receiving the mirrors. *Reflectance in datasheet* shows the information about mirror reflectivity provided by Layertec GmbH.

Mirror	Type	Substrate material	Transmission calibrated (ppm)	Reflectance in datasheet
M <sub>1</sub>	Planar	Fused silica	712	>99.8%
M <sub>2</sub>	Planar	Fused silica	782	>99.95%
M <sub>3</sub>	Concave	Fused silica	75	>99.9%
M <sub>4</sub>	Concave	Fused silica	72	>99.9%

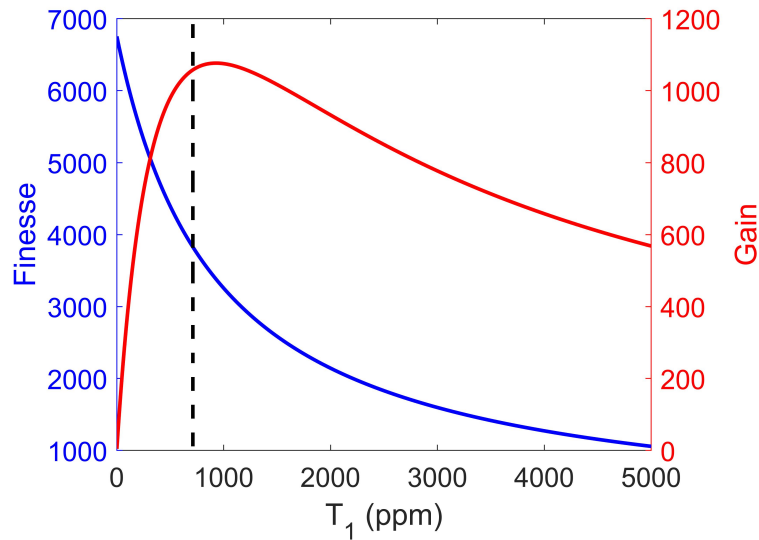


Figure 6.7 For preliminary TBOX, with transmission of cavity mirrors M<sub>2</sub>, M<sub>3</sub>, M<sub>4</sub> fixed to the values shown in Table 6.1 and neglecting all other intra-cavity power losses, the ideal cavity finesse (blue) and cavity gain (red) versus transmission T<sub>1</sub> of cavity mirror M<sub>1</sub> are calculated by Eq. 2-11. The black dashed line indicates the condition of TBOX where T<sub>1</sub> = 712 ppm with cavity finesse of ~ 3830 and cavity gain of ~ 1060, which is close to the maximum gain condition with impedance matching realized.

position should be moved to change the cavity FSR, after which the cavity FSR needs to be remeasured by EOM-based frequency scan with locking of CW laser. In addition, locking of CW laser with cavity is a rather easier process to check the feasibility of the system without the additional requirements to tune the repetition rate or carrier-envelope phase (CEP) of PW injection laser. So it is necessary to lock CW laser with OEC to begin the experiment. Koheras from NKT Photonics, a commercial product CW fiber laser oscillator with a central wavelength of 1064 nm and linewidth of 3 kHz is used as the cavity injection laser. The output power of Koheras is up to ~100 mW.

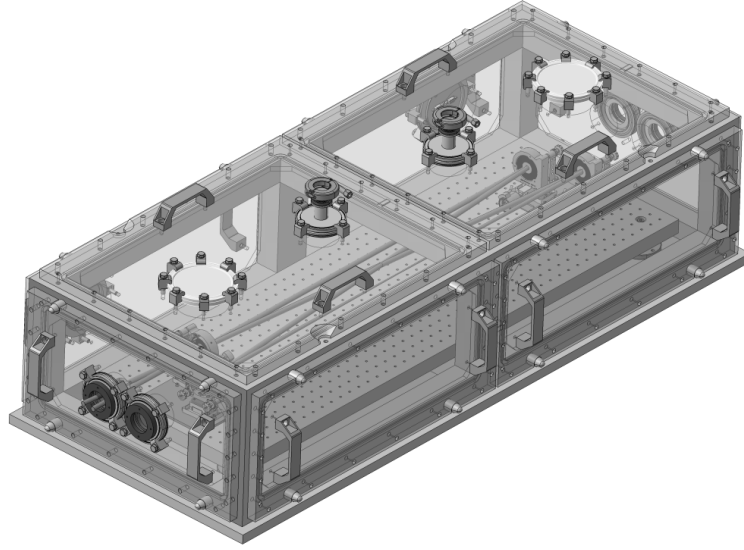


Figure 6.8 Mechanical design of the vacuum chamber of preliminary TBOX<sup>[34]</sup>.



Figure 6.9 Photo of TBOX setup for preliminary experiment.

Telescope made up of one concave lens  $f_1$  and one convex lens  $f_2$  are configured to tune the injection laser beam size and divergence angle to match with that of the cavity mode. A collimator (Thorlabs TC12APC-1064) is used to collimate the laser beam from fiber to free space. The laser beam size at 20 mm after collimator is measured to be with  $1/e^2$  Gaussian fitted radius size of 0.95 mm. The telescope is designed with ABCD matrix to match the injection laser beam size and divergence angle with that of the cavity mode in the middle of  $M_1$  and  $M_2$ . As a result, a concave lens  $f_1$  with focal length of -150 mm positioned at 253 mm after the collimator and a convex lens  $f_2$  with focal length of +250 mm positioned at 102 mm after  $f_1$  are chosen to make up the telescope. The laser

beam size evolution from collimator to the middle position between  $M_1$  and  $M_2$  for both tangential and sagittal axes is shown in Fig. 6.10. The same telescope manipulation for injection laser beam size on both tangential and sagittal axes are made for the simplicity of the preliminary experiment. Ideally, 94 % coupling of injection laser beam power into cavity could be realized with this telescope configuration.

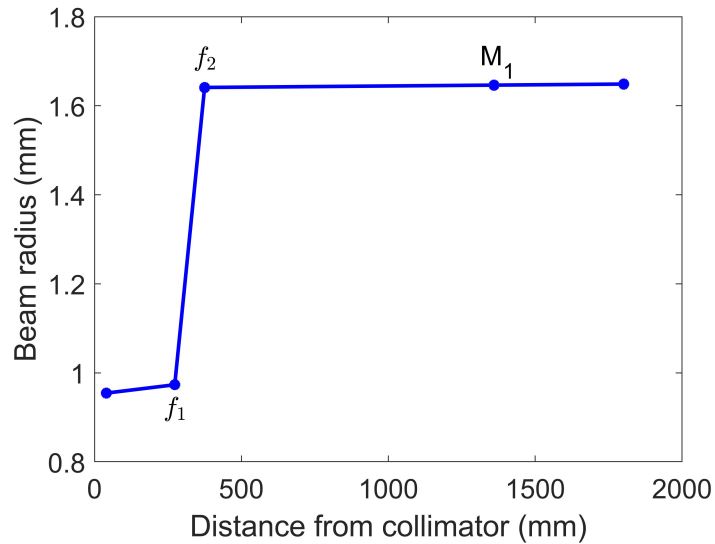


Figure 6.10 Laser beam radius size change versus distance from collimator for both tangential and sagittal axes in the preliminary TBOX setup. During the optical path, a telescope made up of one concave lens  $f_1$  with focal length of -150 mm and one convex lens  $f_2$  with focal length of +250 mm is used to tune injection laser beam size and divergence angle to match with that of the cavity mode, which could realize 94% coupling of injection laser beam power into cavity ideally.

After the implementation of telescope, primary cavity alignment is done in the following procedure. Two irises are put on mounts of cavity mirrors  $M_1$  and  $M_2$ . Injection laser is aligned to go through the centers of the two irises simultaneously by tuning the pair of alignment mirrors  $M_{A1}$  and  $M_{A2}$ . Then iris on cavity mirror mount 2 is replaced with cavity mirror  $M_2$ . Iris is put on cavity mirror mount 3. Screws of cavity mirror mount 2 are tuned to make the laser beam go through the center of iris mounted on cavity mirror mount 3. Then iris on cavity mirror mount 3 is replaced with cavity mirror  $M_3$ . Iris is put on cavity mirror mount 4. Screws of cavity mirror mount 3 are tuned to make the laser beam go through the center of iris mounted on cavity mirror mount 4. Then iris on cavity mirror mount 4 is replaced with cavity mirror  $M_4$ . Screws of cavity mirror mount 4 are tuned to make the laser beam go through the center of iris mounted on cavity mirror mount 1. Direction of laser beam after reflection of  $M_4$  and after transmission through

the center of iris mounted on cavity mirror mount 1 is marked with an iris 5 outside of the vacuum chamber. Finally, the iris mounted on cavity mirror mount 1 is replaced with cavity mirror  $M_1$ . The injection laser beam is aligned with the iris 5 through tuning the screws of cavity mirror mount 1. So far, the primary alignment of the cavity is finished.

The injection laser is locked with OEC by PDH method<sup>[62-63]</sup>. Here it is the optical frequency of the injection laser being tuned to be resonant with the OEC. The optical frequency of the injection laser is tuned through changing the laser oscillator cavity length, which is realized by applying a control signal onto the piezo attached to the end mirror of laser oscillator cavity. At the beginning of the locking process, to find the resonance optical frequency of the injection laser, a triangle control signal with amplitude of 0 to 10 V and repetition frequency of  $\sim 10$  Hz is generated by LaseLock (electronics module from TEM Messtechnik GmbH) and applied onto the piezo of Koheras. Thus a periodic scan of the laser central frequency is generated. Resonance peaks should show up in cavity transmission intensity signal measured by photodiode  $PD_2$  put at transmission position of  $M_2$ .  $PD_2$  of avalanche photodiode (APD, Laser Components A-CUBE-S3000-01) is used at the beginning when the power of transmission signal is low as  $\sim nW$  scale.  $PD_2$  of normal photodiode (Thorlabs DET 36 A/M) is used when intensity of cavity transmission is high enough to have signal with amplitude of at least  $\sim mV$  level on oscilloscope.

A crucial step of lock is to obtain a proper error signal for PDH feedback system to tell which side is the laser frequency deviate from the central resonance frequency and thereby to generate a control signal for laser piezo. The central frequency scanned laser wave will then goes through the electro-optic modulator (EOM). A sine wave with frequency of  $\Omega_1 = 8.2$  MHz and amplitude of  $\sim 100$  mVpp is generated by signal generator (SG1 in Fig. 6.1, RIGOL DG4162) and applied onto  $EOM_1$  (iXblue NIR-MPX-LN-0.1) to produce a phase modulation on the injection laser wave. Electric field of laser beam after  $EOM_1$  modulation can be expressed as  $E_L = E_0 e^{i(\omega_L t + \beta_1 \sin(\Omega_1 t))}$ , in which  $\omega_L$  is the central optical frequency of the laser beam corresponding to wavelength of 1064 nm. Modulation depth  $\beta_1$  depends on both the modulation signal with amplitude of  $\sim 100$  mVpp also the response of the  $EOM_1$ , and it's set to be very small thus the laser power shifted from the central frequency can be neglected. Equivalently, the sinusoidal phase modulation could be rewritten as two sidebands around the central optical frequency spaced with  $\Omega_1$  at each side as already shown in Section 2.3.2. The choice of modulation frequency  $\Omega_1$  depends on the resonance linewidth of the cavity that normally needs to be far away off

resonance, so the sidebands can be considered to be completely nonresonant with the OEC. Also the choice of the modulation frequency depends on the frequency properties of the operational amplifiers which will be used for producing error signal of the PDH feedback system. Here a modulation frequency of  $\Omega_1 = 8.2$  MHz is chosen which is corresponding to a maximum amplification of the operational amplifiers that are being used in the preliminary experiment and also the 8.2 MHz is far outside of the TBOX resonance linewidth of  $\sim 20$  kHz. Then the laser wave with central frequency triangularly periodically scanned and with two sidebands is injected into the cavity. The 8.2 MHz component in the cavity reflection signal as a result of interference between the sideband signal with the cavity reflected central frequency signal will provide information of the cavity central resonance frequency thus will provide error signal used for PDH feedback.

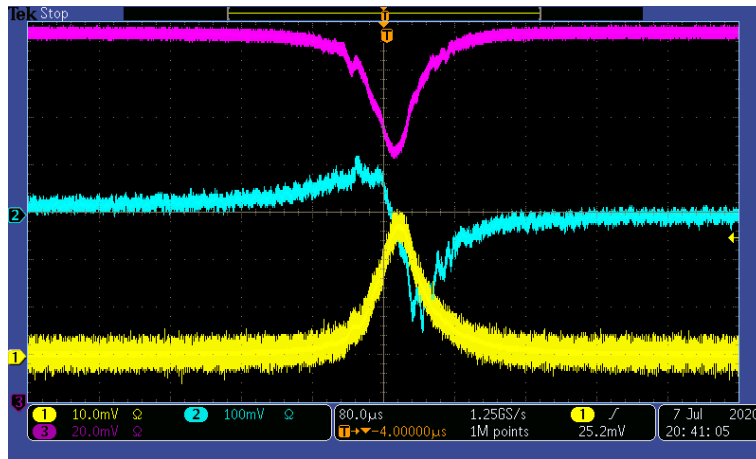


Figure 6.11 Example PDH error signal (blue) of preliminary TBOX from screenshot of oscilloscope, with cavity reflection (magenta) measured by PD<sub>1</sub> and cavity transmission (yellow) measured by PD<sub>2</sub>. These signals are taken after successfully solving the problems of noises as shown in Fig. 6.12.

Example signals from screenshot of oscilloscope during piezo scan process are shown in Fig. 6.11. The magenta curve is the signal measured by photodiode PD<sub>1</sub> (Thorlabs DET 36A/M) put at reflection position of M<sub>1</sub> from which one can read the transient coupling ratio of the injection laser beam into cavity. The transient coupling ratio reaches  $\sim 30\%$  maximally for signal in Fig. 6.11. The yellow curve is the signal measured by photodiode PD<sub>2</sub> (Thorlabs DET 36A/M) put at transmission position of M<sub>2</sub> showing the cavity resonance peak. The blue curve is the PDH error signal. The source of the error signal is taken from cavity reflection signal measured by photodiode PD<sub>3</sub> (Hamamatsu S1223-01) put at reflection position of coupling mirror M<sub>1</sub>. Then according to the mathematical process presented in Section 2.3.2, the error signal is generated through the following elec-

tronics processing. Signal measured by PD<sub>3</sub> is first processed by operational amplifiers to filter out the high intensity constant signal and the nonrelavent  $2\Omega_1$  frequency components, resulted with the single  $\Omega_1$  frequency components remaining and being amplified. Then the amplified single  $\Omega_1$  frequency signal is mixed with another single  $\Omega_1$  frequency signal from signal generator (SG1 in Fig. 6.1) with a proper phase to demodulate out the error signal as expressed in Eq. 2-28. Finally the pure error signal is generated after filtering out the high frequency term with low pass filter (Mini-Circuits BLP-1.9+). As it shown in Fig. 6.11, the crossing-zero point of the error signal is positioned at the moment when the resonance peak reaches the maximum, and the different sign of the error signal on the two sides could tell which direction is the injection laser frequency deviating from the maximum resonance frequency.

The clean signals shown in Fig. 6.11 are taken after successfully solving the problem of noises appearing in them as shown in Fig. 6.12. The noises are characterized with a similar frequency of  $\sim 160$  kHz in all three signals. These noises must be removed as the PDH feedback needs clean cavity transmission signal to set a threshold on the side of the resonance peak using as the trigger for lock and it needs clean error signal to lock the system. After thorough check of the cable connecting of the TBOX setup, the source of these noises are traced to be coming from piezo oscillation induced by the unclean  $\sim 10$  Hz triangular scan signal generated by LaseLock. Thus a potentiometer (BOURNS 3296) with resistance range from 10 ohm to 2 megaohm is implemented in the cable connecting the output of LaseLock with the input of Koheras piezo port as shown in Fig. 6.13, to successfully remove the noise. During experiment, the resistance of the potentiometer could be tuned to stop at the position where the noises disappear from the signals.

Before entering the locking process, fine tuning of alignment should be done with tuning screws on cavity mirror mounts and the pair of alignment mirrors, to optimize the intensity of the ideal cavity working mode  $TEM_{00}$  captured by CCD camera (Gentec Beamage-4M) put at transmission of  $M_3$ , to optimize the intensity of the yellow resonance peak and to optimize the coupling ratio. With enough optimization (for example transient coupling ratio reaching more than 50%) will greatly ease the following locking process. In the TBOX setup, alignment mirrors with two inch diameters are used to have a rather big range of tuning, and they are mounted on mirrors mounts (Newport Gimbal Mirror Mount U200-G) implemented with actuators (Newport Differential Micrometer Head DM-13) which could realize sub-micron resolution of tuning to be able to precisely

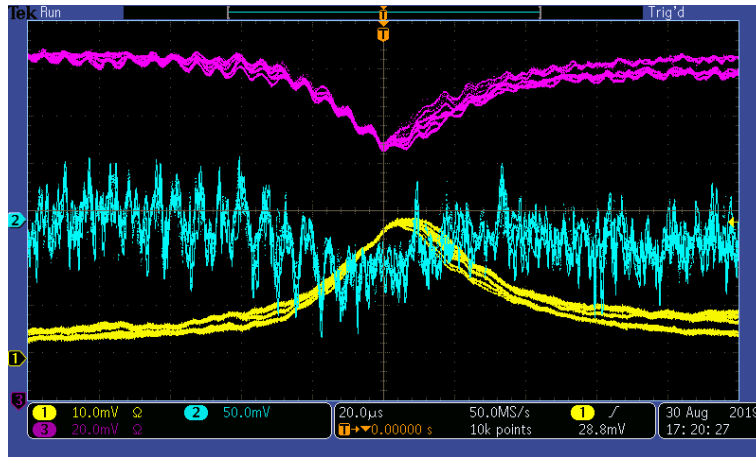


Figure 6.12 Noises with a similar frequency  $\sim 160$  kHz appear in PDH error signal (blue), cavity reflection (magenta) and cavity transmission (yellow), which is traced to be coming from piezo oscillation induced by the unclear  $\sim 10$  Hz triangular scan signal generated by LaseLock.



Figure 6.13 A potentiometer (BOURNS 3296, in color blue) with resistance range from 10 ohm to 2 megaohm is implemented in the cable connecting the output of LaseLock with the input of Koheras piezo port to successfully remove the noises as shown in Fig. 6.12 and resulted in clean signals as shown in Fig. 6.11.

tune the alignment of the injection laser. The photo of one alignment mirror is shown in Fig. 6.14. After the alignment optimization is done, then we enter the locking procedure.

The error signal is separated averagely to be used for two feedback loops. In the fast feedback loop, the error signal is used for generating a modulation signal to be applied to acousto-optic modulator (AOM, Chongqing Smart SCI&TECH Development Co. SGTF110-1064-1P) which will directly shift the central frequency of the injection laser. Technically, the error signal is used as an external modulation signal for signal generator (SG2 in Fig. 6.1) which is working at an frequency modulation (FM) mode. The AOM is working at a carrier frequency shift of 110 MHz with a bandwidth of 20 MHz. Signal



Figure 6.14 Alignment mirror mounts implemented with actuators which could realize sub-micron resolution of tuning used in preliminary TBOX experimental setup.

of frequency shift deviate from the carrier frequency is generated by SG2 proportionally to the error signal by tuning the *FMDev* manually, and stops at the position where for the yellow resonance peak the amplitude is clearly being amplified and the duration is clearly being extended. Also the fast feedback loop gain should not be too big to avoid oscillation of the resonance. Optimally, with the fast feedback loop alone, the duration of the resonance peak could be extended to second time scale. So far, the tuning of the fast feedback loop is finished. During the process, demodulation phase of the error signal maybe needs to be reversed to find a proper feedback phase for the fast feedback loop.

In the slow feedback loop, the error signal is imported into LaseLock. The LaseLock will be switched from *scan mode* to *regulator mode*. Correspondingly the control signal applied to laser piezo will be switched from a triangular scan signal to a algorithm generated regulating signal which aim to keep the error signal constantly zero. Cavity transmission signal measured by PD<sub>2</sub> will also be imported into LaseLock. A proper level of threshold will be set on the side of resonance peak to be used as trigger of lock. For the example signals shown in Fig. 6.11, a trigger threshold could be set as  $\sim 10$  mV. Then with manually tuning algorithm parameters including mainly the proportional-integral-derivative (PID) coefficients, lock could be realized when a proper piezo regulating signal generated by LaseLock and applied to laser piezo. Example screenshot of oscilloscope showing the transition of cavity state from unlocked to locked is presented in Fig. 6.15. When cavity is being locked, steady state is reached for cavity that the intra-cavity power is kept at a constant level which can be read from the signals of cavity transmission and reflection.

After injection laser being locked with cavity, optimization of the lock could be done

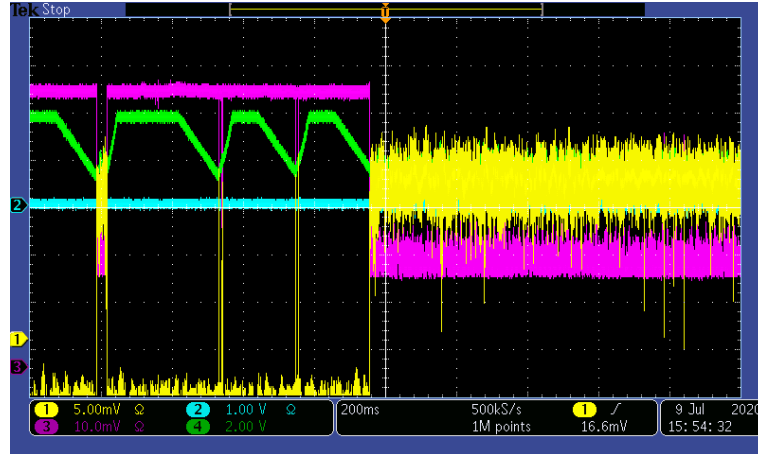


Figure 6.15 Example screenshot of oscilloscope shows the transition of preliminary TBOX state from unlocked to locked, in which cavity transmission signal measured by PD<sub>2</sub> is in color yellow, error signal is in color blue, cavity reflection signal measured by PD<sub>1</sub> is in color magenta, control signal applied to piezo of laser oscillator is in color green.

with optimizing the alignment through tuning the pair of alignment mirrors, optimizing polarization of the injection laser through rotating the half wave plate and quarter wave plate in the injection optical path, and optimizing the feedback through tuning the parameters in the two feedback loops. The optimization is done with the purpose of increasing the intra-cavity average power which can be read from the cavity transmission measured by photodiode and power meter; increasing the injection coupling ratio which can be read from the cavity reflection signal measured by photodiode; and increasing the intensity of the ideal cavity working mode TEM<sub>00</sub> which can be read from the measurement with CCD camera. After preliminary optimization, a coupling ratio of ~60% is realized for TBOX, which is read from the drop amplitude of cavity reflection signal (magenta) measured by photodiode PD<sub>1</sub> as shown in Fig. 6.15.

### 6.1.3 Key Parameters Measurement of TBOX

When injection laser is being locked with the external cavity, profile of cavity mode taken by CCD camera put at transmission position of M<sub>3</sub> is shown in Fig. 6.16. The beam profile is fitted with Gaussian distribution. Beam sizes on tangential and sagittal axes are taken as the radius values at  $1/e^2$  of the maximum intensity to be  $w_x=1.8$  mm,  $w_y=2.03$  mm, which are consistent with the calculated beam sizes as shown in Fig. 6.3 considering the beam is further diverged after transmission of M<sub>3</sub>.

The cavity FSR, finesse and linewidth are measured with the method in Ref.<sup>[111]</sup>. The experimental setup used for the measurement is changed with an addition of a second

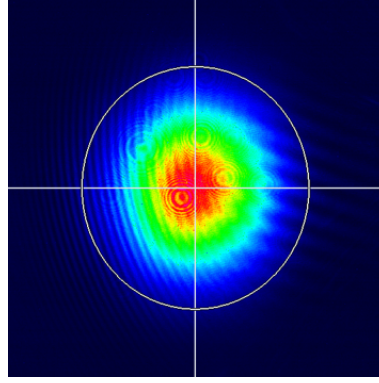


Figure 6.16 Profile of preliminary TBOX cavity mode taken by camera put at transmission position of  $M_3$ . Beam sizes are  $w_x=1.8$  mm,  $w_y=2.03$  mm on tangential and sagittal axes respectively, taking the radius values at  $1/e^2$  of the maximum intensity with Gaussian fit.

EOM as shown in Fig. 6.17. The central frequency component of the continuous wave injection laser is kept being locked with the cavity during the measurement process. A sine wave with frequency of  $\Omega_2$  and amplitude of  $\beta_2$  is generated by signal generator SG2 and applied to EOM<sub>2</sub> (iXblue NIR-MPX-LN-0.1) to produce a phase modulation on the laser wave. Different from the modulation made by EOM<sub>1</sub>,  $\Omega_2$  is set as a linear sweep centered around the cavity FSR and with a modulation depth  $\beta_2$  that make the laser power shift few tens percent from the central optical frequency when modulation frequency is far off the resonance linewidth range from the cavity FSR frequency. Electric field of laser beam after EOM<sub>2</sub> modulation can be expressed as  $E'_L = E_0 e^{i(\omega_L t + \beta_2 \sin(\Omega_2 t))}$ , with neglecting the modulations made by other elements including EOM<sub>1</sub>, AOM and piezo. The sine wave phase modulation can be rewritten as sum of infinite number of sidebands in Eq. 2-24. In the following content of this section, first the principle of the measurement method will be briefly analyzed, then the measurement done on TBOX will be presented.

The electric field of cavity transmission  $E_t$  measured at transmission position of  $M_2$  for a monochromatic injection wave with frequency  $\omega$  can be written from Eq. 2-27 as

$$E_t = \frac{t_1 t_2}{1 - \rho e^{i\omega/FSR}} E_L. \quad (6-1)$$

Only the DC components of the cavity transmission will be measured by photodiode PD<sub>2</sub>, which are basically each frequency components in Eq. 2-24 times the corresponding cavity response in Eq. 6-1 and sum the intensity of each frequency components. Since the central frequency  $\omega_L$  component of the injection laser is kept being locked with the cavity, thus we have the relation  $\omega_L = pFSR$ , in which  $p$  is integer. So the central frequency component is eliminated as it being a constant offset in the scan curve which doesn't

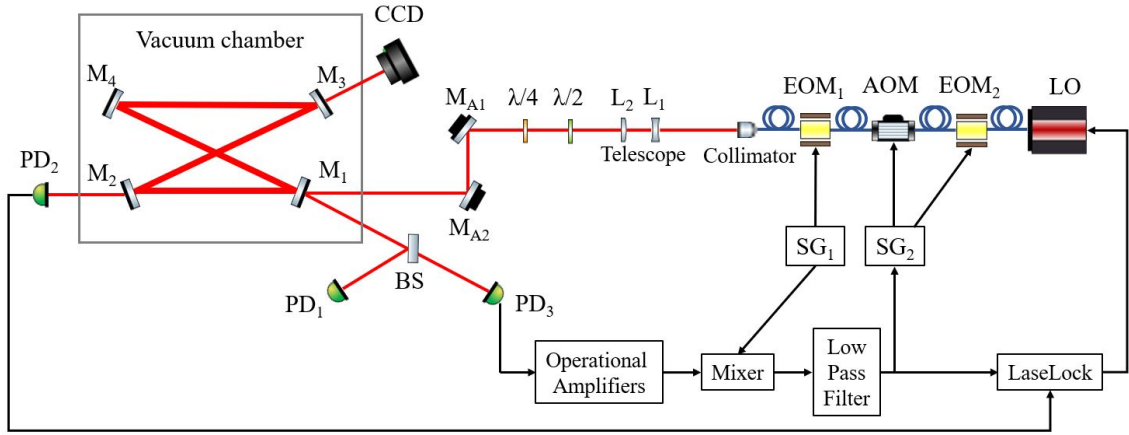


Figure 6.17 Experimental setup used for measurement of cavity FSR, finesse and linewidth. A second EOM is added compared to experimental setup shown in Fig. 6.1. LO: laser oscillator. AOM: acousto-optic modulator. EOM: electro-optic modulator. PD: photodiode. CCD: camera. SG: signal generator.

contribute to the measurement. Also the phase of the cavity response is simplified using the relation. And global amplitude factor  $E_0 t_1 t_2$  is eliminated. For all integer  $n$ ,

$$I_t = \sum_{n=1}^N \left[ |E_t(\omega_L + n\Omega_2)|^2 + |E_t(\omega_L - n\Omega_2)|^2 \right], \quad (6-2)$$

in which

$$|E_t(\omega_L \pm n\Omega_2)| = \left| \frac{J_n(\beta_2) e^{i(\omega_L \pm n\Omega_2)t}}{1 - \rho e^{\mp i n \Omega_2 / FSR}} \right|. \quad (6-3)$$

For example, for cavity FSR assumed to be 79.3 MHz, with the setting as a frequency range of  $\Omega_2 = [-250, +250]$  kHz centered around 79.3 MHz being linearly scanned in 1 s time period with a modulation depth  $\beta_2 = 1$ , the first three order components of  $I_t$  are calculated as shown in Fig. 6.18. The modulation depth of  $\beta_2 = 1$  is corresponding to  $1 - J(0, 1) \approx 23\%$  of the laser power being shifted from the central frequency, which is the condition similar to the measurement we make. From Fig. 6.18 we can see a second order expansion of the injection laser field would be enough. Then the normalized scan curve of  $M_2$  transmission calculated with second order expansion is shown in Fig. 6.19, compared with the normalized cavity resonance peak calculated by Eq. 2-12 using the parameters in Table 6.1. The two curves in Fig. 6.19 are all normalized by dividing with their maximums. A good consistency has been achieved between the normalized scan curve with the normalized cavity resonance peak. Thus for a real measurement the normalized scan curve could be directly fitted with a Lorentzian function as shown in Eq. 2-12, from which the cavity finesse and linewidth could be calculated.

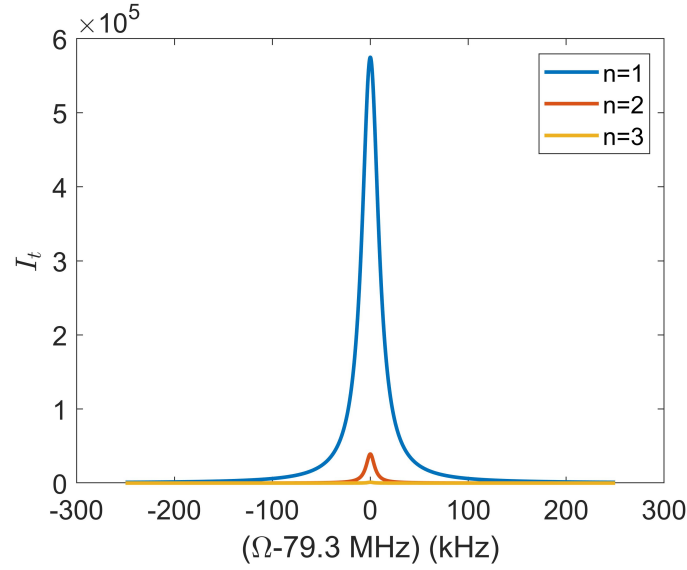


Figure 6.18 The first three order components of  $I_t$  calculated by Eq. 6-2 with parameters of preliminary TBOX and a scan setting of  $\Omega_2 = [-250, +250]$  kHz centered around 79.3 MHz being scanned in 1 s time period with a modulation depth  $\beta_2 = 1$ , in which the cavity FSR is assumed to be 79.3 MHz in the calculation.

During the measurement made on preliminary TBOX, The modulation frequency is first being tuned manually. FSR= 79.15 MHz with a precision of 0.01 MHz is found during the tuning of modulation frequency which is corresponding to the maximum of the transmission resonance peak. A scan with frequency range of  $\Omega_2 = [-250, +250]$  kHz centered around 79.15 MHz in 1 s time period is launched on preliminary TBOX. Fig. 6.20 shows the normalized measurement data of cavity transmission (blue) and the Lorentzian function fitted curve (red). The cavity finesse is calculated to be  $\mathcal{F} \simeq 1610$ , cavity resonance linewidth  $\Delta\nu_c \simeq 50$  kHz. The oscillation showing in the cavity transmission signal that is consistent with those show in Fig. 6.15 could come from both the imperfect locking and the environmental noise in the experimental setup. The measurement values of cavity finesse and linewidth could be further improved with optimization of the locking and reduction of the environmental noise.

The output power of Koheras is tuned to be 103 mW on the control panel. With laser power losses mainly induced by the insertion losses of the AOM and two EOMs each with  $\sim 3$  dB, the injection laser power is measured to be 17.08 mW before the injection window of vacuum chamber. Cavity transmission power of  $163.0 \mu\text{W}$  is measured at transmission position of  $M_4$ . Taking the  $M_4$  transmission coefficient of 72 ppm as shown in Table 6.1, the cavity gain is calculated to be  $\sim 133$ . Using the definition of cavity round trip loss, finesse and gain defined in Section 5.2.2, taking the value of coupling ratio  $|c_{00}|^2 = 60\%$

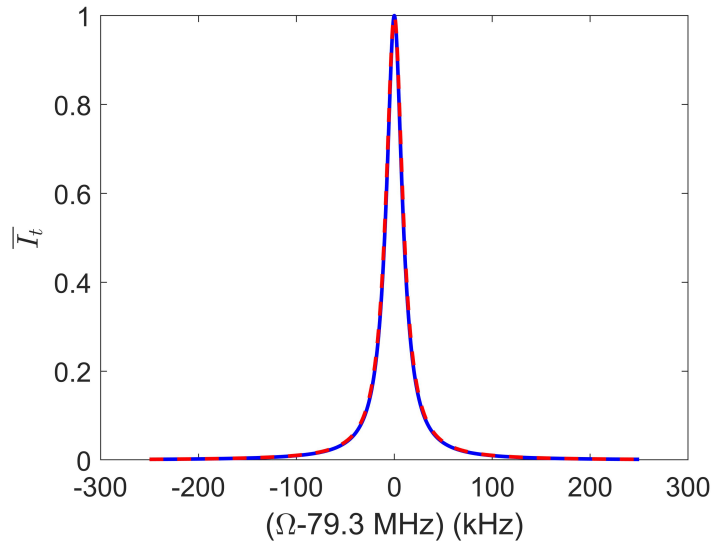


Figure 6.19 Normalized cavity transmission curve (blue) calculated by Eq. 6-2 up to second order expansion, with parameters of preliminary TBOX and a scan setting of  $\Omega_2 = [-250, +250]$  kHz centered around 79.3 MHz being scanned in 1 s time period with a modulation depth  $\beta_2 = 1$ . And the normalized TBOX cavity resonance peak (red) calculated by Eq. 2-12. Cavity FSR is assumed to be 79.3 MHz in the calculation.

. The intra-cavity power losses are calculated to be 2254 ppm and 1943 ppm from the measured cavity finesse and gain respectively.

The cavity finesse and gain could be further optimized, except with the optimization procedures mentioned in the end of Section 6.1.2, additional optimization could be made with changing the experimental setup for example put the two telescope lenses on translation stages to be able to optimize the mode matching after cavity being locked. Limited to the available injection laser, the preliminary experiment of prototype OEC is limited to the successful lock of a CW injection laser oscillator with the external cavity.

## 6.2 Design of High Power Experiments on TBOX

After the preliminary experiment of successfully lock a CW injection laser with the prototype OEC, the next step high power experiment is designed to realized the goals demanded for OEC. The goals include a laser beam waist with radius size of few tens of micrometers inside OEC, intra-cavity laser pulse length of  $\sim 10$  ps with repetition rate of few tens of MHz, and an hour-time-scale stable intra-cavity average power of few hundreds of kilowatts. And still the OEC will not be coupled with electron storage ring. The high power experimental setup of TBOX is shown in Fig. 6.21. The OEC for high power experiment is designed with the same geometrical parameters including cavity round trip

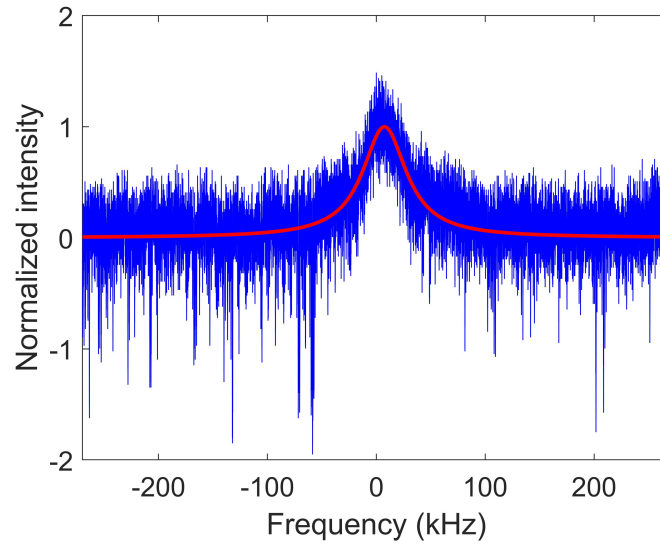


Figure 6.20 Normalized measurement data of cavity transmission (blue) with data taken by photodiode PD<sub>2</sub> put at transmission position of M<sub>2</sub>. Normalization is made with the measurement data divided by its maximum after shift the offset to zero. And the fitted Lorentzian function (red), from which the cavity finesse and linewidth are calculated to be  $\mathcal{F} \simeq 1610$  and  $\Delta\nu_c \simeq 50\text{kHz}$ .

length of  $\sim 3.78\text{ m}$ , distances between mirrors and incidence angle as shown in Fig. 6.2. Diameters of cavity mirrors and radius of curvatures of concave mirrors will also be one inch and 1 m respectively. It means the laser beam transverse size inside high power TBOX will behaves the same as that in preliminary TBOX as shown in Fig. 6.3, Fig. 6.4 and Fig. 6.5. The OEC will be installed in the same vacuum chamber as used in preliminary experiment. However, changes will be made in several aspects compared with the preliminary experimental setup shown in Fig. 6.1.

Key parameters designed for high power TBOX cavity mirrors are summarized in Table 6.2. With transmission of cavity mirrors M<sub>2</sub>, M<sub>3</sub>, M<sub>4</sub> fixed and neglecting all other intra-cavity power losses, the ideal cavity finesse (blue) and cavity gain (red) versus transmission T<sub>1</sub> of cavity mirror M<sub>1</sub> are calculated by Eq. 2-11 as shown in Fig. 6.22. The black dashed line indicates the condition of high power TBOX where T<sub>1</sub> = 200 ppm with the ideal cavity finesse of  $\sim 2.9 \times 10^4$  and cavity gain of  $\sim 1.7 \times 10^4$ , which tells high power TBOX will be working at a over-coupled regime. The gain curve at over-coupled regime is with a rather flat slope thus the cavity will be less affected by varying T<sub>1</sub> compared to the regime on the left side of the maximum gain. An average intra-cavity power of  $\sim 300\text{ kW}$  could be realized with a commercially available high-average-power PW injection laser whose output power can be up to  $\sim 100\text{ W}$ . The injection laser pulse length will be

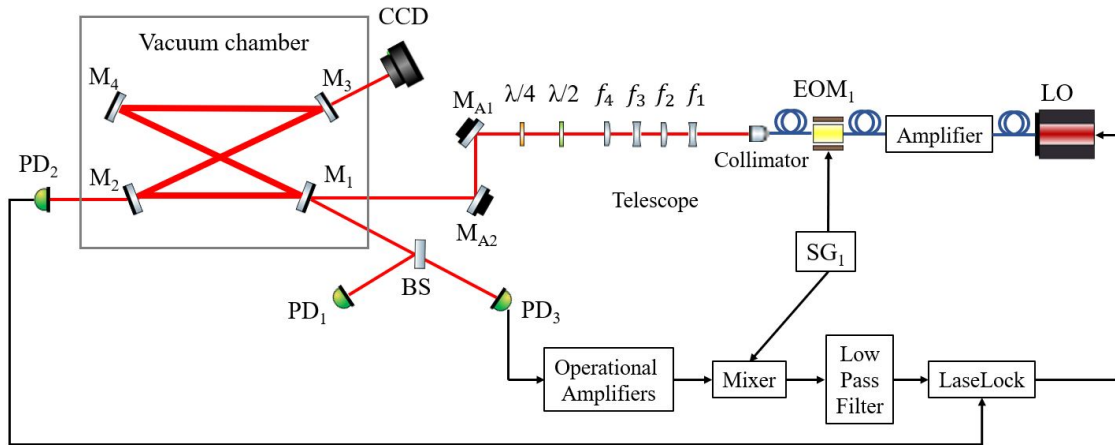


Figure 6.21 High power experimental setup of TBOX. LO: laser oscillator. AOM: acousto-optic modulator. EOM: electro-optic modulator. PD: photodiode. CCD: camera. SG: signal generator.

$\sim 20$  ps. The cavity resonance linewidth is calculated to be  $\sim 2.7$  kHz by Eq. 2-11 and it demands for the injection PW laser to have ultra low phase noise. Besides, for PW injection laser, scheme for tuning carrier-phase-envelope (CEP) needs to be implemented.

Table 6.2 Designed parameters of high power TBOX cavity mirrors.

Mirror	Type	Substrate Material	Transmission (ppm)
$M_1$	Planar	Suprasil	200
$M_2$	Planar	ULE	5
$M_3$	Concave	ULE	5
$M_4$	Concave	ULE	5

Telescope made up of four cylindrical lenses will be used for mode matching in high power experiment, with two cylindrical lenses used for tuning beam size on tangential axis and two for sagittal axis. This is because the cavity mode size on tangential and sagittal axes will become more and more asymmetry with the mirror surface thermoelastically deformed when intra-cavity power is increasing. The cavity mode radius size on  $M_1$  with intra-cavity average power changing from 0 to 500 kW is shown in Fig. 6.23 calculated by ABCD matrix in Eq. 4-5 and mirror surface deformation calculated by Winkler model. The beam will become more elliptical with the major axis along sagittal direction. The telescope could set to be fixed at the position optimized for mode matching at targeted high power state, or they could be mounted on translation stages to be able to tuned during power up experiments.

A pair of D-shape mirrors will be implemented in the middle of cavity mirrors  $M_1$

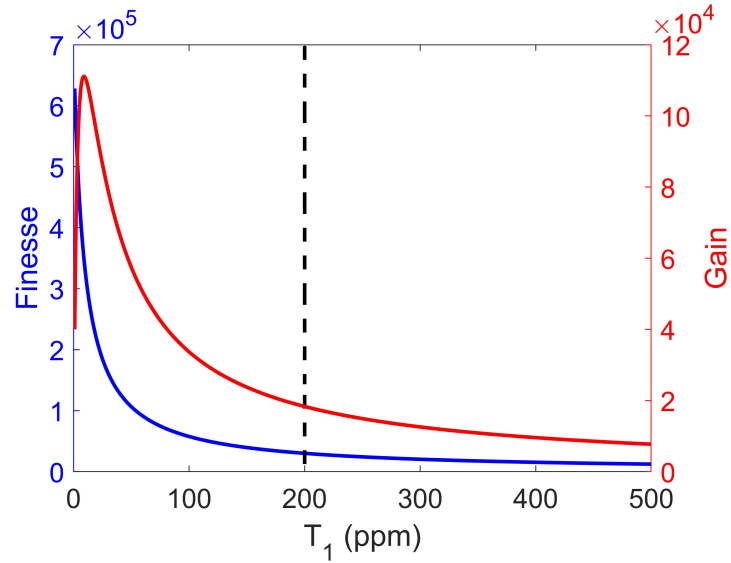


Figure 6.22 For high power TBOX, with transmission of cavity mirrors  $M_2$ ,  $M_3$ ,  $M_4$  fixed to the values shown in Table 6.2 and neglecting all other intra-cavity power losses, the ideal cavity finesse (blue) and cavity gain (red) versus transmission  $T_1$  of cavity mirror  $M_3$  are calculated by Eq. 2-11. The black dashed line indicates the condition of TBOX where  $T_1 = 200$  ppm with the ideal cavity finesse of  $\sim 2.9 \times 10^5$  and cavity gain of  $\sim 1.7 \times 10^4$ , which tells high power TBOX will be working at a over-coupled regime.

and  $M_2$  to suppress modal instabilities at high power state as already shown in Chapter 4. As it shown in Fig. 6.24, the lowest order of high order mode degenerated with  $TEM_{00}$  is calculated for TBOX with intra-cavity average power  $P_c$  range from 0 to 500 kW, in which  $m$  corresponds to the mode order on tangential axis,  $n$  corresponds to the mode order on sagittal axis. The calculation is without considering the limitation from the finite mirror size. The degenerated high mode orders are similar to the condition that has been shown in Chapter 4, so the D-shape mirrors would be effective to remove modal instabilities.

### 6.3 Design of Optical Enhancement Cavity for TTX

After realizing the goals demanded for OEC itself, the final step is to couple the OEC with electron storage ring to produce  $\sim 10^{10}$  photons/s high average flux X-rays. The OEC of TTX will be with round trip length of  $\sim 5.668$  m to match the repetition rate of laser pulse circulating inside OEC with the repetition rate of the electron beam circulating in storage ring with a circumference of  $\sim 5.668$  m as shown in Fig. 6.6. The same four-mirror planar bow-tie structure as shown in Fig. 6.2 will be employed by the OEC of TTX with the same cavity mirrors as that of high power TBOX shown in Table 6.2. The sizes

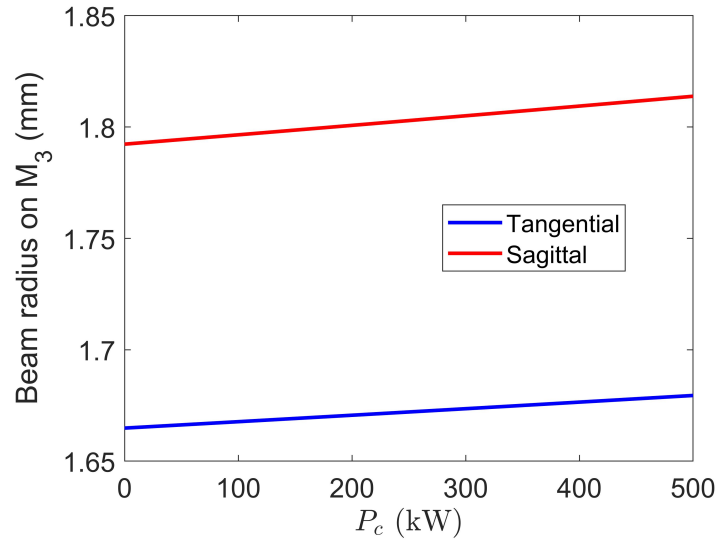


Figure 6.23 For TBOX with intra-cavity average power  $P_c$  range from 0 to 500 kW, beam radius sizes on cavity mirror  $M_3$  are calculated with ABCD matrix using mirror surface deformation calculated from Winkler model.

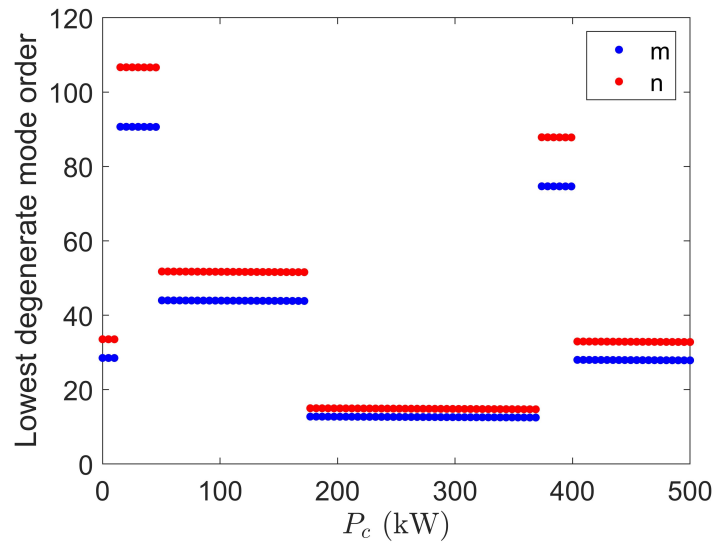


Figure 6.24 For TBOX with intra-cavity average power  $P_c$  range from 0 to 500 kW, the lowest order of high order mode degenerated with  $TEM_{00}$ .  $m$  corresponds to the mode order on tangential axis,  $n$  corresponds to the mode order on sagittal axis. The calculation is without considering the limitation from the finite mirror size.

of OEC of TTX are designed with a 1.5 times scale up of the prototype OEC, resulted in the distances  $L_1, L_2, L_3, L_4$  are [1323,1421,1505,1421] mm,  $d = 120$  mm and incidence angle on  $M_2$  is  $\theta = 2.422^\circ$ . Radius of curvatures of the two concave mirrors  $M_3$  and  $M_4$  are 1.5 m. The intra-cavity laser beam size evolution on tangential and sagittal axis are calculated and shown in Fig. 6.25. A laser beam waist with radius size of  $111 \mu\text{m}$  on

tangential axis and  $97.0 \mu\text{m}$  on sagittal axis is designed to be positioned in the middle between  $M_3$  and  $M_4$  as shown in Fig. 6.25.

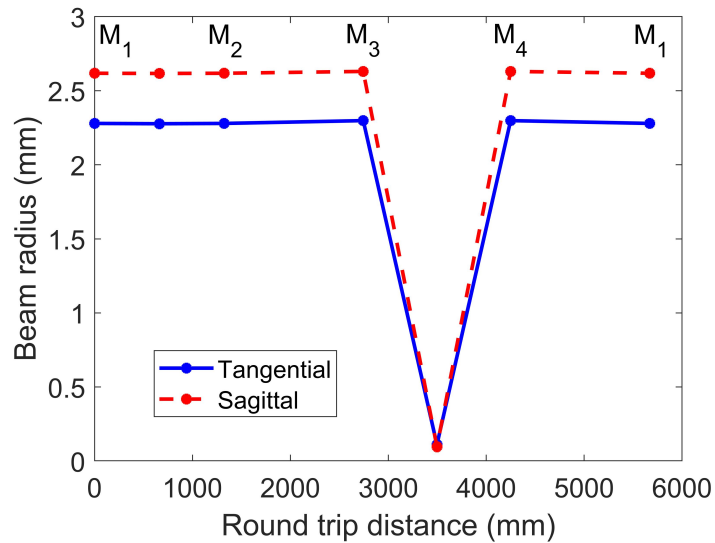


Figure 6.25 Laser beam radius size change inside OEC of TTX on tangential (blue) and sagittal (red) axes with respect to the round trip distance from  $M_1$ . The texts " $M_1, M_2, M_3, M_4$ " mark the corresponding cavity mirror positions. A laser beam waist with radius size of  $111 \mu\text{m}$  on tangential axis and  $97.0 \mu\text{m}$  on sagittal axis exists in the middle position between cavity mirror  $M_3$  and  $M_4$ .

Intra-cavity laser beam waist size could be tuned by changing  $L_3$  as the relation of waist radius versus  $L_3$  shown in Fig. 6.26. Repetition rate of laser pulse circulating inside OEC could be tuned with changing OEC round trip length by changing  $L_1$  without varying much the laser beam waist size as shown in Fig. 6.27.

New vacuum chamber will be designed to be able to contain the OEC of TTX and to be coupled with the vacuum pipe of electron storage ring with an residual pressure of  $10^{-7}$  mbar. The same injection line and feedback system of high power TBOX will be used for OEC of TTX to realize a stable intra-cavity average power of 300 kW. For optical cavity working in accelerator environment rather than in clean room, vibrational noises must be shielded to ensure a stable lock of OEC. The OEC will be installed on ultra-stable optical table to shield the seismic noise. Housing will be installed on the optical table around the setup of OEC to shield the vibrational noises transmitted through air.

For OEC of TTX working at a stable intra-cavity average power of 300 kW, it is corresponding to laser pulse with energy of 5.668 mJ and pulse length of 20 ps circulating inside OEC with a repetition rate of 52.93 MHz. To scatter the laser beam circulating inside OEC with electron beam circulating inside electron storage ring at the same fre-

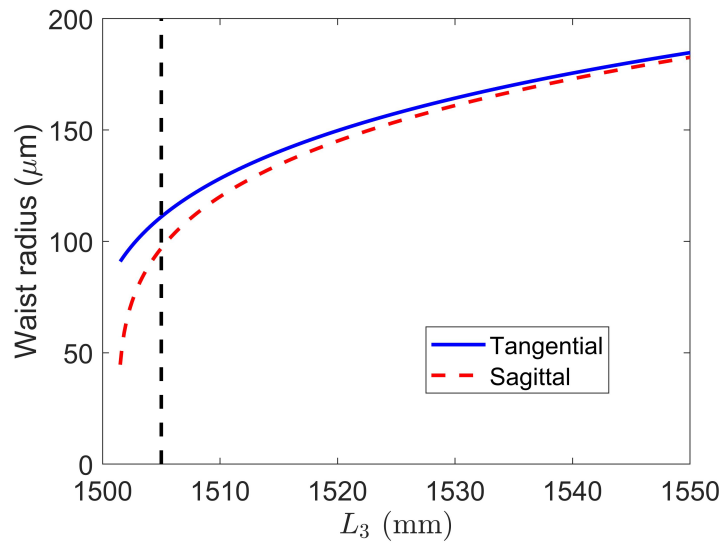


Figure 6.26 For OEC of TTX to be coupled with electron storage ring, relation of intra-cavity laser beam waist radius versus  $L_3$  the distance between cavity mirror  $M_3$  and  $M_4$  when distances between other mirrors are fixed. Black dashed line indicates the condition of OEC of TTX where  $L_3 = 1505$  mm. Tuning of intra-cavity laser beam waist size could be realized by changing  $L_3$ .

quency of 52.93 MHz with charge of 1 nC, bunch length of 20 ps and transverse rms size of 1.5 mm tangentially and 0.5 mm sagittally, TTX is envisaged to produce X-ray with an energy cut-off of 45 keV and average flux of  $\sim 10^{10}$  photons/s.

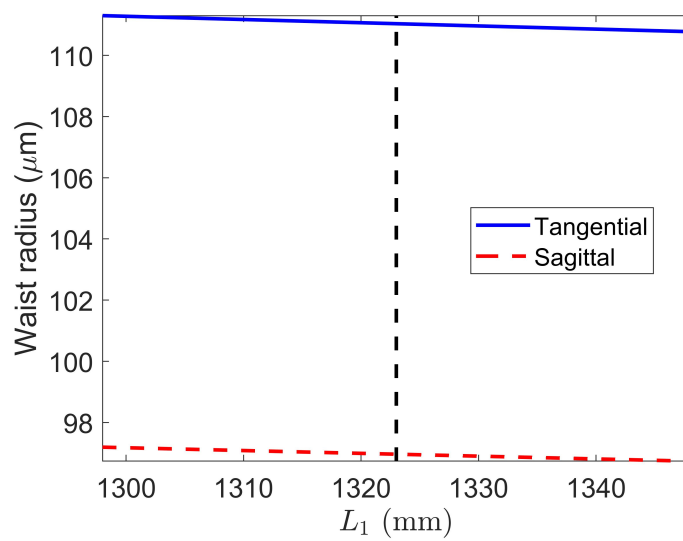


Figure 6.27 For OEC of TTX to be coupled with electron storage ring, relation of intra-cavity laser beam waist radius versus  $L_1$  the distance between cavity mirror  $M_1$  and  $M_2$  when distances between other mirrors are fixed. Black dashed line indicates the condition of OEC of TTX where  $L_1 = 1323$  mm. Repetition rate of laser pulse circulating inside OEC could be tuned with changing OEC round trip length by changing  $L_1$  without varying much the intra-cavity laser beam waist size.

## Chapter 7 Concluding Remarks

In this thesis, with the targeted application in Thomson scattering light sources for producing high average flux and high quality X/ $\gamma$ -rays, the studies of high-average-power optical enhancement cavity (OEC) are carried out theoretically and experimentally. The compact Thomson scattering light source could fill the gap between the conventional X/ $\gamma$ -ray sources and synchrotrons or free electron lasers, thus enables easier access to high quality X/ $\gamma$ -rays for wide range of frontier researches.

The studies are done with the purpose of realizing the designing goals demanded by Thomson scattering light source for OEC, that are: a small laser beam waist existing inside OEC with a radius size of few tens of micrometers, intra-cavity laser beam pulse length of picosecond scale, and a stable intra-cavity average power of few hundreds of kilowatts for hour time scale.

An expression of highly focused linearly polarized laser field is derived through a generalized Lax series expansion method, realizing good consistency with the precise integral Ignatovsky solution, thus providing a precise and efficient description of the laser field inside OEC for Thomson scattering simulation.

The modal instabilities appearing apparently on OEC with an average intra-cavity power reaching more than 100 kW affecting cavity stability are well understood. The experimental observed modal instabilities could be well described with the modal we established ascribing this phenomenon to the mode degeneracies induced by mirror surface thermoelastic deformation characterized with Winkler model. The D-shape mirror method is brought up to suppress modal instabilities in high-average-power OEC. And the effectiveness of this method is well proved with simulation. Experiment was carried out on prototype OEC of Thomson scattering light source ThomX with the implementation of D-shape mirrors inside and realized an hour-time-scale stable intra-cavity average power of 200 kW.

The fast intra-cavity power drop phenomenon appearing on high-finesse OEC is well understood with the model we established. The model attributes this phenomenon to the scattering loss induced by mirror surface thermoelastic deformation due to a hot spot contaminant. Based on this model, the experimentally recorded transient power drop behavior could be well reproduced with simulation. This analysis could help to understand

the physical process behind this phenomenon and help to prevent permanent mirror damage of high-average-power OEC being applied in wide range of applications including cavity-enhanced high-order harmonic generation, gravitational wave detection, steady-state microbunching (SSMB) light source and fusion energy experiment etc.

The full design of the prototype OEC of TTX is provided and preliminary experiment is carried out on it. The goal of locking a continuous wave injection laser with the prototype OEC is successfully realized and the cavity gain is measured to be 133. Design of the high power TTX prototype OEC experimental setup and the design for TTX OEC to be coupled with the electron storage ring are provided.

The R&D work of the OEC for TTX will be continued. Also the R&D work of the OEC for SSMB at Tsinghua has been ongoing and will be continued. More works based on OEC are being envisaged.

To satisfy the ultimate demands for OEC from a wide range of applications to reach megawatt average intra-cavity power level, problems yet exist to be solved including: to find out the reason and tackle with the gain drop with increasing injection laser power; dealing with thermal effects to increase the stability of OEC.

## Bibliography

- [1] Maiman T H. Stimulated optical radiation in ruby[J]. *nature*, 1960, 187(4736): 493-494.
- [2] Strickland D, Mourou G. Compression of amplified chirped optical pulses[J]. *Optics communications*, 1985, 56(3): 219-221.
- [3] Jackson J D. *Classical electrodynamics*[M]. John Wiley & Sons, 2007.
- [4] Bilderback D H, Elleaume P, Weckert E. Review of third and next generation synchrotron light sources[J]. *Journal of Physics B: Atomic, molecular and optical physics*, 2005, 38(9): S773.
- [5] Willeke F. Commissioning of NSLS-II[R]. Brookhaven National Laboratory (BNL), 2015.
- [6] Hongjie X, Zhentang Z. Current status and progresses of SSRF project[J]. *Nuclear Science and Techniques*, 2008, 19(1): 1-6.
- [7] Pellegrini C, Marinelli A, Reiche S. The physics of x-ray free-electron lasers[J]. *Reviews of Modern Physics*, 2016, 88(1): 015006.
- [8] Madey J M. Stimulated emission of bremsstrahlung in a periodic magnetic field[J]. *Journal of Applied Physics*, 1971, 42(5): 1906-1913.
- [9] Elias L R, Fairbank W M, Madey J M, et al. Observation of stimulated emission of radiation by relativistic electrons in a spatially periodic transverse magnetic field[J]. *Physical Review Letters*, 1976, 36(13): 717.
- [10] Deacon D A, Elias L, Madey J M, et al. First operation of a free-electron laser[J]. *Physical Review Letters*, 1977, 38(16): 892.
- [11] Bonifacio R, Pellegrini C, Narducci L. Collective instabilities and high-gain regime free electron laser[J]. *Optics Communications*, 1984, 50(6): 373-378.
- [12] Emma P, Akre R, Arthur J, et al. First lasing and operation of an ångstrom-wavelength free-electron laser[J]. *nature photonics*, 2010, 4(9): 641-647.
- [13] Yu L H. Generation of intense uv radiation by subharmonically seeded single-pass free-electron lasers[J]. *Physical Review A*, 1991, 44(8): 5178.
- [14] Allaria E, Castronovo D, Cinquegrana P, et al. Two-stage seeded soft-X-ray free-electron laser[J]. *Nature Photonics*, 2013, 7(11): 913-918.
- [15] Huang Z, Ruth R D. Laser-electron storage ring[J]. *Physical Review Letters*, 1998, 80(5): 976.
- [16] Loewen R. A compact light source: design and technical feasibility study of a laser-electron storage ring x-ray source[D]. Stanford Linear Accelerator Center, Menlo Park, CA (US), 2004.
- [17] Hsu I C, Chu C C, Yu C I. Energy measurement of relativistic electron beams by laser compton scattering[J]. *Physical Review E*, 1996, 54(5): 5657.
- [18] Klein O, Nishina Y. Über die streuung von strahlung durch freie elektronen nach der neuen relativistischen quantendynamik von dirac[J]. *Zeitschrift für Physik*, 1929, 52(11-12): 853-868.

- 
- [19] Hornberger B, Kasahara J, Gifford M, et al. A compact light source providing high-flux, quasi-monochromatic, tunable X-rays in the laboratory[C]// *Advances in Laboratory-based X-Ray Sources, Optics, and Applications VII: volume 11110*. International Society for Optics and Photonics, 2019: 1111003.
- [20] Huang J, Günther B, Achterhold K, et al. Energy-dispersive x-ray absorption spectroscopy with an inverse Compton source[J]. *Scientific reports*, 2020, 10(1): 1-10.
- [21] Variola A, Haissinski J, Loulergue A, et al. Thomx technical design report[R]. 2014.
- [22] Du Y, Yan L, Hua J, et al. Generation of first hard x-ray pulse at Tsinghua Thomson scattering x-ray source[J]. *Review of Scientific Instruments*, 2013, 84(5): 053301.
- [23] Androsov V, Bazarov S, Berezka V, et al. Commissioning of the storage ring for the Kharkov generator of x-ray radiation NESTOR[C]// *Proc. 9th Int. Particle Accelerator Conf. (IPAC'13)*, Vancouver, Canada, May 2018. 4307-4309.
- [24] Chaikovska I, Cassou K, Chiche R, et al. High flux circularly polarized gamma beam factory: coupling a Fabry-Perot optical cavity with an electron storage ring[J]. *Scientific Reports*, 2016, 6: 36569.
- [25] Bonis J, Chiche R, Cizeron R, et al. Non-planar four-mirror optical cavity for high intensity gamma ray flux production by pulsed laser beam Compton scattering off GeV-electrons[J]. *Journal of instrumentation*, 2012, 7(01): P01017.
- [26] Sakaue K, Washio M, Araki S, et al. Laser-Compton scattering x-ray source based on normal conducting linac and optical enhancement cavity[C]// *Proc. 6th Int. Particle Accelerator Conf. (IPAC'15)*, Richmond, USA, May 2015. 1635-1637.
- [27] Fukuda M, Araki S, Honda Y, et al. Development and upgrade plan of an x-ray source based on laser Compton scattering in laser undulator compact x-ray source(LUCX)[C]// *Proc. 7th Int. Particle Accelerator Conf. (IPAC'16)*, Busan, Korea, May 2016. 1867-1869.
- [28] Akagi T, Kosuge A, Araki S, et al. Narrow-band photon beam via laser Compton scattering in an energy recovery linac[J]. *Physical Review Accelerators and Beams*, 2016, 19(11): 114701.
- [29] Faillace L, Agostino R, Bacci A, et al. Status of compact inverse Compton sources in Italy: BriXS and STAR[C]// *Advances in Laboratory-based X-Ray Sources, Optics, and Applications VII: volume 11110*. International Society for Optics and Photonics, 2019: 1111005.
- [30] Serafini L, et al. Multi-disciplinary advanced research infrastructure for the generation and application of x-rays[R]. 2019.
- [31] Favier P. Etude et conception d'une cavité Fabry-Perot de haute finesse pour la source compacte de rayons x Thomx[D]. Université Paris-Saclay, 2017.
- [32] Favier P, Amoudry L, Cassou K, et al. Optimization of a Fabry-Perot cavity operated in burst mode for Compton scattering experiments[J]. *Physical Review Accelerators and Beams*, 2018, 21(121601).
- [33] You Y. A study of optical enhancement cavity with short pulse lasers for laser electron beam interaction[D]. Tsinghua University&Paris-Saclay University, 2014.
- [34] Liu X. R&D of a high-average-power Fabry-Pérot resonator for Thomson scattering experiments[D]. Tsinghua University&Paris-Saclay University, 2018.

## Bibliography

---

- [35] Xu H, Huang W, Tang C, et al. Design of a 4.8-m ring for inverse Compton scattering x-ray source[J]. *Physical Review Special Topics-Accelerators and Beams*, 2014, 17(7): 070101.
- [36] Rui T, Huang W. Lattice design and beam dynamics of a storage ring for a Thomson scattering x-ray source[J]. *Physical Review Accelerators and Beams*, 2018, 21(10): 100101.
- [37] Krause J L, Schafer K J, Kulander K C. High-order harmonic generation from atoms and ions in the high intensity regime[J]. *Physical Review Letters*, 1992, 68(24): 3535.
- [38] Carstens H. Enhancement cavities for the generation of extreme ultraviolet and hard x-ray radiation[D]. Ludwig Maximilian University of Munich, 2016.
- [39] Saule T, Heinrich S, Schoetz J, et al. High-flux ultrafast extreme-ultraviolet photoemission spectroscopy at 18.4 mhz pulse repetition rate[J]. *Nature communications*, 2019, 10(1): 1-10.
- [40] Pupeza I, Holzberger S, Eidam T, et al. Compact high-repetition-rate source of coherent 100 eV radiation[J]. *Nature Photonics*, 2013, 7(8): 608-612.
- [41] Cingöz A, Yost D C, Allison T K, et al. Direct frequency comb spectroscopy in the extreme ultraviolet[J]. *Nature*, 2012, 482(7383): 68-71.
- [42] Corder C, Zhao P, Bakalis J, et al. Ultrafast extreme ultraviolet photoemission without space charge[J]. *Structural Dynamics*, 2018, 5(5): 054301.
- [43] Mills A, Zhdanovich S, Na M, et al. Cavity-enhanced high harmonic generation for extreme ultraviolet time- and angle-resolved photoemission spectroscopy[J]. *Review of Scientific Instruments*, 2019, 90(8): 083001.
- [44] Ozawa A, Zhao Z, Kuwata-Gonokami M, et al. High average power coherent VUV generation at 10 mhz repetition frequency by intracavity high harmonic generation[J]. *Optics express*, 2015, 23(12): 15107-15118.
- [45] Willke B, Aufmuth P, Aulbert C, et al. The GEO 600 gravitational wave detector[J]. *Classical and Quantum Gravity*, 2002, 19(7): 1377.
- [46] Evans M, Gras S, Fritschel P, et al. Observation of parametric instability in Advanced LIGO[J]. *Physical review letters*, 2015, 114(16): 161102.
- [47] Allocca A, Chiummo A, Ruggi P, et al. Transient power drop in dark fringe lock acquisition during the commissioning before O3[J/OL]. *Virgo note*, 2019. <https://tds.virgo-gw.eu/ql/?c=14881>.
- [48] Aasi J, Abbott B, Abbott R, et al. Advanced LIGO[J]. *Classical and quantum gravity*, 2015, 32(7): 074001.
- [49] Acernese F, Agathos M, Agatsuma K, et al. Advanced Virgo: a second-generation interferometric gravitational wave detector[J]. *Classical and Quantum Gravity*, 2014, 32(2): 024001.
- [50] Ratner D F, Chao A W. Steady-state microbunching in a storage ring for generating coherent radiation[J]. *Physical review letters*, 2010, 105(15): 154801.
- [51] Chao A, Granados E, Huang X, et al. High power radiation sources using the steady-state microbunching mechanism[C]// *Proc. 7th Int. Particle Accelerator Conf. (IPAC'16)*, Busan, Korea, May 2016. 1048-1053.
- [52] Ratner D, Chao A. Reversible seeding in storage rings[C]// *Proceedings of the 33th International Free Electron Laser Conference (FEL'11)*, Shanghai, China, 2011. 57-60.

- 
- [53] Deng X, Chao A, Feikes J, et al. Single-particle dynamics of microbunching[J]. *Physical Review Accelerators and Beams*, 2020, 23(4): 044002.
- [54] Simonin A, Agnello R, Bechu S, et al. Negative ion source development for a photoneutralization based neutral beam system for future fusion reactors[J]. *New Journal of Physics*, 2016, 18(12): 125005.
- [55] Escoffier S, Bertin P, Brossard M, et al. Accurate measurement of the electron beam polarization in jlab hall a using Compton polarimetry[J]. *Nuclear Instruments and Methods in Physics Research Section A: Accelerators, Spectrometers, Detectors and Associated Equipment*, 2005, 551(2-3): 563-574.
- [56] Baudrand S, Bouchel M, Brisson V, et al. A high precision Fabry-Perot cavity polarimeter at HERA[J]. *Journal of Instrumentation*, 2010, 5(06): P06005.
- [57] Rakhman A, Hafez M, Nanda S, et al. A high-finesse Fabry-Perot cavity with a frequency-doubled green laser for precision Compton polarimetry at Jefferson lab[J]. *Nuclear Instruments and Methods in Physics Research Section A: Accelerators, Spectrometers, Detectors and Associated Equipment*, 2016, 822: 82-96.
- [58] Carstens H, Lilienfein N, Holzberger S, et al. Megawatt-scale average-power ultrashort pulses in an enhancement cavity[J]. *Optics Letters*, 2014, 39(9): 2595-2598.
- [59] Potma E O, Evans C, Xie X S, et al. Picosecond-pulse amplification with an external passive optical cavity[J]. *Optics Letters*, 2003, 28(19): 1835-1837.
- [60] Sakaue K, Washio M, Endo A. Demonstration of an optical enhancement cavity with 10 micron wavelength[C]// *High-Power, High-Energy, and High-Intensity Laser Technology II: volume 9513*. International Society for Optics and Photonics, 2015: 951313.
- [61] Rakhman A, Notcutt M, Liu Y. Power enhancement of burst-mode ultraviolet pulses using a doubly resonant optical cavity[J]. *Optics Letters*, 2015, 40(23): 5562-5565.
- [62] Drever R, Hall J L, Kowalski F, et al. Laser phase and frequency stabilization using an optical resonator[J]. *Applied Physics B*, 1983, 31(2): 97-105.
- [63] Black E D. An introduction to Pound-Drever-Hall laser frequency stabilization[J]. *American Journal of Physics*, 2001, 69(1): 79-87.
- [64] Zhang J W, Han H N, Hou L, et al. Frequency doubled femtosecond ti: sapphire laser with an assisted enhancement cavity[J]. *Chinese Physics B*, 2015, 25(1): 014205.
- [65] Zhang J, Hua L Q, Yu S G, et al. Femtosecond enhancement cavity with kilowatt average power[J]. *Chinese Physics B*, 2019, 28(4): 044206.
- [66] Kogelnik H, Li T. Laser beams and resonators[J]. *Applied Optics*, 1966, 5(10): 1550-1567.
- [67] Siegman A E. *Lasers*[M]. University Science Books, 1986.
- [68] Romanini D, Ventrillard I, Méjean G, et al. Introduction to cavity enhanced absorption spectroscopy[M]// *Cavity-Enhanced Spectroscopy and Sensing*. Springer, 2014: 1-60.
- [69] Wang H, Amoudry L, Cassou K, et al. Linearly polarized laser beam with generalized boundary condition and non-paraxial corrections[J]. *Journal of the Optical Society of America A*, 2019, 36(12): 1949-1956.

## Bibliography

---

- [70] April A. Nonparaxial tm and te beams in free space[J]. *Optics Letters*, 2008, 33(14): 1563-1565.
- [71] Peatross J, Berrondo M, Smith D, et al. Vector fields in a tight laser focus: comparison of models[J]. *Optics Express*, 2017, 25(13): 13990-14007.
- [72] Lax M, Louisell W H, McKnight W B. From maxwell to paraxial wave optics[J/OL]. *Physical Review A*, 1975, 11: 1365-1370. DOI: 10.1103/PhysRevA.11.1365.
- [73] Martens A, Dupraz K, Cassou K, et al. Direct electron acceleration with tightly focused TM<sub>0,1</sub> beams: boundary conditions and non-paraxial corrections[J]. *Optics Letters*, 2014, 39(4): 981-984.
- [74] Dai L, Li J X, Zang W P, et al. Vacuum electron acceleration driven by a tightly focused radially polarized gaussian beam[J]. *Optics Express*, 2011, 19: 9303-9308.
- [75] Borghi R, Santarsiero M. Summing lax series for nonparaxial beam propogation[J]. *Optics Letters*, 2003, 28: 774-776.
- [76] Ignatovsky V S. Diffraction by a parabolic mirror having arbitrary opening[J]. *Transactions of the Optical Institute of Petrograd*, 1920, 1(5): 5.
- [77] Davis L W. Theory of electromagnetic beams[J]. *Physical Review A*, 1979, 19: 1177-1179.
- [78] Barton J P, Alexander D R. Fifth-order corrected electromagnetic field components for a fundamental gaussian beam[J]. *Journal of Applied Physics*, 1989, 66(7): 2800-2802.
- [79] Cullen A L, Yu P K. Complex source-point theory of the electromagnetic open resonator[J]. *Proceedings of the Royal Society of London. A. Mathematical and Physical Sciences*, 1979, 366(1725): 155-171.
- [80] González de Alaiza Martínez P, Duchateau G, Chimier B, et al. Maxwell-consistent, symmetry- and energy-preserving solutions for ultrashort-laser-pulse propagation beyond the paraxial approximation[J]. *Physical Review A*, 2018, 98: 043849.
- [81] Liu X, Cassou K, Dupraz K, et al. S-shaped non-paraxial corrections to general astigmatic beams[J]. *Journal of the Optical Society of America A*, 2017, 34(4): 576-582.
- [82] Favier P, Dupraz K, Cassou K, et al. Short pulse laser beam beyond paraxial approximation[J]. *Journal of the Optical Society of America A*, 2017, 34(8): 1351-1359.
- [83] Maucher F, Skupin S, Gardiner S A, et al. Creating complex optical longitudinal polarization structures[J]. *Physical Review Letters*, 2018, 120: 163903.
- [84] ANSYS® Workbench 2019R3[EB/OL].
- [85] Degallaix J. OSCAR a matlab based optical fft code[C]// *Journal of Physics: Conference Series*: volume 228. IOP Publishing, 2010: 012021.
- [86] Udem T, Holzwarth R, Hänsch T W. Optical frequency metrology[J]. *Nature*, 2002, 416(6877): 233-237.
- [87] Jones R J, Diels J C. Stabilization of femtosecond lasers for optical frequency metrology and direct optical to radio frequency synthesis[J]. *Physical Review Letters*, 2001, 86(15): 3288.
- [88] Amoudry L, Wang H, Cassou K, et al. Modal instability suppression in a high-average-power and high-finesse Fabry–Perot cavity[J]. *Applied Optics*, 2020, 59(1): 116-121.

## Bibliography

---

- [89] Dazzi A, Prater C B, Hu Q, et al. AFM-IR: combining atomic force microscopy and infrared spectroscopy for nanoscale chemical characterization[J]. *Applied Spectroscopy*, 2012, 66(12): 1365-1384.
- [90] Northup T E. Coherent control in cavity QED[D]. California Institute of Technology, 2008.
- [91] Winkler W, Danzmann K, Rüdiger A, et al. Heating by optical absorption and the performance of interferometric gravitational-wave detectors[J]. *Physical Review A*, 1991, 44(11): 7022.
- [92] Boccara A, Fournier D, Badoz J. Thermo-optical spectroscopy: Detection by the "mirage effect"[J]. *Applied Physics Letters*, 1980, 36(2): 130-132.
- [93] Klaassen T, de Jong J, van Exter M, et al. Transverse mode coupling in an optical resonator[J]. *Optics Letters*, 2005, 30(15): 1959-1961.
- [94] Gallais L, Commandré M. Laser-induced damage thresholds of bulk and coating optical materials at 1030 nm, 500 fs[J]. *Applied optics*, 2014, 53(4): A186-A196.
- [95] Gushwa K E, Torrie C I. Coming clean: understanding and mitigating optical contamination and laser induced damage in advanced LIGO[C]// *Laser-Induced Damage in Optical Materials: 2014: volume 9237*. International Society for Optics and Photonics, 2014: 923702.
- [96] Papernov S, Schmid A. Using gold nanoparticles as artificial defects in thin films: What have we learned about laser-induced damage driven by localized absorbers?[C]// *Laser-Induced Damage in Optical Materials: 2006: volume 6403*. International Society for Optics and Photonics, 2007: 64030D.
- [97] Amotchkina T, Trubetskov M, Pervak V. Experimental and numerical study of the nonlinear response of optical multilayers[J]. *Optics Express*, 2017, 25(11): 12675-12688.
- [98] Hello P, Vinet J Y. Analytical models of thermal aberrations in massive mirrors heated by high power laser beams[J]. *Journal de Physique*, 1990, 51(12): 1267-1282.
- [99] Hello P, Vinet J Y. Analytical models of transient thermoelastic deformations of mirrors heated by high power cw laser beams[J]. *Journal de Physique*, 1990, 51(20): 2243-2261.
- [100] Kim S H, Hwangbo C K. Temperature dependence of transmission center wavelength of narrow bandpass filters prepared by plasma ion-assisted deposition[J]. *Journal of the Korean Physical Society*, 2004, 45(1): 93-98.
- [101] Yeh P. Electromagnetic propagation in birefringent layered media[J]. *JOSA*, 1979, 69(5): 742-756.
- [102] Sassolas B. Etude et réalisation d'empilements multicouches sur des optiques asphériques de grandes dimensions pour des applications en lithographie Extrême UV[D]. Université Claude Bernard Lyon-1, 2008.
- [103] Bullington A L, Lantz B T, Fejer M M, et al. Modal frequency degeneracy in thermally loaded optical resonators[J]. *Applied Optics*, 2008, 47(15): 2840-2851.
- [104] Straniero N, Degallaix J, Flaminio R, et al. Realistic loss estimation due to the mirror surfaces in a 10 meters-long high finesse fabry-perot filter-cavity[J]. *Optics Express*, 2015, 23(16): 21455-21476.
- [105] Hello P. II: optical aspects of interferometric gravitational-wave detectors[M]// *Progress in optics: volume 38*. Elsevier, 1998: 85-164.

## Bibliography

---

- [106] Demésy G, Gallais L, Commandré M. Tridimensional multiphysics model for the study of photo-induced thermal effects in arbitrary nano-structures[J]. *Journal of the European Optical Society - Rapid publications*, 2011, 6(0).
- [107] Pupeza I, Eidam T, Rauschenberger J, et al. Power scaling of a high-repetition-rate enhancement cavity[J]. *Optics Letters*, 2010, 35(12): 2052-2054.
- [108] Potma E O, Evans C, Xie X S, et al. Picosecond-pulse amplification with an external passive optical cavity[J]. *Optics Letters*, 2003, 28(19): 1835-1837.
- [109] Jones R J, Ye J. High-repetition-rate coherent femtosecond pulse amplification with an external passive optical cavity[J]. *Optics Letters*, 2004, 29(23): 2812-2814.
- [110] Zomer F, Fedala Y, Pavloff N, et al. Polarization induced instabilities in external four-mirror Fabry-Perot cavities[J]. *Applied Optics*, 2009, 48(35): 6651-6661.
- [111] Locke C, Stuart D, Ivanov E, et al. A simple technique for accurate and complete characterisation of a fabry-perot cavity[J]. *Optics express*, 2009, 17(24): 21935-21943.

## Acknowledgements

Thank to my supervisor Pr. Wenhui Huang at Tsinghua University.

Thank to my supervisor Pr. Fabian Zomer at Paris-Saclay University.

Thank to Pr. Lixin Yan, Pr. Chuanxiang Tang, Pr. Huaibi Chen, Pr. Renkai Li, Pr. Yingchao Du, Pr. Jiaru Shi, Pr. Wei Lu, Pr. Jianfei Hua and Dr. Xing Liu at Tsinghua University.

Thank to Aurélien Martens, Kevin Dupraz, Kevin Cassou, Ronic Chiche, Victor Soskov, Pierre Favier and Loïc Amoudry at Paris-Saclay University.

The deepest thank goes to my parents. Love you two.

## Statement

本人郑重声明：所呈交的学位论文，是本人在导师指导下，独立进行研究工作所取得的成果。尽我所知，除文中已经注明引用的内容外，本学位论文的研究成果不包含任何他人享有著作权的内容。对本论文所涉及的研究工作做出贡献的其他个人和集体，均已在文中以明确方式标明。

签 名： 王焕 日 期： 2020年12月14日

## Resume and Academic Achievements

### 个人简历

1993年6月19日出生于山东省济南市。2011年9月考入四川大学物理学院核工程与核技术专业，2015年7月本科毕业并获得工学学士学位。2015年9月免试进入清华大学工程物理系攻读核科学与技术博士学位至今，指导教师为黄文会教授。2017年9月至2019年6月获清华大学博士生短期出国访学基金和法国政府Eiffel奖学金的资助，赴巴黎萨克雷大学进行联合培养博士生的学习，联合指导教师为Fabian Zomer教授。

### Resume

I was born in Jinan, Shandong Province on 19 June 1993. I entered College of Physics, Sichuan University in September, 2011, majored in Nuclear Engineering and Nuclear Technology, and graduated in July, 2015. I entered Department of Engineering Physics, Tsinghua University and started my Ph.D study in September, 2015 under the supervision of Professor Wenhui Huang. From September 2017 to June 2019 with the funding of Tsinghua Scholarship for Overseas Graduate Studies and Eiffel Scholarship, I studied as a joint Ph.D student at Paris-Saclay University under the supervision of Professor Fabian Zomer.

### 在学期间完成的相关学术成果

#### 学术论文:

- [1] Huan Wang, Loïc Amoudry, Kevin Cassou et al. "Linearly polarized laser beam with generalized boundary condition and non-paraxial corrections." *JOSA A* 36.12 (2019): 1949-1956. (SCI 收录, 检索号:WOS:000506236300011.)
- [2] Loïc Amoudry, Huan Wang, Kevin Cassou et al. "Modal instability suppression in a high-average-power and high-finesse Fabry-Perot cavity." *Applied Optics* 59.1 (2020): 116-121. (SCI 收录, 检索号:WOS:000506807000015.)
- [3] Huan Wang, Loïc Amoudry, Kevin Cassou et al. "Prior-damage dynamics in high-finesse optical enhancement cavity." *Applied Optics* 59.35 (2020): 10995-11002.

## 指导小组学术评语

光学增益腔由于可以提供高平均功率的激光脉冲，在包括高性能 X/γ 射线源研制、引力波探测、激光高次谐波产生等研究中有着重要的应用。随着应用的开展，对光学增益腔的功率水平、稳定性等参数提出了越来越高的要求，使高功率光学增益腔的研究成为了研究的热点和前沿。清华大学在持续开展汤姆逊散射源的研究工作，采用光学增益腔是提高射线通量的关键技术。王焕的论文工作就是在此背景下，开展了高平均功率光学增益腔的理论和实验研究。

围绕百千瓦平均功率、几十微米束腰、皮秒级束长的光学增益腔，王焕同学独立完成了光学增益腔的物理分析、搭建、调试和性能改进，取得了很好的创新性成果：采用推广型 Lax 级数展开的方法给出了强聚焦、线偏振激光场的非傍轴近似的表达式，为高效地模拟分析激光束与电子束的汤姆逊散射过程，提供了更精确的光腔内强聚焦激光场的描述；采用腔镜热弹性形变与腔内平均功率线性关联的模型，成功解释了高功率光腔内的模式不稳定性，模拟证明了 D 型镜法抑制模式不稳定性的有效性，实验上基于通过 D 型镜法实现了小时时间尺度的 200 千瓦功率水平的光腔稳定运行；针对光学增益腔高功率水平运行所出现的功率快速下降现象，建立了热斑引起腔镜表面形变造成散射损耗的模型，基于该模型的模拟结果与实验比较一致，该工作有助于理解功率快速下降现象背后的物理过程并起到腔镜损伤预警的作用。

王焕同学思想积极进步，政治立场坚定。该生数理基础知识扎实，专业知识全面，实验动手能力强，发表多篇科研论文，英语水平较高，能够熟练利用英语进行文献阅读、论文写作、专业交流，独立开展科研工作的能力强，学术作风严谨细致。

## 答辩委员会决议书

随着汤姆逊散射光源、自由电子激光、稳态微聚束光源等先进光源的发展，能够储存高平均功率激光的光学增益腔越来越受到重视。论文围绕应用于汤姆逊散射光源的光学增益腔展开理论与实验研究，具有重要的科学意义和工程应用价值。论文主要创新点如下：

1. 使用推广型的 Lax 级数展开的方法给出了强聚焦、线偏振激光场的非傍轴近似表达式，能够更精确地描述光腔内强聚焦激光场。

2. 对高功率光学增益腔内的模式不稳定性进行了建模分析，提出了利用 D 型镜抑制模式不稳定性的方法，并通过实验证明了其有效性。

3. 针对影响光腔稳定性的功率快速下降现象，建立了“热斑”模型，重现了实验现象，揭示了功率下降的物理机理，对光腔损伤能起到有效的预警作用。

论文工作反映了作者具有扎实的数理基础和专业知识，已具备独立从事科研工作的能力。论文写作规范，逻辑严谨，图表清晰。答辩中表述清楚，回答问题正确。

经答辩委员会表决，一致同意通过论文答辩，建议授予王焕工学博士学位，并推荐参加清华大学优秀博士论文评选。

**Résumé détaillé de la thèse.** Depuis la première opération du laser démontrée par Théodore Maiman en 1960, l'homme continue de s'efforcer d'augmenter la puissance du laser qui a été entravée par le seuil d'endommagement du matériau de gain laser. Une étape révolutionnaire de progrès a été franchie avec l'invention de la technique d'amplification d'impulsions pulsées (CPA) en 1985. De plus, pour les applications exigeant une puissance laser moyenne élevée et un taux de répétition élevé, la cavité résonante optique (OEC) basée sur des éléments optiques réfléchissants devient une des solutions les plus prometteuses. OEC est une cavité résonante Fabry-Pérot (FPC) sans milieu de gain à l'intérieur. Il ne souffre donc pas de la limite liée au seuil d'endommagement du milieu à gain. Outre la fonction d'amélioration de la puissance, le faisceau laser à l'intérieur de l'OEC peut atteindre un taux de répétition élevé, ce qui est particulièrement avantageux pour améliorer les signaux dans un processus physique qui a une faible efficacité de génération en un seul passage.

Les travaux de cette thèse se concentrent sur des études théoriques et expérimentales des OEC de puissance moyenne élevée visant une application dans les sources de rayons X Thomson. Dans le but d'augmenter le flux moyen des photons générés par diffusion Thomson, il est demandé que le faisceau laser à l'intérieur de l'OEC ait une petite taille avec un rayon de l'ordre de quelques dizaines de microns, une longueur d'impulsion de l'ordre de la picoseconde et une puissance moyenne intra-cavité stable de quelques centaines de kilowatts. Les principaux défis se situent dans les deux derniers points, à savoir la puissance et la stabilité moyennes intra-cavités élevées, qui demandent de comprendre le mécanisme des instabilités thermiques apparaissant avec l'accroissement de puissance et de trouver des méthodes pour les supprimer.

Dans le chapitre 1, une revue des méthodes expérimentales et des paramètres clés des sources lumineuses à diffusion Thomson basées sur l'OEC sont présentées. Une revue est également présentée sur le développement de l'OEC pour différentes applications, notamment la génération d'harmoniques d'ordre élevé (HHG) améliorée par cavité, les interféromètres de détection d'ondes gravitationnelles (GW), les sources de lumière de microbunching en régime permanent (SSMB), les expériences d'énergie de fusion et les polarimètres Compton, etc. Et des critiques sont présentées sur le développement de l'OEC sans applications ciblées, mais avec des fonctionnalités spécialisées, notamment une puissance moyenne intra-cavité élevée à une

échelle du mégawatts, fonctionnant pour des longueurs d'ondes laser incidente de 355 nm, 800 nm et 10  $\mu\text{m}$ , et avec verrouillage simultané de deux lasers incidents de longueurs d'onde différentes. En outre, une revue est présentée sur le développement de l'OEC en Chine avec des travaux expérimentaux représentatifs.

Dans le chapitre 2, les principes fondamentaux et les propriétés du FPC sont présentées pour établir le cadre théorique de cette thèse. Tout d'abord, les propriétés de la cavité elle-même sont présentées dans la section 2.1, y compris la condition de stabilité, les modes de cavité et le peigne de fréquence de cavité. Ensuite, les améliorations de la cavité avec injection en onde continue (CW) et injection en onde pulsée (PW) sont analysées séparément dans la section 2.2. Le couplage du faisceau laser d'injection dans la cavité est analysé à partir de l'adaptation de mode transverse avec le télescope et du verrouillage de phase longitudinal avec la technique PDH respectivement dans la section. 2.3.

Dans le chapitre 3, pour décrire précisément et efficacement le champ laser hautement focalisé à l'intérieur de l'OEC à utiliser dans les simulations de la diffusion Thomson, une expression de champ du champ laser polarisé linéairement hautement focalisé corrigé non paraxial est dérivée avec une méthode d'expansion de la série Lax généralisée. Une description précise et efficace du champ laser à l'intérieur de l'OEC est d'une importance cruciale pour faire une simulation de diffusion Thomson afin de prédire les propriétés des photons  $X/\gamma$ . Plusieurs approches ont été utilisées dans le passé pour modéliser le faisceau laser dans la région de focalisation, chacune correspondant à des hypothèses différentes. Des solutions particulières satisfaisant exactement les équations de Maxwell ont été obtenues pour des faisceaux laser à polarisation radiale qui fournissent des expressions auto-cohérentes qui correspondent cependant à des conditions aux limites définies qui peuvent ne pas être représentatives d'une expérience réelle. Des expressions intégrales des solutions des équations de Maxwell sont également disponibles mais souffrent d'approximations et sont également liées à des conditions aux limites spécifiques. Enfin, la technique historique consistant à étendre les solutions paraxiales des équations d'onde en série s'est récemment avérée offrir la capacité unique de rendre compte de conditions aux limites arbitraires. Cette capacité peut être considérée comme cruciale lorsque l'on considère la sensibilité du processus de diffusion aux conditions aux limites susceptibles de limiter le pouvoir prédictif des simulations détaillées et expansives.

Le formalisme de la m thode d'expansion g n ralis e des s ries de Lax est pr sent  dans la section 3.1. Avec la sym trie enracin e dans la d finition du potentiel Hertz, les potentiels vectoriels et scalaires couramment utilis s sont red finis avec des contreparties sym triques. Le probl me de la r solution de la distribution du champ est ensuite converti en probl me de la r solution de la distribution spatiale du potentiel vectoriel. Et avec la m thode perturbative, le probl me de la r solution de la distribution spatiale du potentiel vectoriel est converti en probl me de la r solution des  quations r cursives pour diff rents ordres de termes de correction. Pour prouver les performances de la m thode d'expansion g n ralis e des s ries de Lax, les coefficients de celle-ci sont ajust s   l'expression d'Ignatovsky qui est pr sent e dans la section 3.2. Le processus d'ajustement est pr sent  dans la section 3.3., Et les distributions de champ sont compar es entre celle de la m thode d'expansion g n ralis e des s ries de Lax et celle du formalisme d'Ignatovsky. Une bonne coh rence peut  tre obtenue avec seulement une correction non paraxiale du premier ordre par la m thode d'expansion g n ralis e de la s rie Lax par rapport   celle du formalisme Ignatovsky.

Au cours de l'exp rience consistant   essayer d'augmenter la puissance moyenne intra-cavit  de l'OEC, la puissance du laser incident est augment e progressivement. Dans le chapitre 4, il est pr sent  que des instabilit s modales ont commenc    appara tre lorsque la puissance moyenne intra-cavit  de l'OEC atteint plus de  $\sim 100$  kW. Sur la cam ra CCD plac e   la position de transmission dun miroir de cavit , les instabilit s induites par des d g n rescences modales sont observ es (mode TEM<sub>00</sub> d g n r  avec des modes d'ordre  lev ). Ces instabilit s modales qui affectent la stabilit  de la cavit  et emp chent l'augmentation de la puissance de la cavit  doivent  tre comprises et supprim es.

Avec le mod le de Winkler qui relie lin airement la d formation thermo lastique du miroir de cavit  en r gime permanent   la puissance moyenne intra-cavit , les instabilit s modales peuvent  tre bien mod lis es par la d g n rescence modale. Les ordres de modes d g n r s calcul s par la simulation repr sentent bien ceux observ s exp rimentalement et se r v lent tous assez  lev s. Pour  liminer les d g n rescences modales, des miroirs en forme de D sont introduits   l'int rieur de l'OEC pour introduire des pertes sur les modes d'ordres  lev s. Des simulations ont  t  effectu es pour estimer les performances attendues de ces miroirs sur l' limination des d g n rescences. Une paire de miroirs en forme de D a ensuite  t  impl ment e dans la cavit 

et une puissance moyenne intra-cavité stable à l'échelle d'une heure de 200 kW a été obtenue en 2018.

Après avoir résolu avec succès le problème des instabilités modales, en comparant les données de puissance moyenne intra-cavité à la puissance moyenne du laser incident pris entre 2017 et 2018, nous avons observé une baisse du gain dans la cavité. Le problème de la baisse de gain se comporte en deux volets, premièrement, avec la puissance maximale du laser incident moyen disponible de 40 W, la puissance moyenne intra-cavité est passée de 400 kW en 2017 à 200 kW en 2018; Deuxièmement, le gain a chuté par rapport à l'augmentation de la puissance moyenne intra-cavité pour les données prises en 2018. Ensuite, des efforts ont été consacrés à résoudre ce problème de baisse de gain.

Pour étudier la chute de gain de la cavité, le phénomène de chute de puissance rapide et non-linéaire de la cavité est observé en 2019. Ceci est présenté dans la section 5.1. Le temps caractéristique et l'amplitude de la chute de puissance moyenne intra-cavité observés dépendent de la puissance intra cavité. L'augmentation de la puissance du faisceau laser incident a conduit à un endommagement irréversible de la surface du miroir de couplage de cavité. Une analyse est effectuée pour comprendre le phénomène de chute de puissance rapide qui affecte la stabilité de la cavité et empêche la puissance intra-cavité d'atteindre l'objectif visé. L'origine de ce phénomène est étudiée par imagerie de surface de miroir post mortem et analyse des signaux transmis et réfléchis par l'OEC.

Après avoir exclu les effets dominants du couplage non linéaire et de l'absorption de puissance dans le revêtement multicouche, de la réponse temporelle de la photodiode et de la lecture électronique et du temps de remplissage de la cavité, on constate que la perte de diffusion induite par la déformation de la surface du miroir due à un probablement la physique dominante derrière ce phénomène. Un modèle de point chaud a été établi pour décrire le phénomène qui dépend de quatre ensembles de paramètres: le rayon du point chaud, le rapport puissance laser sur absorption de puissance thermique, la position du point chaud sur la surface du miroir de couplage et la position des miroirs en demie lune.

Des simulations ont été lancées pour modéliser le comportement du phénomène de chute de puissance rapide. Les simulations ont été divisées en deux étapes. Pour la première étape, nous trouvons les valeurs du rayon et du rapport d'absorption du point chaud qui décrivent le

régime permanent mesurer expérimentalement. Dans une deuxième étape, nous modélisons les données expérimentales transitoires avec les quatre autres paramètres du modèle. Pendant les simulations, le logiciel ANSYS a été utilisé pour calculer les déformations thermoélastiques de la surface du miroir en régime permanent et transitoire, et un code FFT basé sur MATLAB appelé OSCAR a été utilisé pour modéliser les signaux réfléchis et transmis par la cavité. Avec les simulations basées sur le modèle des points chauds, les comportements des données expérimentales en régime permanent et transitoire est bien décrit. Cette analyse pourrait aider à comprendre le processus physique derrière ce type de phénomène de chute de puissance apparaissant sur l'OEC appliqué dans une large gamme d'applications et à prévenir les dommages permanents au miroir.

Pour améliorer le flux moyen des rayons X, TTX prévoit de passer à une configuration combinant OEC et anneau de stockage d'électrons. Avant le développement de l'OEC pour la combinaison avec l'anneau de stockage d'électrons, des travaux de R&D doivent être effectués sur le prototype OEC de TTX qui s'appelle TBOX. Le prototype TBOX est indépendant de l'anneau de stockage d'électrons pour réaliser les objectifs de conception exigés pour l'OEC lui-même. Les objectifs comprennent une taille de faisceau laser avec une taille de rayon de quelques dizaines de micromètres à l'intérieur de l'OEC, une longueur temporelle d'impulsion laser intra-cavité de 10 ps avec un taux de répétition de quelques dizaines de MHz, et une puissance moyenne de la cavité de quelques centaines de kilowatts. Auparavant, une partie des travaux de conception du prototype OEC de TTX avait été effectuée, mais aucun travail expérimental n'a été engagé.

La conception complète de l'installation expérimentale de la TBOX et les expériences préliminaires qui y ont été effectuées sont présentées dans la section 6.1. Le but de l'expérience préliminaire est atteint avec succès. La finesse et le gain de la TBOX préliminaire sont mesurés. La conception de la configuration TBOX haute puissance pour réaliser une puissance moyenne de quelques centaines de kilowatts à l'intérieur est présentée dans la section 6.2. La conception de l'OEC final qui sera combiné avec l'anneau de stockage d'électrons est présentée dans la section 6.3.

Des remarques finales sont exposées au chapitre 7. Les travaux de R&D de l'OEC pour TTX seront poursuivis. Les travaux de R&D de l'OEC pour le SSMB à Tsinghua sont également en

cours et se poursuivront. D'autres travaux basés sur l'OEC sont envisagés. Pour satisfaire les demandes ultimes d'OEC d'une large gamme d'applications pour atteindre le niveau de puissance intra-cavité moyen en mégawatts, des problèmes doivent encore être résolus, notamment : découvrir la raison et lutter contre la baisse de gain avec l'augmentation de la puissance du laser d'injection; traiter les effets thermiques pour augmenter la stabilité de l'OEC.

**Titre:** Étude de cavités résonantes optiques pour les sources lumineuses à diffusion Thomson

**Mots clés:** Cavité résonante optique, diffusion Thomson, haute puissance, effet thermique modales et prouvé son efficacité par simulation. Une puissance moyenne intra-cavité stable à l'échelle horaire de 200 kW a été réalisée sur le prototype OEC de la source de lumière diffusée Thomson Thomson avec mise en uvre de miroirs en forme de D à l'intérieur.

**Résumé:** Les cavité résonante optique (OEC) de puissance moyenne élevée ont un large éventail d'applications, y compris la diffusion Thomson produisant des rayons X/ $\gamma$  quasi-monochromatiques à flux moyen élevé, notamment la génération d'harmoniques d'ordre élevé (HHG) améliorée par cavité, les interféromètres de détection d'ondes gravitationnelles (GW), les sources de lumière de microbunching en régime permanent (SSMB), les expériences d'énergie de fusion, etc.

Les travaux de cette thèse se concentrent sur des études théoriques et expérimentales des OEC de puissance moyenne élevée visant une application dans les sources de rayons X Thomson. Dans le but d'augmenter le flux moyen des photons générés par diffusion Thomson, il est demandé que le faisceau laser à l'intérieur de l'OEC ait une petite taille avec un rayon de lordre de quelques dizaines de microns, une longueur d'impulsion de l'ordre de la picoseconde et une puissance moyenne intra-cavité stable de quelques centaines de kilowatts.

Pour décrire précisément et efficacement le champ laser hautement focalisé à l'intérieur de l'OEC à utiliser dans les simulations de la diffusion Thomson, une expression de champ du champ laser polarisé linéairement hautement focalisé corrigé non paraxial est dérivée avec une méthode d'expansion de la série Lax généralisée.

Pour supprimer les instabilités modales commencent à apparaître apparemment sur OEC avec une puissance moyenne intra-cavité atteignant  $\sim 100$  kW qui affectent la stabilité de la cavité et pourraient conduire à une perte de verrouillage, les instabilités modales sont bien décrites avec les dégénérescences de mode induites par la surface du miroir déformation thermoélastique caractérisée par le modèle Winkler. Nous avons évoqué la méthode du miroir en forme de D pour supprimer les instabilités

L'analyse est effectuée pour comprendre le phénomène de chute de puissance rapide apparaissant sur l'OEC qui affecte la stabilité de la cavité et empêche la puissance intra-cavité d'atteindre l'objectif conçu. Des chutes de puissance intra-cavité sont apparues avec une ampleur et une échelle de temps en fonction du niveau de puissance. L'augmentation supplémentaire de la puissance incidente a conduit à des dommages irréversibles de la surface du miroir de couplage de cavité. L'origine de ce phénomène est étudiée par imagerie de surface miroir post mortem et analyse des signaux transmis et réfléchis par l'OEC. La perte de diffusion induite par la déformation de la surface du miroir due à un contaminant de point chaud s'avère très probablement la physique dominante derrière ce phénomène et le comportement de la cavité pourrait être bien reproduit par simulation. Cette analyse pourrait aider à comprendre le processus physique derrière ce type de phénomène de chute de puissance apparaissant sur l'OEC appliqué dans une large gamme d'applications et à prévenir les dommages permanents au miroir.

La conception complète du prototype OEC de la source de lumière à rayons X à diffusion Tsinghua Thomson (TTX) est présentée et une expérience préliminaire est réalisée dessus, réalisant l'objectif de verrouiller un laser à injection à ondes continues avec la cavité avec le gain de cavité mesuré à 133 L'invention concerne la conception de l'installation expérimentale à haute puissance pour le prototype TTX OEC et la conception du TTX OEC à coupler avec l'anneau de stockage d'électrons.

**Title:** Study of Optical Enhancement Cavity for Thomson Scattering Light Sources

**Keywords:** Optical enhancement cavity, Thomson scattering, high power, thermal effect

**Abstract:** High-average-power optical enhancement cavities (OEC), have a wide range of applications including Thomson scattering producing high average flux quasi-monochromatic X/ $\gamma$ -rays, cavity-enhanced high-order harmonic generation (HHG), gravitational wave interferometers, steady-state microbunching (SSMB) light sources and fusion energy experiments etc.

The works of this thesis focus on the theoretical and experimental studies of high-average-power OEC dedicated to Thomson scattering light sources. With the purpose of increasing the average flux of Thomson scattering generated photons, it is demanded for the laser beam inside OEC to have small waist with radius size of few tens of microns, pulse length at the order of picosecond and stable intra-cavity average power of few hundreds of kilowatts.

To precisely and effectively describe the highly focused laser field inside OEC to be used in simulations of Thomson scattering, a field expression of nonparaxial corrected highly focused linearly polarized laser field is derived with a generalized Lax series expansion method.

To suppress the modal instabilities start to appear apparently on OEC with an intra-cavity average power reaching  $\sim 100$  kW which affect cavity stability and could lead to lose of lock, the modal instabilities are well described with mode degeneracies induced by mirror surface thermoelastic deformation characterized by Winkler model. We brought up the D-shape mirror method for suppressing modal instabilities and proved its effectiveness with simulation.

An hour-time-scale stable intra-cavity average power of 200 kW was realized on the prototype OEC of Thomson scattering light source ThomX with implementation of D-shape mirrors inside.

Analysis is carried out for understanding the fast power drop phenomenon appearing on OEC which affects the cavity stability and hinders the intra-cavity power reaching the designed goal. Intra-cavity power drops appeared with magnitude and time scale depending on the power level. Increasing further the incident power led to irreversible damage of the cavity coupling mirror surface. The origin of this phenomenon is investigated with post mortem mirror surface imaging and analysis of the signals transmitted and reflected by the OEC. Scattering loss induced by mirror surface deformation due to a hot-spot contaminant is found to be most likely the dominant physics behind this phenomenon and the cavity behavior could be well reproduced by simulation. This analysis could help to understand the physical process behind this kind of power drop phenomenon appearing on OEC being applied in wide range of applications and to prevent permanent mirror damage.

Full design of the prototype OEC of Tsinghua Thomson scattering X-ray light source (TTX) is presented and preliminary experiment is carried out on it, realizing the goal of locking a continuous wave injection laser with the cavity with the cavity gain measured to be 133. Design of the high power experimental setup for TTX prototype OEC and the design for TTX OEC to be coupled with the electron storage ring are provided.